



**RESEARCH AND DEVELOPMENT TECHNICAL REPORT  
CECOM-TR-97-8635-F**

**LOW G-SENSITIVE QUARTZ RESONATORS, AND  
LOW-POWER CLOCK UTILIZING THE RESONATORS**

**James Stewart**

**VECTRON INTERNATIONAL  
166 GLOVER AVENUE  
NORWALK, CT 06856-5160**

**DECEMBER 1999**

Approved for public release;  
distribution is unlimited.

**20000214 079**

**CECOM  
U.S. ARMY COMMUNICATIONS-ELECTRONICS COMMAND  
RESEARCH, DEVELOPMENT AND ENGINEERING CENTER  
FORT MONMOUTH, NEW JERSEY 07703-5000**

**DTIC QUALITY INSPECTED 1**

## **NOTICES**

### **Disclaimers**

The findings in this report are not to be construed as an official Department of the Army position, unless so designated by other authorized documents.

The citation of trade names and names of manufacturers in this report is not to be construed as official Government endorsement or approval of commercial products or services referenced herein.

## REPORT DOCUMENTATION PAGE

Form Approved  
OMB No. 0704-0188

Public reporting burden for this collection of information is estimated to average 1 hour per response, including the time for reviewing instructions, searching existing data sources, gathering and maintaining the data needed, and completing and reviewing the collection of information. Send comments regarding this burden estimate or any other aspect of this collection of information, including suggestions for reducing this burden, to Washington Headquarters Services, Directorate for Information Operations and Reports, 1215 Jefferson Davis Highway, Suite 1204, Arlington, VA 22202-4302, and to the Office of Management and Budget, Paperwork Reduction Project (0704-0188), Washington, DC 20503.

1. AGENCY USE ONLY (Leave blank)	2. REPORT DATE December 1999	3. REPORT TYPE AND DATES COVERED Final Report: Oct 97 to Sep 99	
4. TITLE AND SUBTITLE LOW G-SENSITIVE QUARTZ RESONATORS, AND LOW-POWER CLOCK UTILIZING THE RESONATORS		5. FUNDING NUMBERS C: N66001-97-C-8635	
6. AUTHOR(S) James Stewart			
7. PERFORMING ORGANIZATION NAME(S) AND ADDRESS(ES) Vectron International 166 Glover Avenue Norwalk, CT 06856-5160		8. PERFORMING ORGANIZATION REPORT NUMBER	
9. SPONSORING / MONITORING AGENCY NAME(S) AND ADDRESS(ES) US Army Communications-Electronics Command (CECOM) Research, Development and Engineering Center (RDEC) ATTN: AMSEL-RD-C2-CS Fort Monmouth, NJ 07703-5000		10. SPONSORING / MONITORING AGENCY REPORT NUMBER CECOM-TR-97-8635-F	
11. SUPPLEMENTARY NOTES			
12a. DISTRIBUTION / AVAILABILITY STATEMENT  Approved for public release; distribution is unlimited.		12b. DISTRIBUTION CODE	
13. ABSTRACT (Maximum 200 words)  This report presents the results of ongoing theoretical and experimental work toward reducing the sensitivity of crystal resonators to vibration and other accelerations. Strip resonators were the chosen embodiment, and extensive finite element analysis was performed on various electrode configurations and cantilever extensions of the crystal blank beyond the supports. Measurements on resonators fabricated following theoretical designs have shown that acceleration sensitivity has been reduced by an order of magnitude, to one-tenth part per billion per g. There are indications that the techniques reported here can yield another order-of-magnitude improvement. Theory, finite-element analysis, design approach, construction details, and test results are presented.			
14. SUBJECT TERMS Crystal oscillators; phase noise; vibration sensitivity; oven-controlled oscillators; miniature oscillators; low-power oscillators; quartz resonators		15. NUMBER OF PAGES 119	
		16. PRICE CODE	
17. SECURITY CLASSIFICATION OF REPORT Unclassified	18. SECURITY CLASSIFICATION OF THIS PAGE Unclassified	19. SECURITY CLASSIFICATION OF ABSTRACT Unclassified	20. LIMITATION OF ABSTRACT UL

## TABLE OF CONTENTS

<u>PART 1: Report on the Design Optimization of Singly and Doubly Rotated Crystal Resonators That Minimize the Sensitivity of the Acceleration Sensitivity to Manufacturing Imperfections</u>	1
Introduction	1
Sensitivity of $\Gamma$ to Misalignment of the Electrode Plating	2
Minimization of the Sensitivity of $\Gamma$ to Manufacturing Imperfections as a Nonlinear Optimization Problem	3
Discussion of Results	3
Part One Conclusions	5
References	5
Part One Figures (1-23)	7-38
 <u>PART 2: Report on the Theoretical and Experimental Results for Optimization of the Acceleration Sensitivity of Rectangular Crystal Resonators</u>	 39
Introduction	39
Measurement Techniques	39
Discussion of Results	40
Part Two Conclusions	43
References	43
Appendix A: Tabulated Results	44
Part Two Figures (1-21)	47-61
 <u>PART 3: Report on the Development of the Miniature Low Power SDIL &amp; DDIL OCXOs for Low G-Sensitivity Applications (Slides)</u>	 63
SDIL & DDIL OCXO Development	64
SDIL & DDIL Test Data (Description)	75
• Current Aging Over Time	76
• Temp Stability Data/Evaluation	77
• Current Consumption Data/Evaluation	86
• OCXO Warmup Data/Evaluation	91
• Vibration Sensitivity Data/Evaluation	97
• Phase Noise Data/Evaluation	105
• Allan Deviation Data	110
• Summary	113

## FIGURES

### Part 1:

1. Functional layout of nonlinear optimization software package.	7
2. Geometry and dimensions for mode-offset study.	7
3. Orientation of crystal blank rotation for mode-offset study.	7
4. Sensitivity study for SC cut.	8-10
5. $C_{max}$ for rectangular SC cut at larger aspect ratios.	11
6. Refinement of Fig. (4.K) for $\gamma=136^\circ - 156^\circ$ .	11
7. $C_{max}$ vs. $\gamma$ for SC cut at various LW values for rigid mount along all four edges.	12
8. $C_{max}$ vs. $\gamma$ for SC cut at various LW values for rigid mount along two edges (X-X).	12
9. Sensitivity study for FC cut	13-15
10. Sensitivity study for AT cut.	16-18
11. $C_{max}$ vs. $\gamma$ for AT cut at various LW values for rigid mount along all four edges.	19
12. $C_{max}$ vs. $\gamma$ for AT cut at various LW values for rigid mount along two edges (X-X).	19
13. Sensitivity study for BT cut.	20-22
14. Mode mispositioning analysis for slotted-ribbon mounted rectangular SC-cut plate.	23-25
15. Effect of overhang distance on the mispositioning coefficient for slotted-ribbon mount.	26
16. Mode mispositioning analysis for two-point mounted elliptical SC cut plate.	27
17. Mode positioning analysis for four-point mounted elliptical SC cut plate.	28
18. Mode mispositioning analysis for continuously mounted elliptical SC cut plate.	29
19. Effect of geometric scale on the mispositioning coefficient for a rectangular SC cut plate.	30
20. Geometry for four-point mounted plate with cubic shaped boundary used for shape optimization studies.	31
21. $C_{max}$ vs. blank orientation for convex and concave blank geometries.	32-36
22. Minimum $C_{max}$ vs. shape factor for convex and concave blank geometries.	37
23. Summary of results from nonlinear optimization study.	38

### Part 2:

1. Schematic diagram for measurement system.	47
2. Rectangular AT/SC cut crystal with double-ended mount in S-Type ceramic package.	47
3. $\Gamma$ Vs. Frequency for rectangular AT cut plate.	48
4. Distribution of results $-Z'$ elongated, double-ended mount.	48
5. Distribution of results $-X'$ elongated, double-ended mount.	49
6. Distribution of results $-Z'$ elongated, single-ended mount.	49
7. Distribution of results $-X'$ elongated, single-ended mount.	50
8. Distribution of results for small K-type crystals, AT cut.	50
9. Geometry used for FEA study on rectangular AT cut with overhang mount.	51
10. Typical FEA model used for study on rectangular AT cut with overhang mount.	51
11a. Variation of $\Gamma$ with overhang lengths for various types of support-beam spacing.	52

11b. Variation of $C_{\max}$ with overhang length for various values of support-beam spacing.	52
12a. Variation of $\Gamma$ components with support beam spacing, 0.210 in. length crystal.	53
12b. Variation of $C_{\max}$ with support-beam spacing, 0.210 in. length crystal.	53
13a. Photochemical-etched lead frame.	54
13b. Lead-frame mounted rectangular AT cut crystal.	54
14a. Results for various lead-frame mounted devices.	55
14b. Variation of $\Gamma$ magnitude with support-beam spacing, lead frame mount.	55
15. Variation of $\Gamma$ components with support-beam spacing, lead-frame mount.	56
16. Comparison of $\Gamma$ magnitude for fundamental and 3 <sup>rd</sup> O.T., lead frame mount.	56
17a. Distribution of $\Gamma$ in each of the three axes, lead frame design, 20 MHz. fundamental, 0.140" beam spacing.	57
17b. Distribution of $ \Gamma $ , lead-frame design, 20 MHz. fundamental, 0.140" spacing.	57
17c. Distribution of $\Gamma$ in each of the three axes, lead frame design, 60 MHz., 3 <sup>rd</sup> O.T., 0.140" beam spacing.	58
17d. Distribution of $ \Gamma $ , lead-frame design, 60 MHz., 3 <sup>rd</sup> O.T., 0.140" beam spacing.	58
18. Variation of $\Gamma$ components with blank orientation, SC cut, double-end mount.	59
19. Slotted clip for mounting rectangular crystals.	60
20. Rectangular AT cut Z'-elongated crystal mounted with slotted clips.	61
21. Variation of $\Gamma$ with support spacing for slotted-clip mounted crystals.	61

## FOREWORD

This report is presented in three parts; the first part was published as an interim report for the contract in August 98, and it consists of a number of theoretical studies on minimization of the g-sensitivity of strip resonators with various geometries and mounting structures. The second part describes an extension of the theoretical work, concentrating on some of the blank geometries which showed the highest probability of success, together with practical results on devices. The third part describes the low-g sensitivity SDIL and DDIL OCXOs development and the corresponding test data.

## **Part 1: Report on The Design Optimization of Singly and Doubly Rotated Crystal Resonators Which Minimize The Sensitivity of The Acceleration Sensitivity to Manufacturing Imperfections.**

### **Introduction**

Manufacturing precision crystal resonators with low acceleration sensitivity continues to be a major challenge in the production of ultra stable frequency sources for many applications, such as GPS. This problem has received quite a bit of academic attention in recent years, and there exist established theoretical results which point to good crystal design principles for low g-sensitivity. In production however, there generally seems to be a lower bound of a few parts in  $10^{-10}/g$  on what is reproducible with any reasonable yield, while a small number of crystals are produced with very low g-sensitivities ( $< 1 \times 10^{-10}/g$ ), suggesting that very good resonators are at least possible to manufacture. The fundamental problem faced in producing real resonators is that the acceleration sensitivity can be very sensitive to manufacturing tolerances for a particular design. The present study seeks to quantify this phenomenon by using a finite element model to obtain an accurate description of the stresses and deformations in a crystal plate that has been mounted in various configurations and then combine this solution with an analytical solution of the vibration mode shape for a harmonic of thickness shear in the general perturbation procedure developed by H.F. Tiersten [1,2] to obtain the frequency shift. To this end, a very powerful software tool has been created which utilizes previously developed finite element software integrated together with a custom developed numerical perturbation integral solver to compute the frequency shift under any applied static bias. This finite element procedure has been integrated into a general nonlinear optimization program to automate the search for good designs.

To compute the frequency shift, a general purpose integration method has been developed which calculates the first perturbation of the Eigen-value from a finite element solution of the static biasing state and an analytical solution of the mode shape for a trapped energy resonator operating in an arbitrary overtone of thickness shear. The numerical technique that has been employed generalizes previously developed methods by L.D. Clayton and E.P. Eernisse [5] with many enhancements to improve accuracy. Similar techniques have been applied to problems in SAW acceleration sensitivity by Sinha and Locke [7], as well as by the first author [8]. Similar finite element methods have been developed for BAW devices by the authors [6] for the analysis of mounting stresses in crystal resonators. The mode shape that has been developed is completely general accommodating either singly or doubly rotated cuts of quartz through the well know planar transformation of the mode shape axes. The integration procedure readily accommodates this planar transformation, as well as the existence of non-rectangular geometries caused by circular or elliptical electrodes and/or contouring by using a very general quadrature procedure. Using the developed software tools, detailed sensitivity studies are performed on rectangular, circular, elliptical, and more general shaped resonator geometries with various mounting schemes for the purpose of ranking the designs with respect to their sensitivity to manufacturing imperfections.



## Sensitivity of $\Gamma$ To Misalignment of the Electrode Plating

The sensitivity of the acceleration sensitivity to misalignment of the electrode is obtained by following Tiersten's analysis [3,4]. Shown in figure (2) is the geometry of a rectangular crystal resonator with a single pair of identical electrodes, which in the unperturbed case, are located in the center of the plate. When the resonator is manufactured it is assumed to have a small error in the electrode placement, as shown. The resulting electrode will be displaced from the center by a small distance  $R$ , at an angle  $\alpha$ . In general, the acceleration sensitivity vector for the resonator is denoted by

$$\Gamma^{(j)}, j = 1, \dots, 3 \quad (1)$$

The sensitivity of  $\Gamma$  to electrode misalignment is obtained by expanding this quantity to first order in the mode offset distances

$$\Gamma^{(j)} \approx \Gamma_0^{(j)} + \frac{\partial \Gamma^{(j)}}{\partial d_A} d_A, A = 1, 3 \quad (2)$$

where  $d_1 = R \cos \alpha$  and  $d_3 = R \sin \alpha$  are the mode offset distances in the  $x_1$  and  $x_3$  directions, respectively. For a perfectly symmetric mounting structure,

$$\Gamma_0^{(j)} = 0 \quad (3)$$

which gives

$$\Gamma^{(j)} = C_A^{(j)} d_A \quad (4)$$

where  $C_A^{(j)}$  are the so-called mispositioning coefficients. The maximum sensitivity to mode mispositioning is defined as

$$C_{\max} = \frac{\Gamma_{\max}}{R} \quad (5)$$

where

$$\Gamma_{\max} = \max\{|\Gamma|, \alpha = 0^\circ \dots 360^\circ\} \quad (6)$$

with

$$|\Gamma| = \sqrt{\Gamma^{(1)2} + \Gamma^{(2)2} + \Gamma^{(3)2}} \quad (7)$$

representing the magnitude of the acceleration sensitivity vector.  $C_{\max}$  represents the maximum sensitivity of the acceleration sensitivity to misalignment of the electrode structure with respect to the support system.

## Minimization of the Sensitivity of $\Gamma$ to Manufacturing Imperfections as a Nonlinear Optimization Problem

For a given support structure, the mode mispositioning coefficient is a function of geometric and material parameters defining the structural system of resonator and mount. In general,

$$C_{\max} = C_{\max}(a_1, a_2, \dots, a_n) \quad (8)$$

where  $a_i$  represent  $N$  generalized variable parameters defining the geometry, crystal cut, blank orientation, etc. Define the general nonlinear optimization problem:

$$\text{Minimize } C_{\max}(a_1, \dots, a_N)$$

$$\text{Subject to: } a_i^L \leq a_i \leq a_i^U, i = 1, \dots, N \quad (9)$$

where  $a_i^L$  and  $a_i^U$  represent lower and upper bounds placed on each parameter.

Figure (1) shows a functional layout of the non-linear optimization program developed to solve equation (9). The present analysis makes use of the IMSL routine BCONF, which minimizes a function of  $N$  variables subject to bounds on the variables using a quasi-Newton method and a finite difference gradient.

## Discussion of Results

Using the developed software, numerical studies have been carried out on resonators of different geometries and crystal cuts for the purpose of comparing the various designs. In all cases the plate thickness has been held constant and a fundamental thickness harmonic has been considered. Also, the basic ranges of major dimensions have been held constant for different blank geometries and mounting schemes. This allows the different designs to be compared most accurately. The basic dimensions used are summarized in figure (2) and figure (3) shows the sense of rotation for the blank rotation used in all the studies. Figures (4.a) - (4.j) show the results of a basic study of the effect of a 0.1 mm mode offset on the total  $\Gamma$  of a rectangular SC Cut resonator rigidly mounted along all four edges. These plots show the magnitude of  $\Gamma$  in units of  $10^{-10}/g$  vs. the angle of mode offset,  $\alpha$ , for various length to width ratios. This study was done for  $L/W$  ratios of 0.5, 0.6, 0.7, 0.8, 0.9, 1.0, 1.11, 1.25, 1.43, 1.67, and 2.0. Only the curves representing  $L/W = 0.5, 1.0$ , and 2.0 are labeled so as to not clutter the graphs. Each of the graphs in figure (4) represent different blank rotations with respect to the crystallographic axes, taken in twenty degree increments. From these curves it is observed that the sensitivity of the resonator to mode offset varies widely with respect to blank orientation and planar aspect ratio with roughly an order of magnitude difference between the best and worst values. Figure (4.k) summarizes the results by plotting  $C_{\max}$  as a function of planar aspect ratio for different blank orientations. The horizontal scale in this graph is in dimensionless aspect ratio with the vertical scale representing units of  $10^{-6}$  per meter per 1 g acceleration. By tracing the minimum  $C_{\max}$  over all aspect ratios, it can be seen that for this particular mounting condition, the 1:1 aspect ratio is the worst case with the best cases realized by elongated plates (1:2 or 2:1 planar aspect ratios). Figure (6) shows a refined study done in the vicinity of  $\gamma=136^\circ$  to  $156^\circ$  which shows an approximate minimum at  $\gamma=128^\circ$ . This result was verified later with the optimizer. Figure (5) shows similar results for larger aspect ratios. It is observed here that the

sensitivity tends to level off at higher aspect ratios, suggesting that for greatly elongated plates, the  $C_{\max}$  is not sensitive to errors in actual blank dimensions. Figure (7) shows the dependency of  $C_{\max}$  on  $\gamma$  for the range of aspect ratios from 1:2 to 2:1 for an SC Cut rectangular plate rigidly mounted along all four edges. Here it is seen again that the optimum blank orientation occurs at  $38^\circ \pm 90^\circ$ . Figure (8) shows the results of the same study carried out on a plate with rigid mounts along only two edges ( $x_1 = \pm L$ ). Here it is seen that the best result is obtained for an aspect ratio of 1:2 at roughly the same angle. This represents the case of a rigid mount along the long dimension of the plate. The case of a rigid mount along the short dimension is represented by aspect ratios greater than 1.0. For this case the optimum occurs at a slightly higher value of  $\gamma$  with about twice the sensitivity of that obtained for the four edge mount. Figure (9) shows the results of a similar study carried out for an FC Cut plate. By inspection it is seen that the FC Cut behaves essentially the same as the SC with only slight differences. Figures (10) - (12) represent a study carried out for an AT Cut plate and figure (13) shows results for the BT Cut. It is observed that the theoretical behavior of the singly rotated cuts is very different from that of the SC or FC. The optimum values obtained for AT and BT cuts are found at  $\gamma = 0^\circ$  with roughly twice the sensitivity of the four edge mounted SC Cut. Shown in figure (14) is the geometry of a rectangular SC Cut resonator mounted along two edges with thin slotted ribbons with overhang of the crystal beyond the support by a distance of  $L_0$ . Figures (14.a) - (14.e) show the results of a study carried out on this plate for various values of  $L_0$ . Considering the case of mounting along the short edge ( $L/W > 1$ ), it is observed here that the minimum  $C_{\max}$  is found at roughly  $\gamma = 120^\circ$  for all cases with the actual minimum value changing with overhang distance. Using the optimization program, optimal values have been found for this case of  $L = 5.0$  mm,  $W = 2.9$  mm ( $L/W = 1.72$ ),  $\gamma = 129^\circ$ , and  $L_0 = 3.5$  mm ( $L_0/L_{\text{total}} = 0.206$ ). Figures (15.a) and (15.b) show the centerline deflection of the blank along the two planar axes under the action of normal acceleration for different  $L_0$  values. Interesting to note here is that the optimum value does not correspond to the minimum deflection case. Figure (15.c) shows the effect of overhang distance on  $C_{\max}$ . The dotted line in this figure represents the same plate rigidly mounted along the two edges with the same inner dimensions. Figures (16) - (18) show results obtained for an elliptical SC Cut plate using, respectively, two point, four point, and fully supported mounting schemes. Interesting to note is that in the fully supported case, there is very little difference between the elliptical plate and the rectangular plate as shown in figure (7). Also worth noting is that in the case of the four point mount as shown in figure (17), the optimal values are obtained at  $\gamma = 0^\circ, \pm 90^\circ$ . Figure (19) shows the results of a study done on the effect of geometric scale on  $C_{\max}$  for an SC Cut rectangular plate rigidly supported along all four edges. In this figure, the magnification of the  $C_{\max}$  value is plotted as a function of geometric scale factor,  $K$ , for various cases. From these results, it is observed that  $C_{\max}$  is relatively invariant to scale when the thickness of the plate is scaled with the lateral dimensions, but is very sensitive to lateral scaling at constant thickness. In general,  $C_{\max}$  will scale with lateral dimensions at constant thickness (constant frequency) as the square of  $K$  when the electrode size is held constant. Figure (20) shows the configuration for a general shape blank in which a parametric cubic spline is used to define the outer edge of the plate. Shown in figures (20.a) and (20.b) are the possible shapes realizable by the curves when the shape factors  $k_1$  and  $k_3$  are varied through values of 1.0 to 3.0 for convex and concave profiles. Figures (21.a) - (21.j) show the results of a study done for convex and concave geometries using various  $k_1$  and  $k_3$  values for a four point mounted SC Cut resonator. It is observed here that while the general shape of the plotted curves changes with the geometry, the minimum  $C_{\max}$  obtainable does not vary appreciably. This fact is highlighted in the plots of figure (23) which show the effect of varying the shape factors  $k_1$  and  $k_3$  on the optimum  $C_{\max}$ . The total variation in  $C_{\max}$  shown in these plots is roughly  $0.1 \times 10^{-6}$  /m/g, which is quite small when compared to the effect of aspect ratio and blank orientation.

## Part One Conclusions

Shown in figure (23) is a table of results obtained from the optimization program for the various geometries and crystal cuts considered. The very best results are obtained from the fully supported plate with crystal cut in the vicinity of the SC, with  $C_{\max} \approx 0.25 \cdot 10^{-6}$ . This value is achieved at a specific aspect ratio and blank orientation, and is generally not changed dramatically by using different shapes other than a rectangle. The  $\phi$  angle has a small effect on the minimum  $C_{\max}$ , although this is not a dominating factor. In the case of the rectangular plate rigidly mounted along two edges only, it is observed that the minimum value of  $C_{\max} = 0.56 \cdot 10^{-6}$  for the SC Cut is roughly twice that obtained for the full four edge mount. For the AT Cut, an optimum value of  $C_{\max} = 0.50 \cdot 10^{-6}$  is obtained for the four edge mount and a corresponding value of  $C_{\max} = 0.80 \cdot 10^{-6}$  is obtained for the two edge mount. It appears that the compensating effects of optimal blank aspect ratio and orientation are fully developed with a continuous mount around the perimeter. For a two edge mount, the effect of overhangs has been found to be a factor at a given blank orientation as illustrated by figure (15.c). In the example considered here, the overhang tends to improve the sensitivity of the structure to manufacturing imperfections over the corresponding rigid mounted plate. The effects of scaling the geometry as illustrated by figure (19) are also significant. These results suggest that an advantage can be gained by shrinking the planar geometry of a crystal at a given frequency. For a four point mounted crystal, there is a small effect of overall shape on the minimum  $C_{\max}$  obtainable. The results of the shape optimization suggest that there is a small advantage to be gained by effectively trimming off the portions of an elliptical blank between the supports, resulting in somewhat of a diamond shape. In general, the most important parameters for reducing  $C_{\max}$  are the planar aspect ratio and the blank orientation, and not the actual shape of the resonator.

## References

- J.C. Baumhauer and H.F. Tiersten, "Nonlinear Electroelastic Equations for Small Fields Superposed on a Bias", J. Acoust. Soc. Am., Vol. 54, No. 4, 1973, pp. 1017-1034.
- H.F. Tiersten, "Perturbation Theory For Linear Electroelastic Equations for Small Fields Superposed On a Bias", J. Acoust. Soc. Am., Vol. 64, No. 3, Sept., 1978 pp. 832-837.
- Y.S. Zhou and H.F. Tiersten, "On the Normal Acceleration Sensitivity of Contoured Quartz Resonators With the Mode Shape Displaced With Respect to Rectangular Supports", J. Appl. Phys., 69(5) March 1991, pp. 2862-2870.
- H.F. Tiersten and Y.S. Zhou, "On the In-Plane Acceleration Sensitivity of Contoured Quartz Resonators Supported Along Rectangular Edges", J. Appl. Phys., 70(9) Nov. 1991, pp. 4708-4714.
- L.P. Clayton and E.P. Eemisse, "Frequency Shift Calculations for Quartz Resonators", Proceedings of the 1991 IEEE International Frequency Control Symposium, pp. 309-320.
- J.T. Stewart and D.S. Stevens, "Analysis of the Effects of Mounting Stresses on the Resonant Frequency of Crystal Resonators", Proc. 1997 IEEE International Frequency Control Symposium, pp. 621-629.
- B.K. Sinha and S. Locke, "Acceleration and Vibration Sensitivity of SAW Devices", IEEE Trans. Ultrason. Ferroelec. Freq. Contr., Vol. UFFC-34, no. 1, pp. 29-38, Jan. 1987.

J.T. Stewart, R.C. McGowan, J.A. Kosinski, and A. Ballato, "Semi-Analytical Finite Element Analysis of Acceleration-Induced Frequency Change In SAW Resonators", Proc. 1995 IEEE International Frequency Control Symposium, pp. 499-506

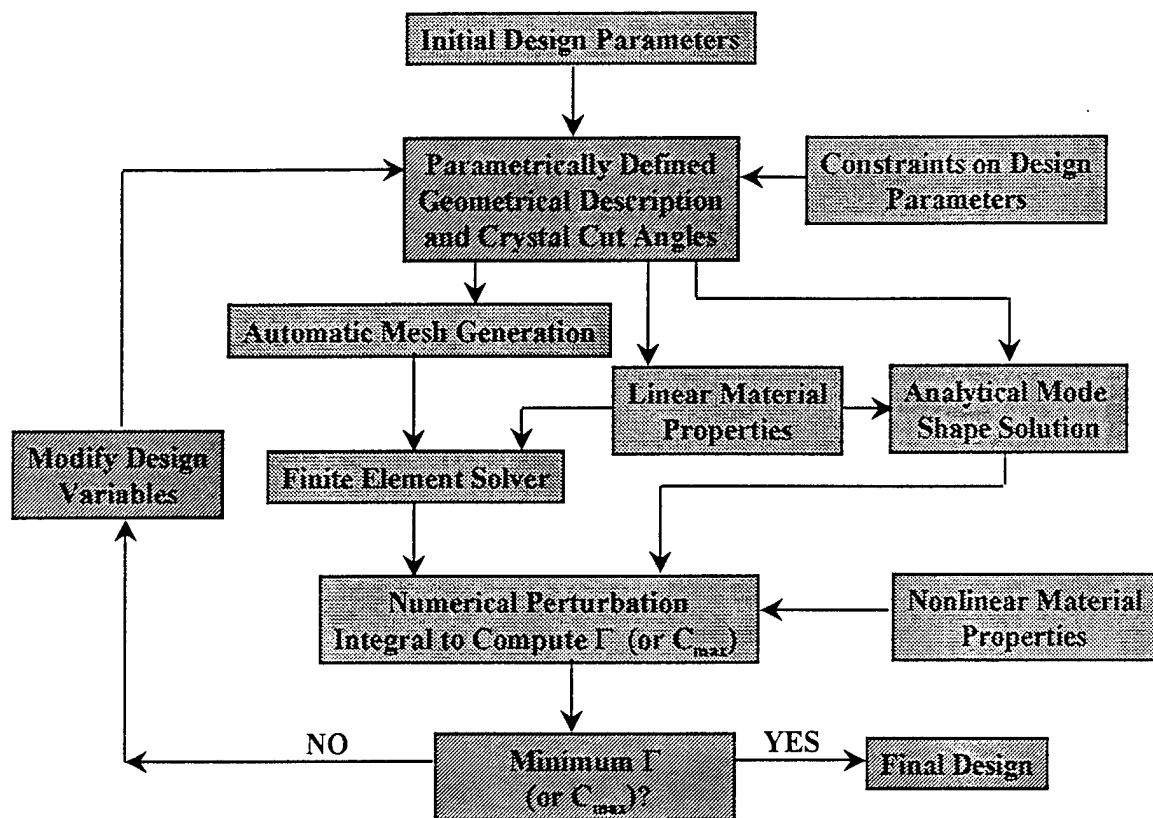
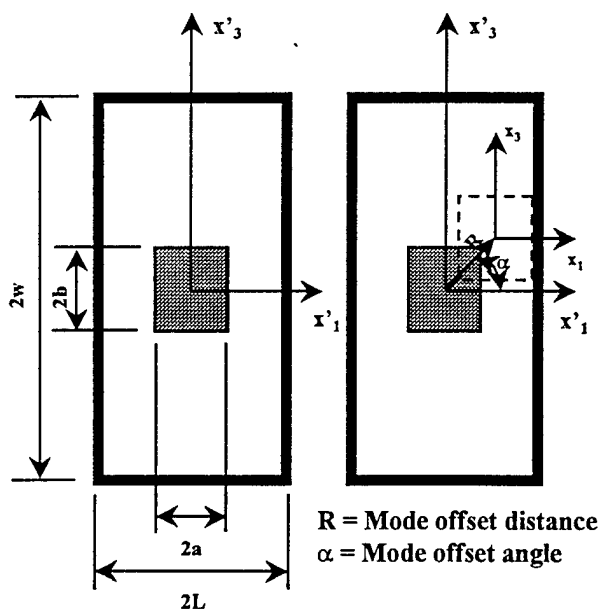
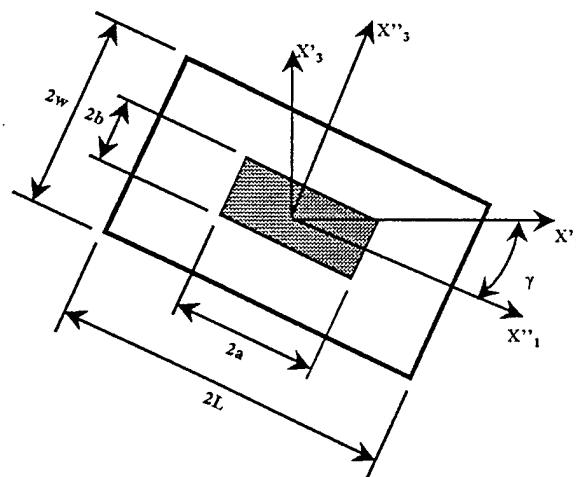


Figure 1.) Functional layout of non-linear optimization software package.



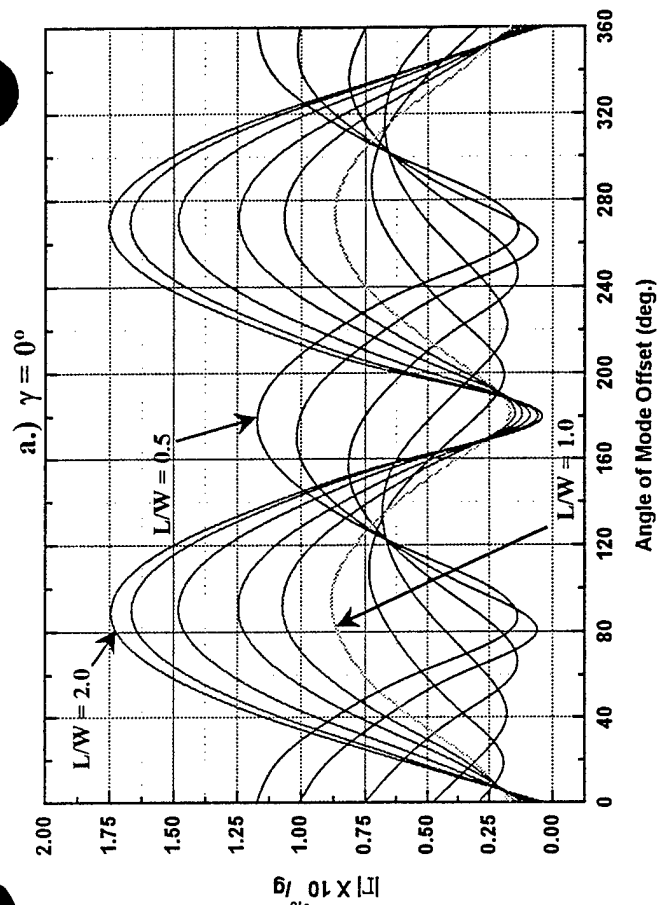
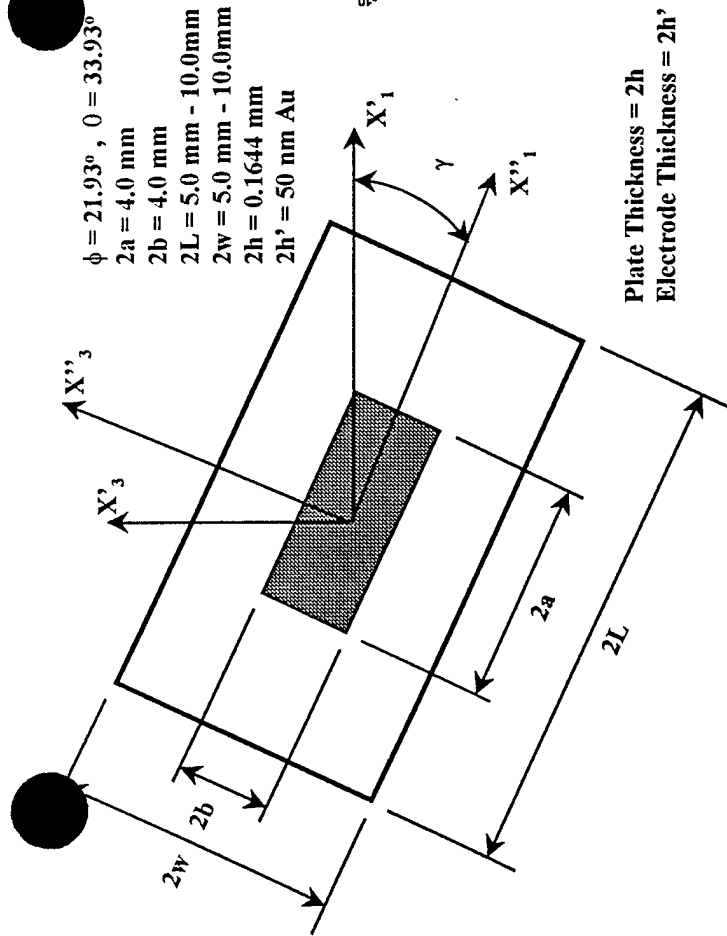
$2a = 4.0 \text{ mm}$   
 $2b = 4.0 \text{ mm}$   
 $2L = 5.0 \text{ mm} - 10.0 \text{ mm}$   
 $2w = 5.0 \text{ mm} - 10.0 \text{ mm}$   
 $2h = 0.1644 \text{ mm}$   
 $2h' = 50 \text{ nm Au}$

Figure 2.) Geometry and dimensions for mode offset study.

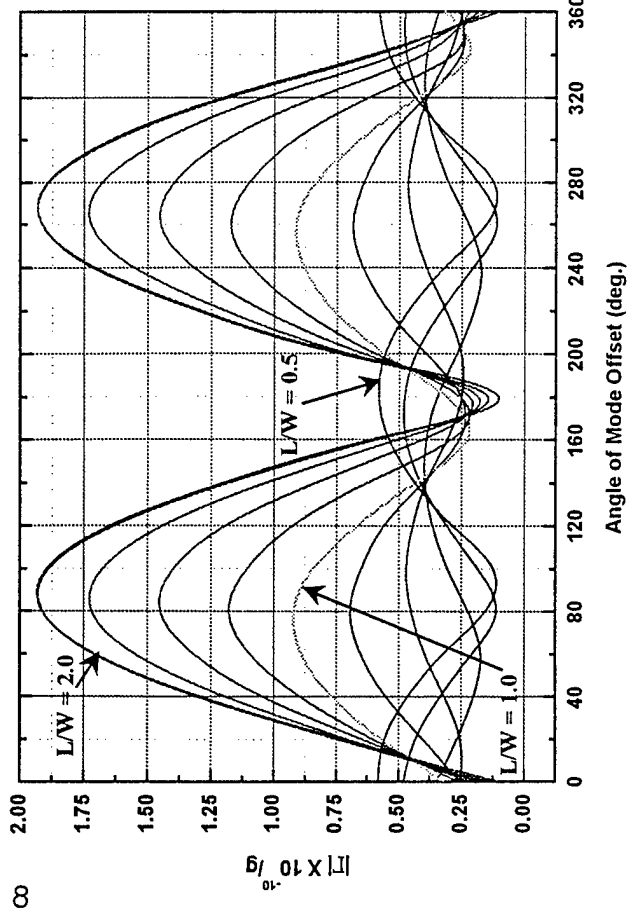


$\gamma$  = Blank rotation angle  
 $2h$  = Blank thickness  
 $2h'$  = Electrode thickness

Figure 3.) Orientation of crystal blank rotation for mode offset study.



b.)  $\gamma = 20^\circ$



c.)  $\gamma = 40^\circ$

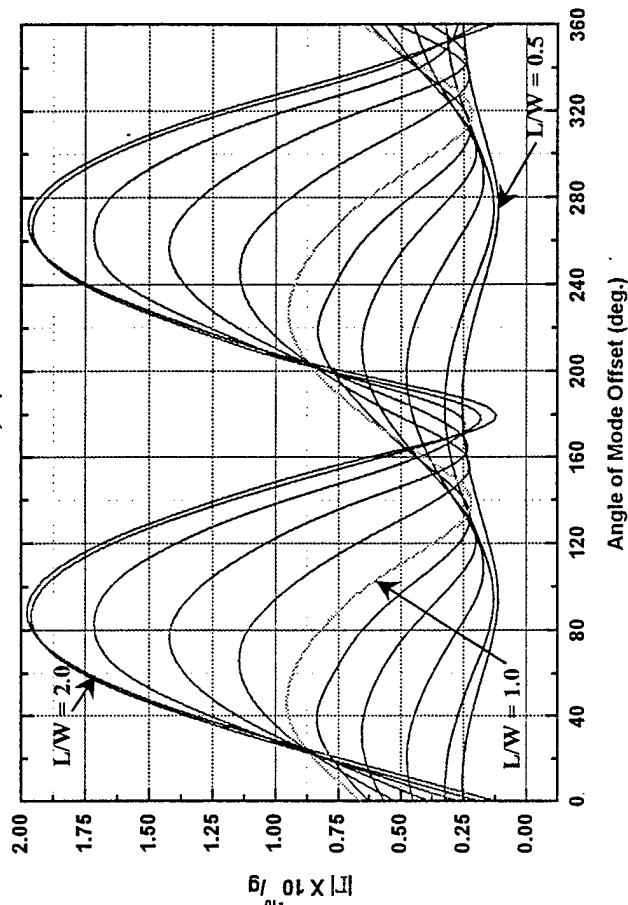
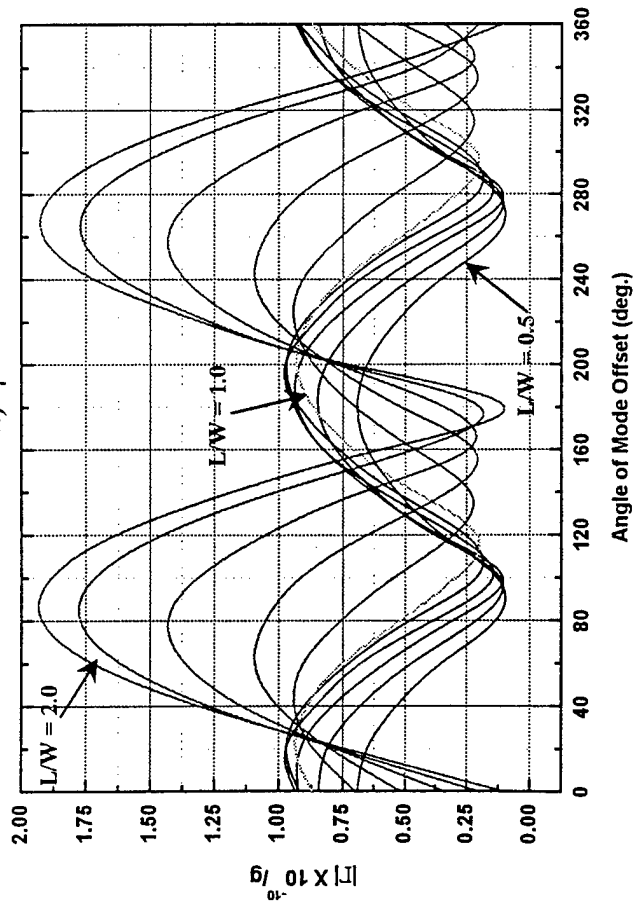
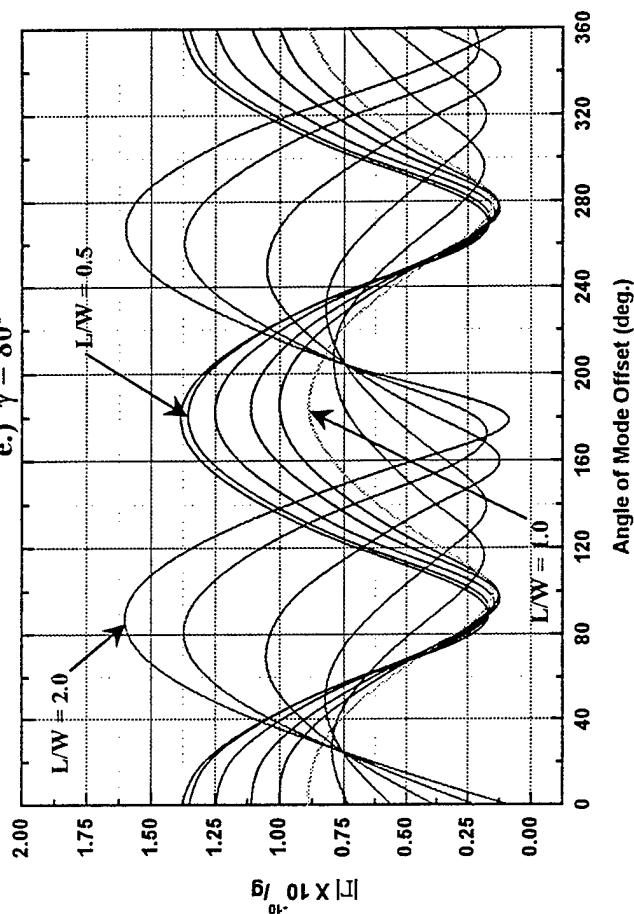


Figure 4.) Sensitivity study for SC Cut

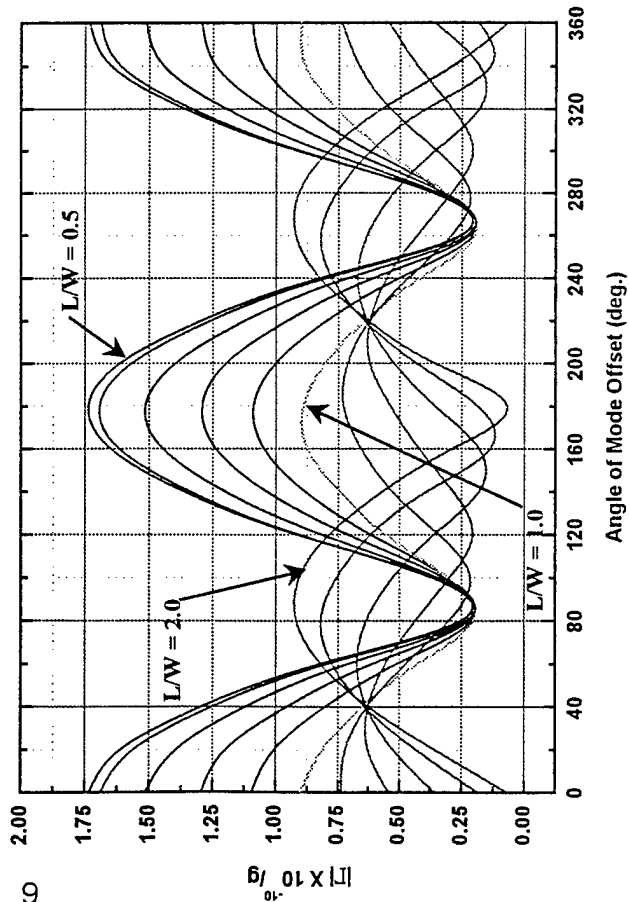
d.)  $\gamma = 60^\circ$



e.)  $\gamma = 80^\circ$



f.)  $\gamma = 100^\circ$



g.)  $\gamma = 120^\circ$

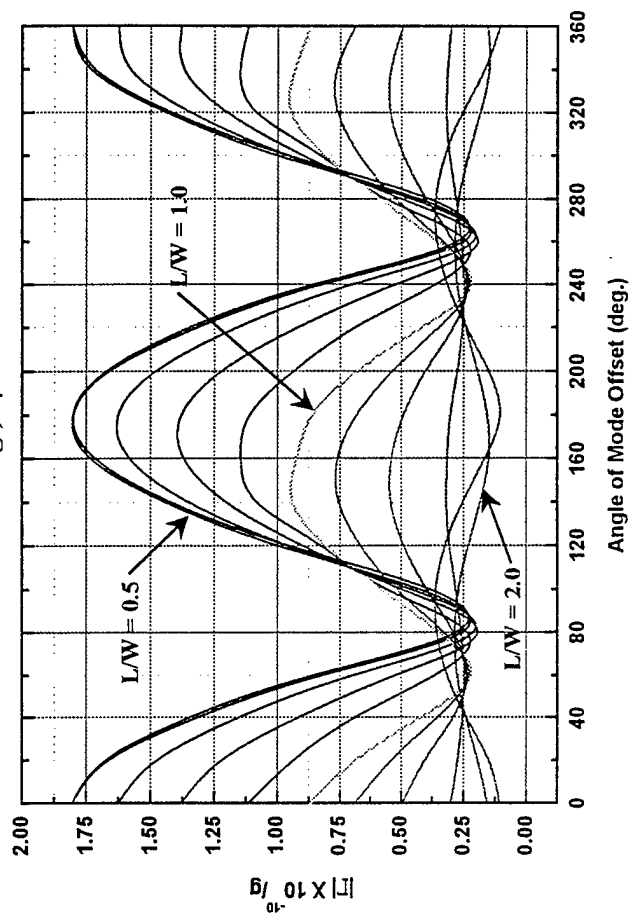


Figure 4.) Sensitivity study for SC Cut



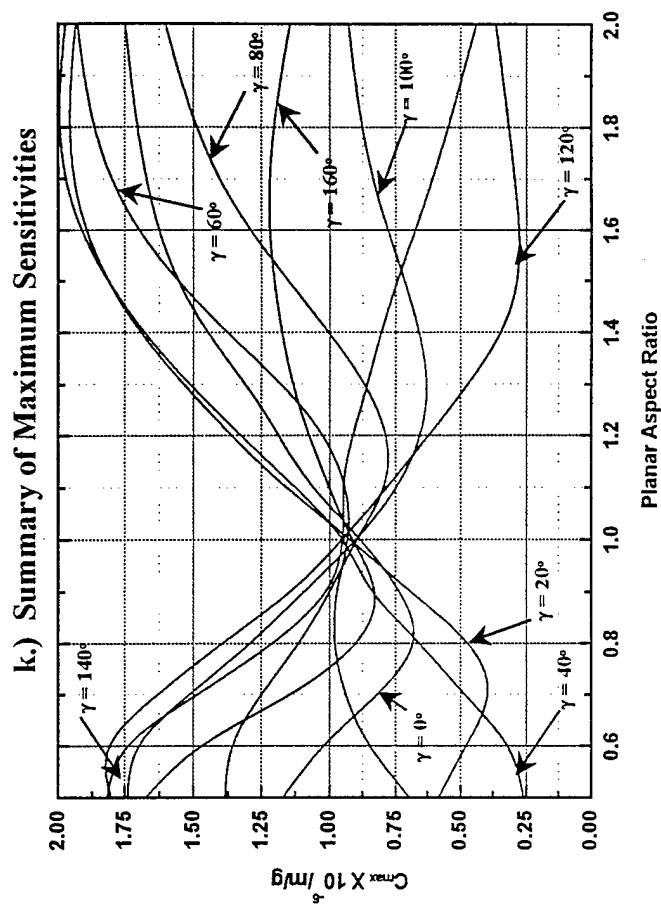
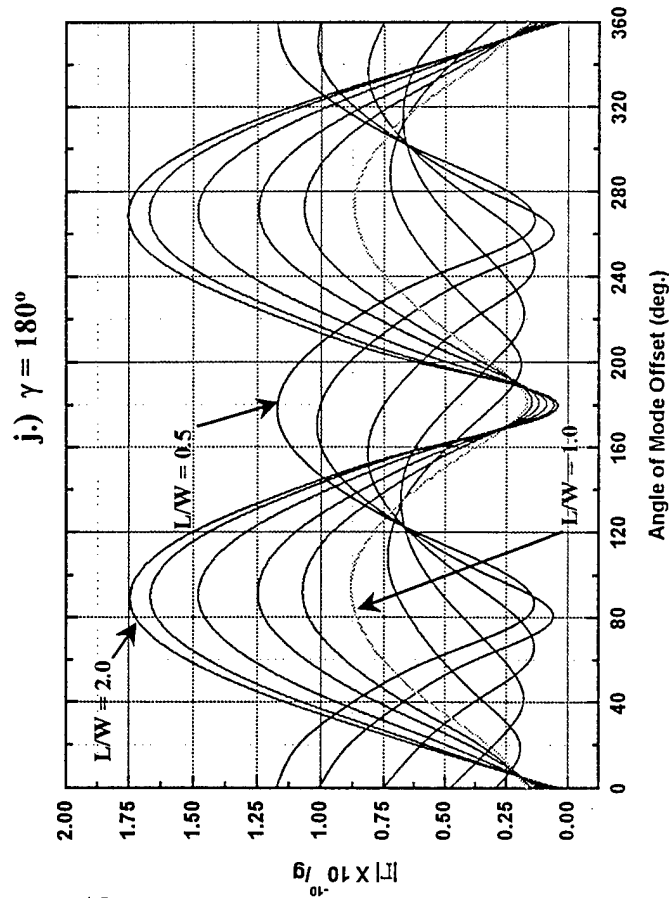
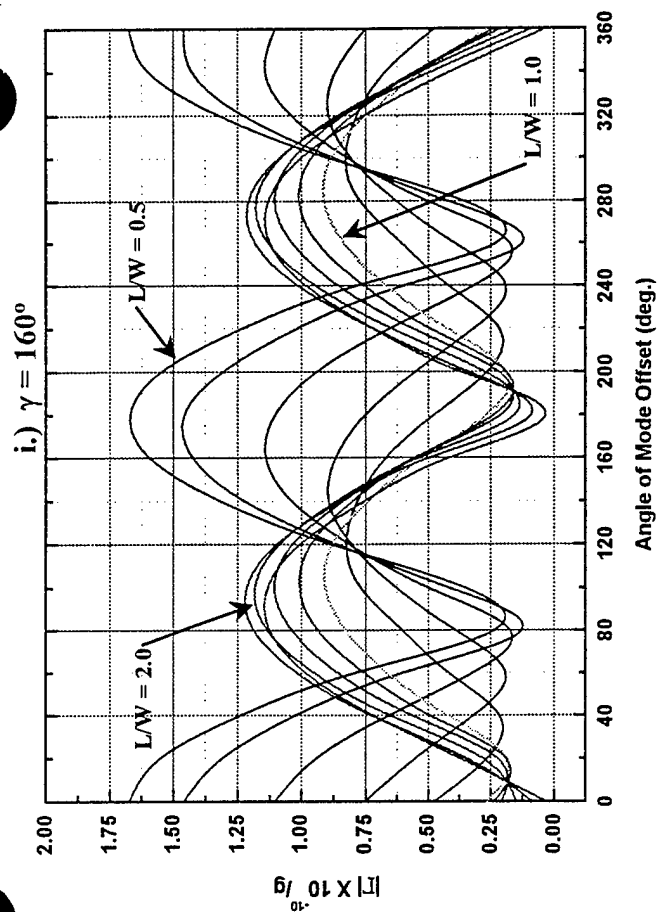
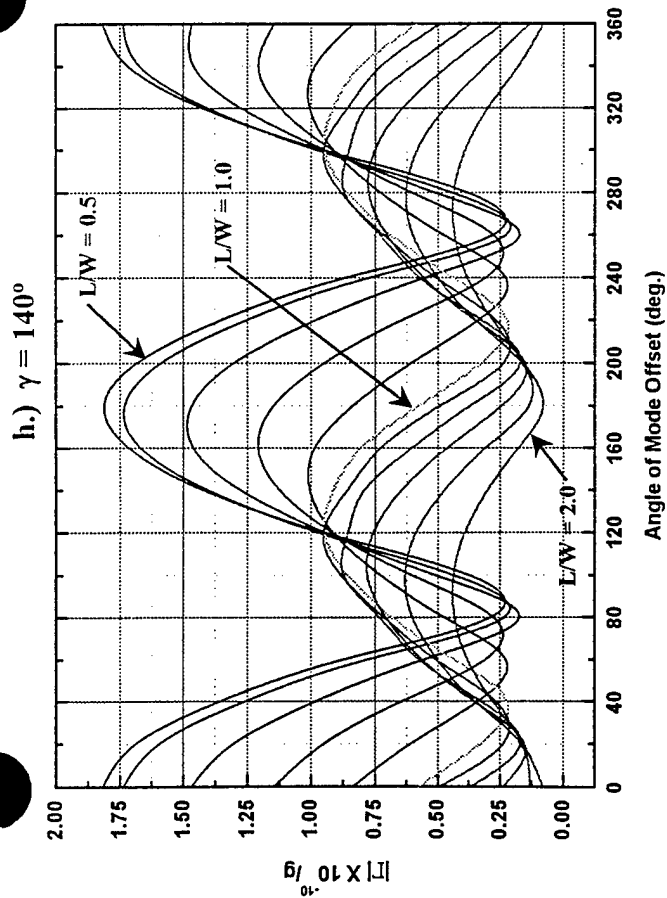


Figure 4.) Sensitivity study for SC Cut

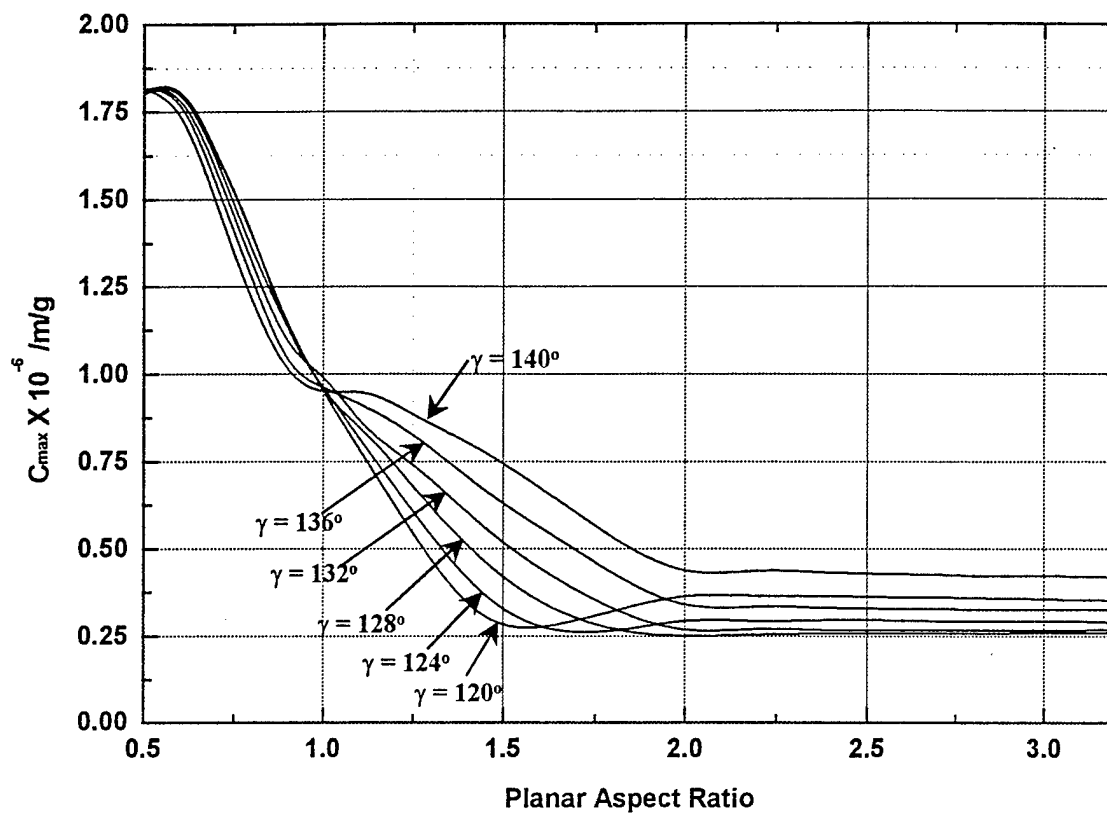


Figure 5.)  $C_{\max}$  for rectangular SC Cut at larger aspect ratios.

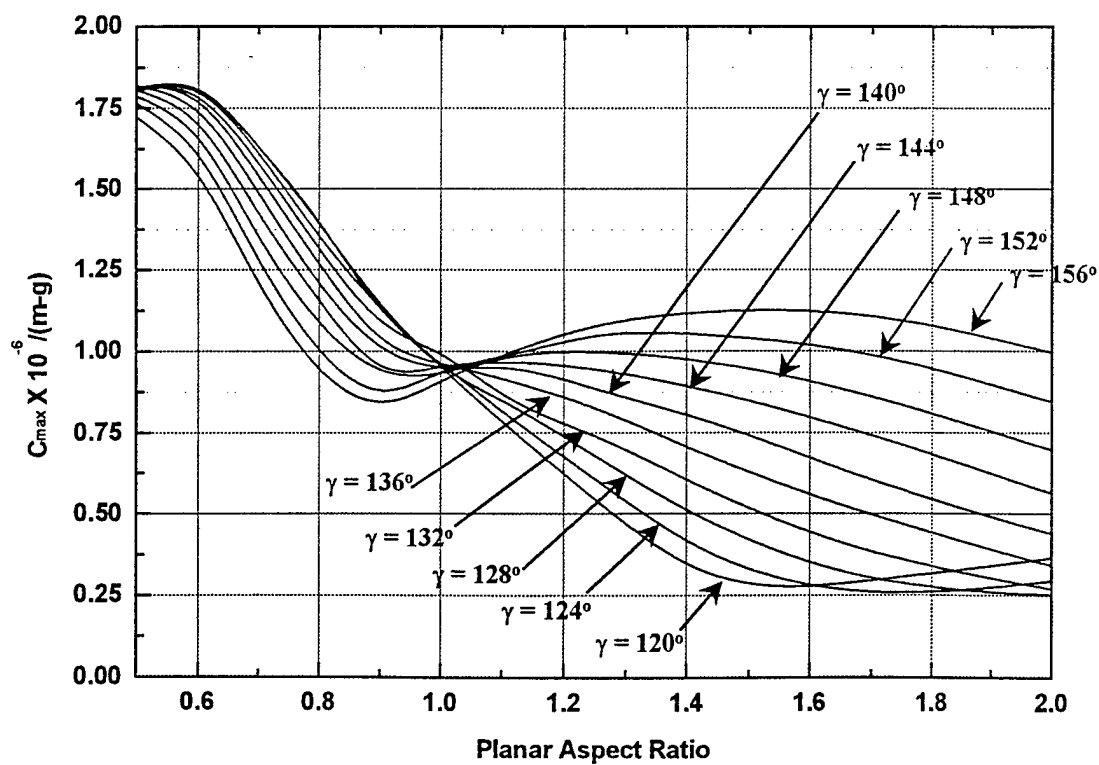


Figure 6.) Refinement of Fig. (4.k) for  $\gamma = 136^\circ - 156^\circ$

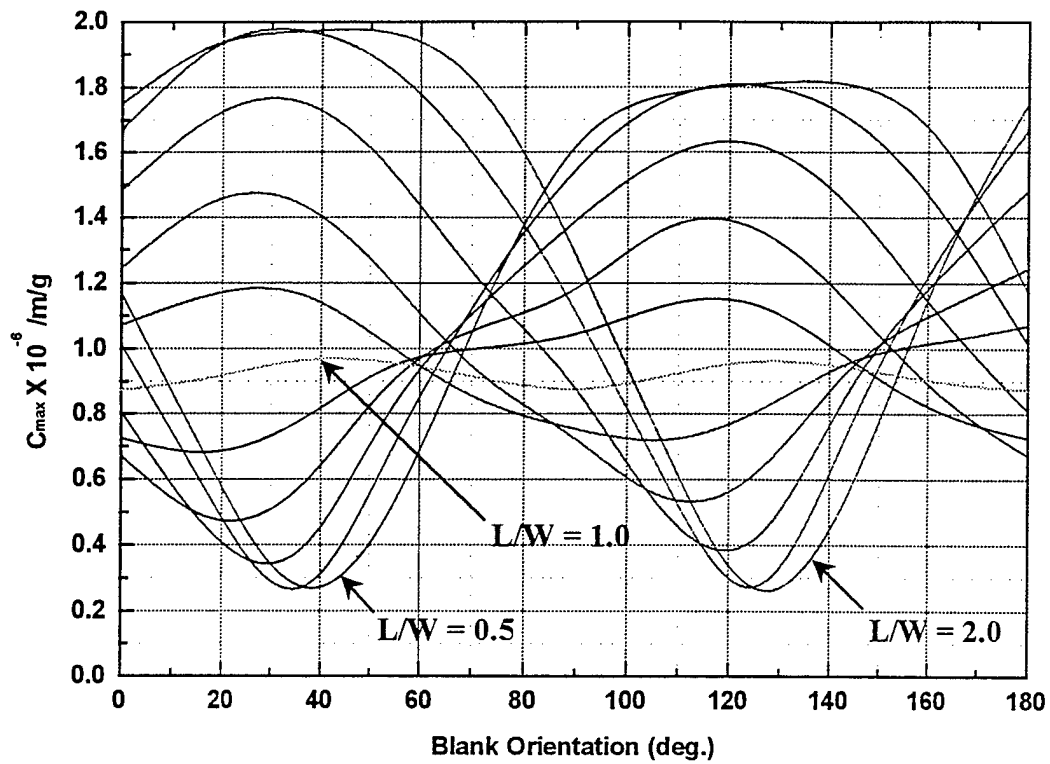


Figure 7.)  $C_{\max}$  vs.  $\gamma$  for SC Cut at various  $L/W$  values for rigid mount along all four edges.

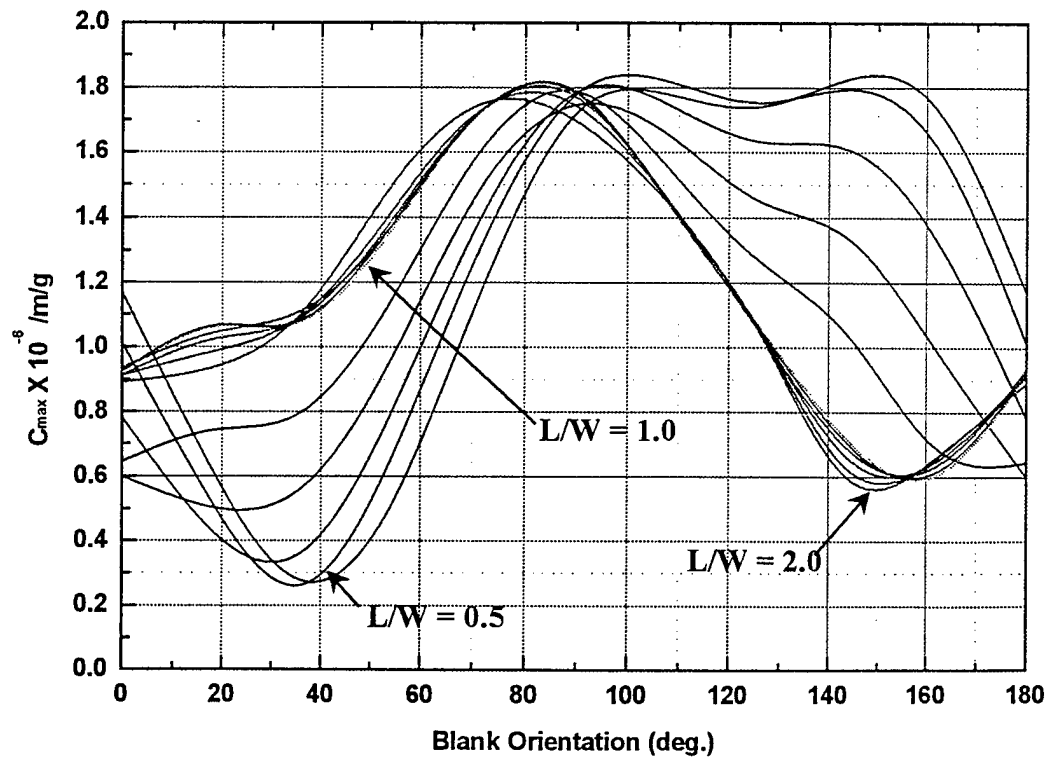
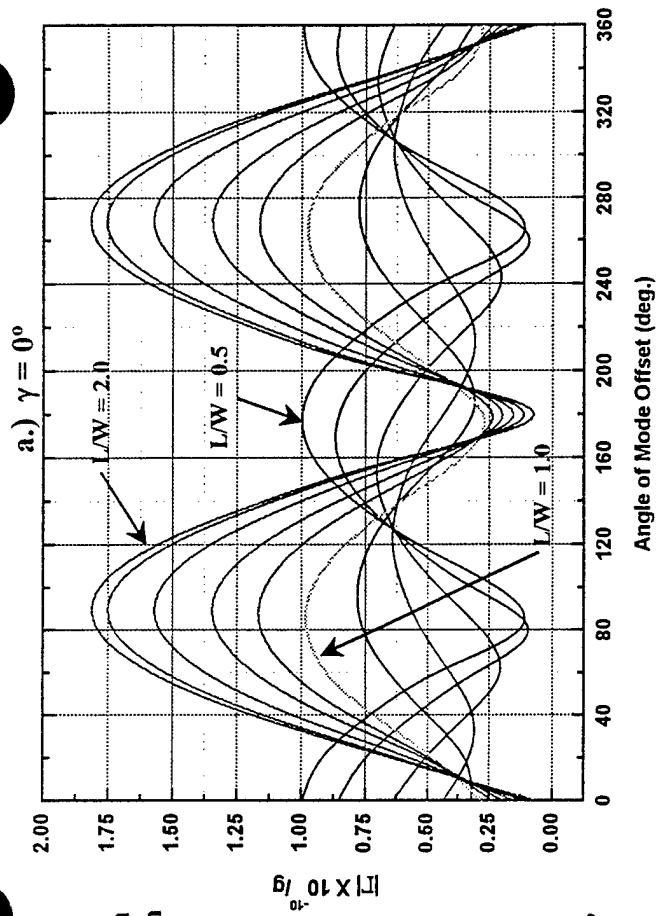
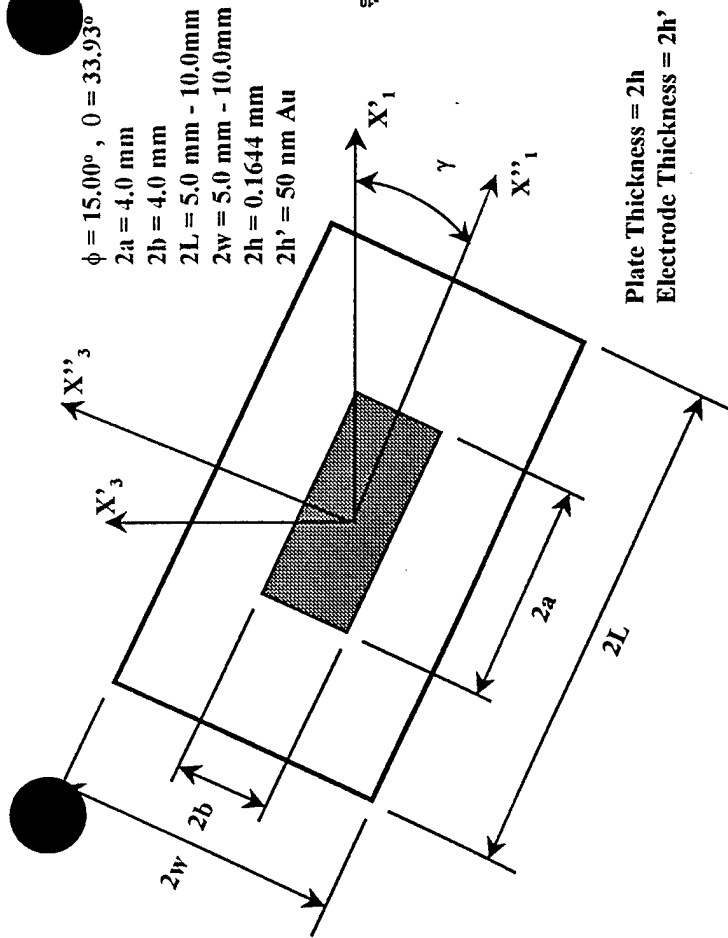
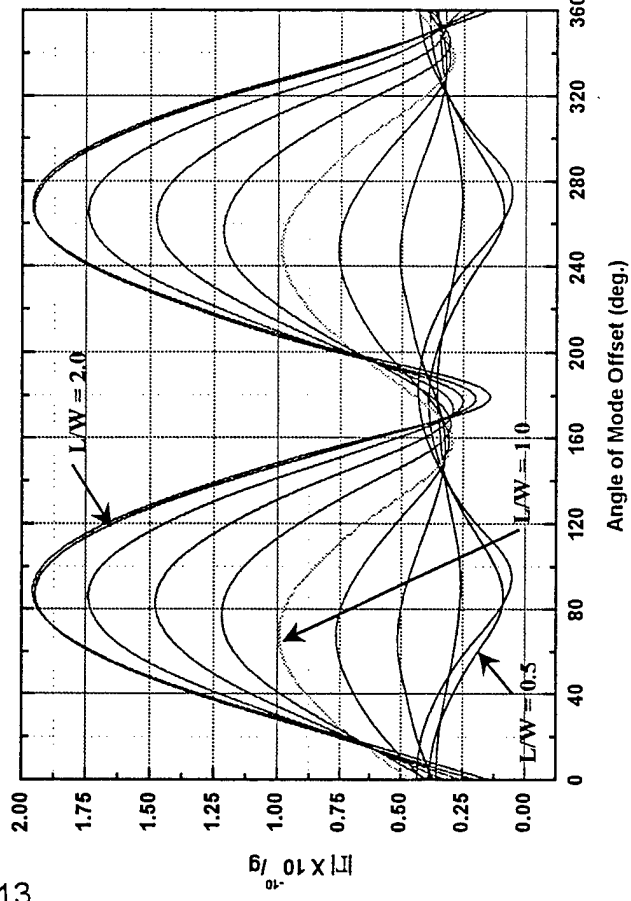


Figure 8.)  $C_{\max}$  vs.  $\gamma$  for SC Cut at various  $L/W$  values for rigid mount along two edges (x-x).



b.)  $\gamma = 20^\circ$



c.)  $\gamma = 40^\circ$

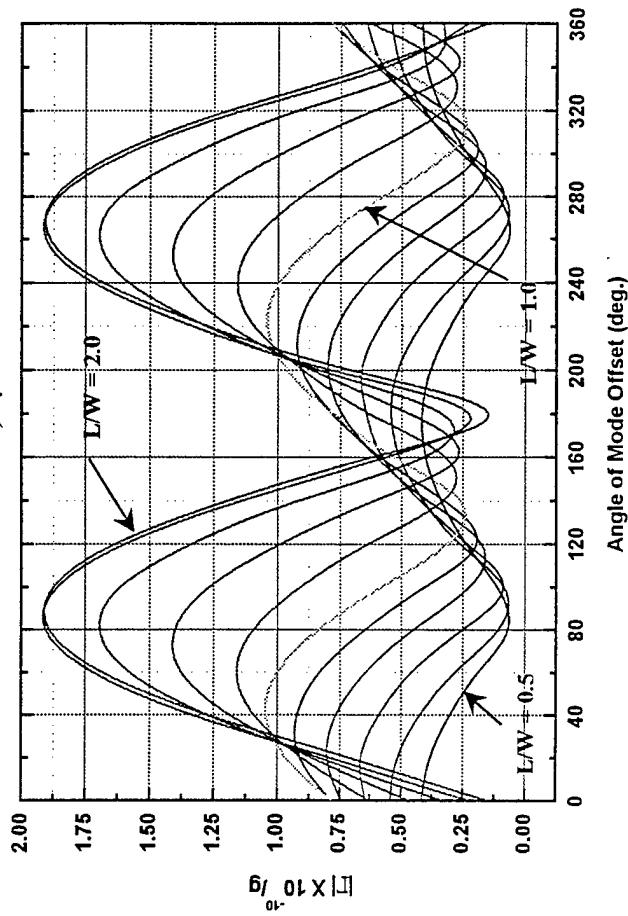
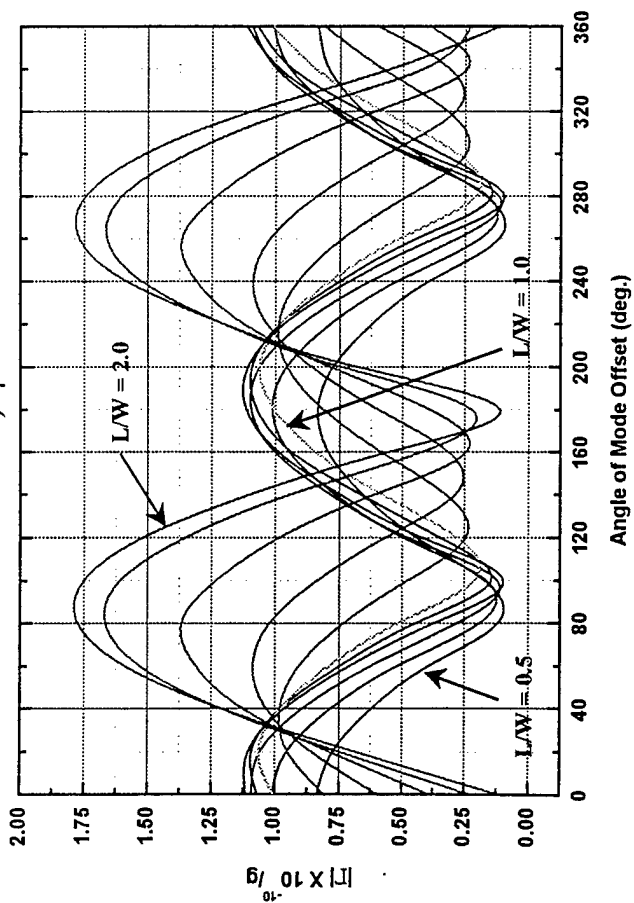
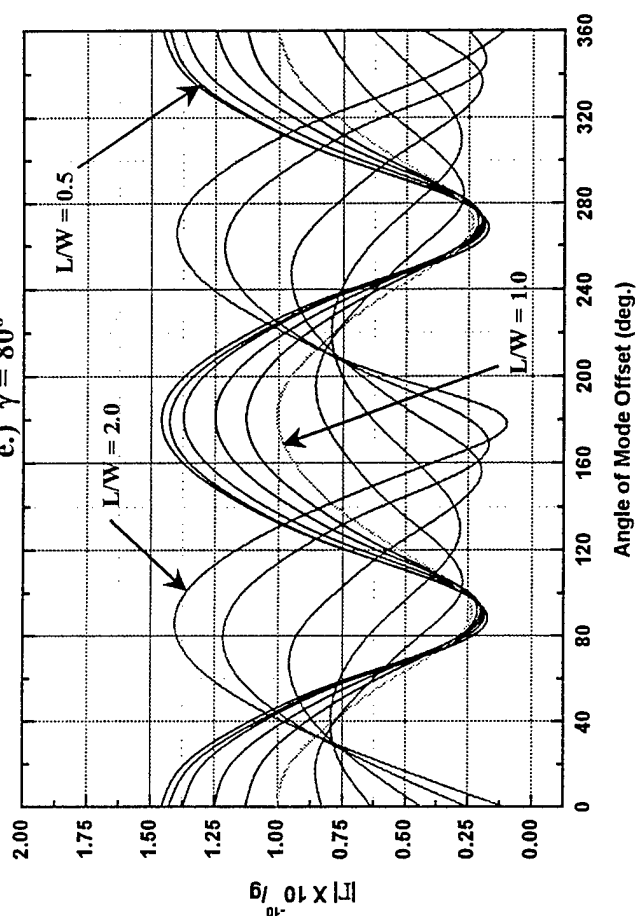


Figure 9.) Sensitivity study for F-C Cut

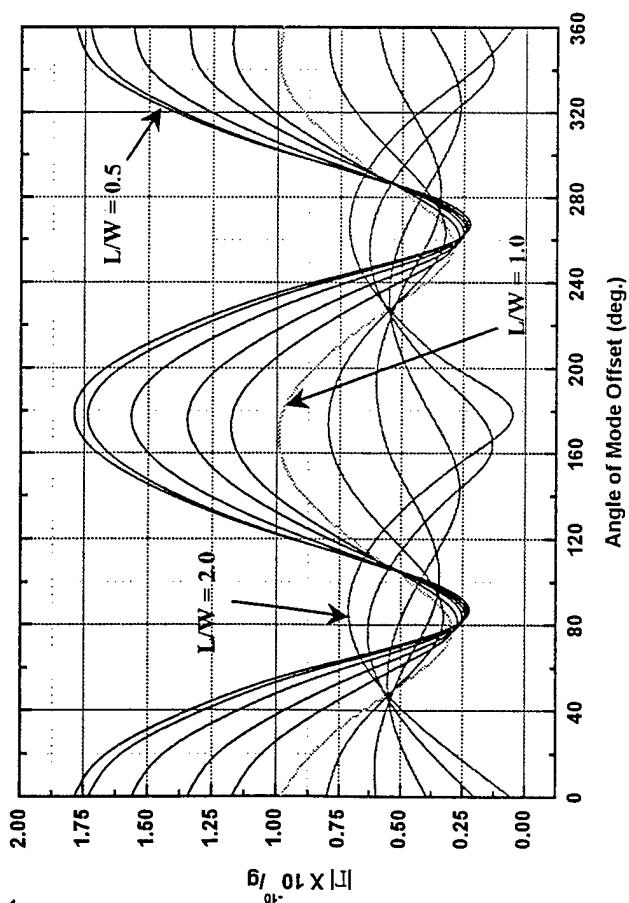
d.)  $\gamma = 60^\circ$



e.)  $\gamma = 80^\circ$



f.)  $\gamma = 100^\circ$



g.)  $\gamma = 120^\circ$

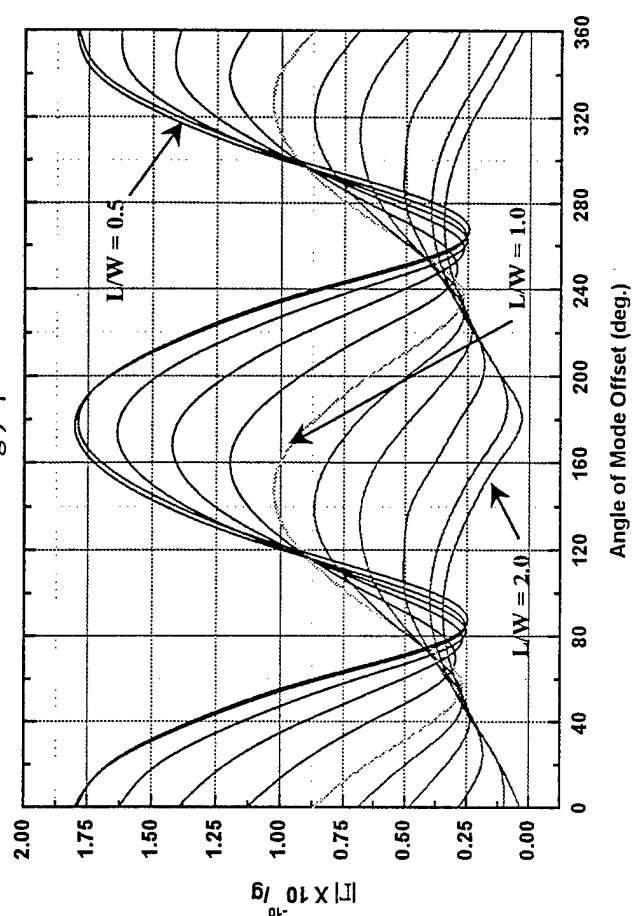
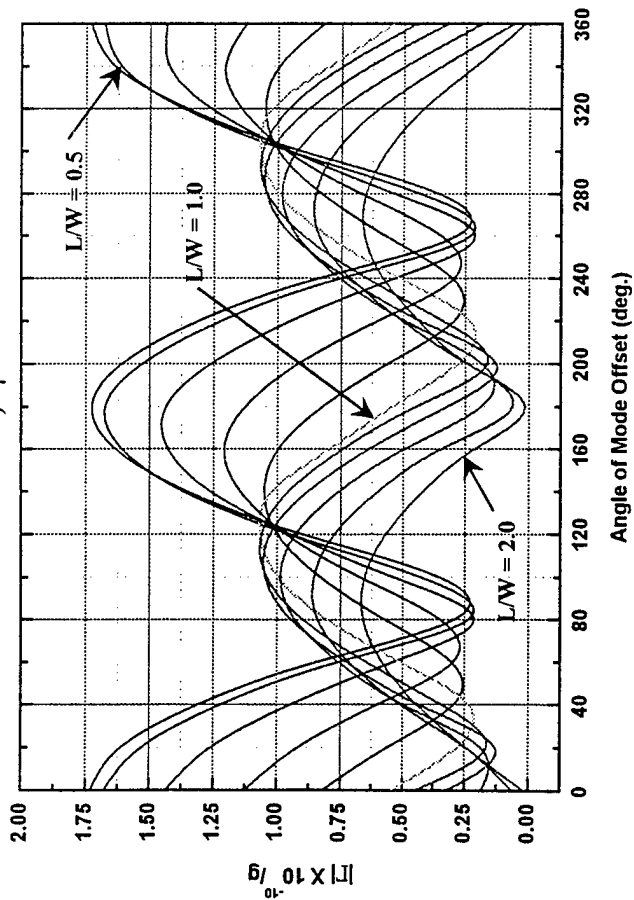
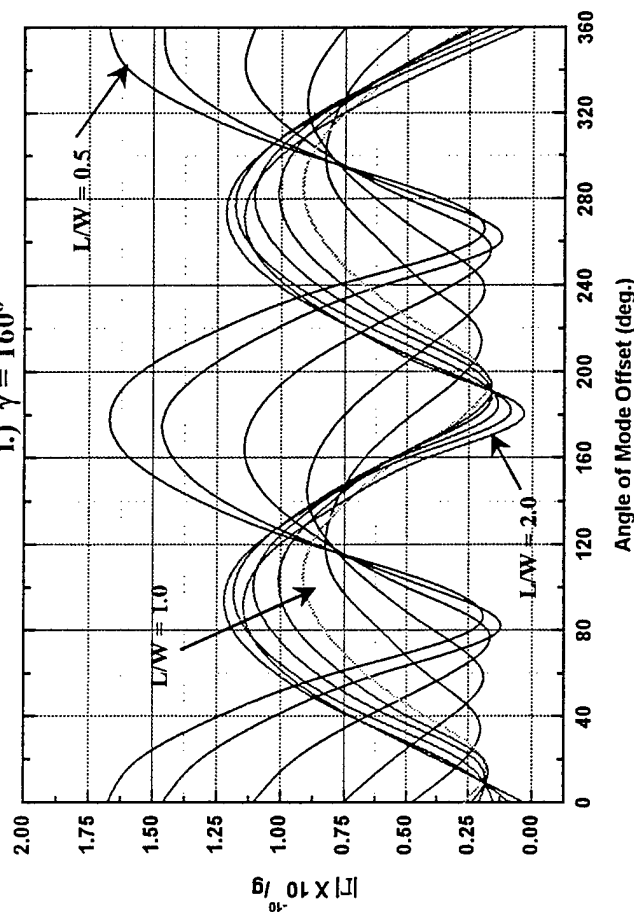


Figure 9.) Sensitivity study for FC Cut

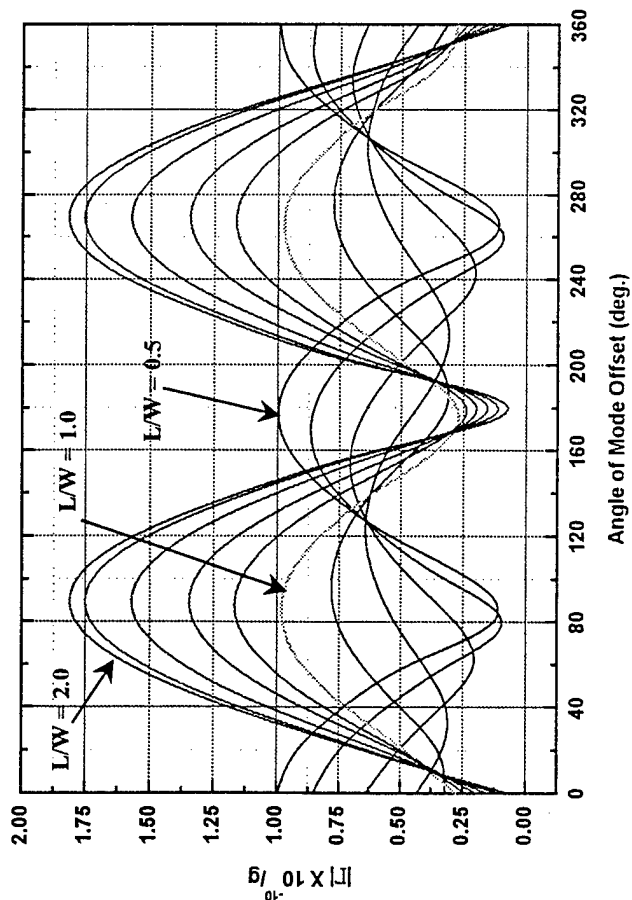
h.)  $\gamma = 140^\circ$



i.)  $\gamma = 160^\circ$



j.)  $\gamma = 180^\circ$



k.) Summary of Maximum Sensitivities

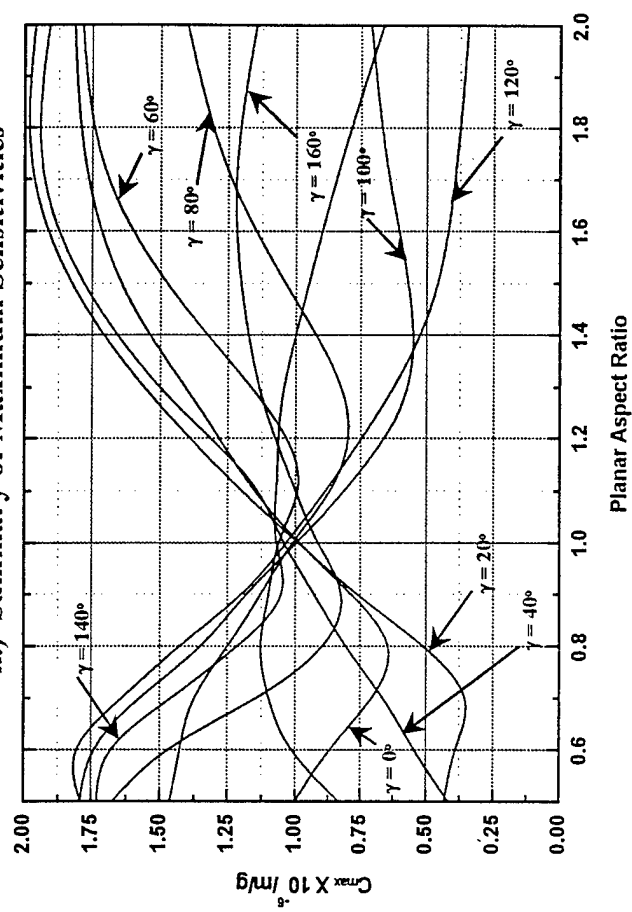
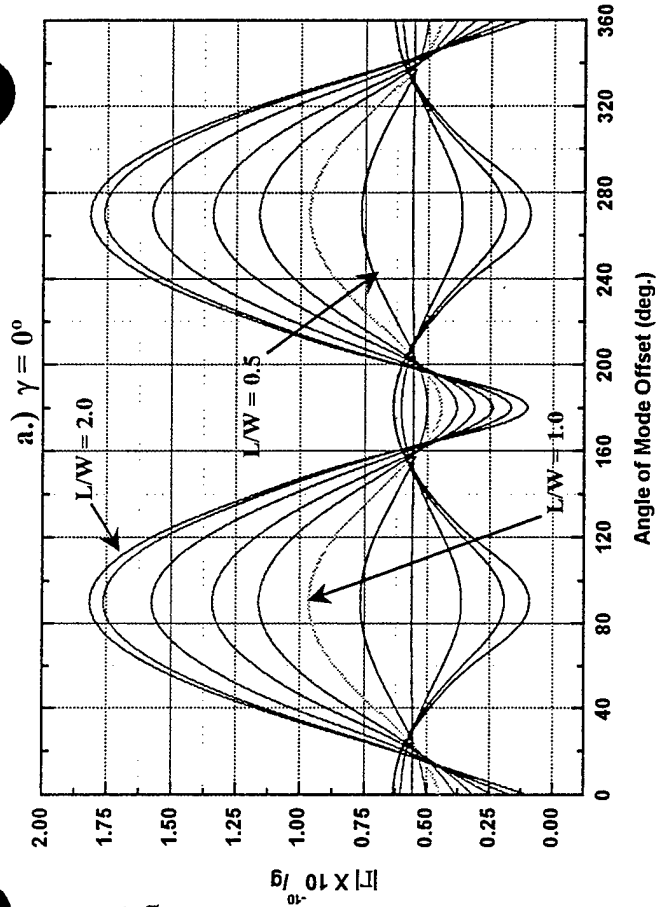
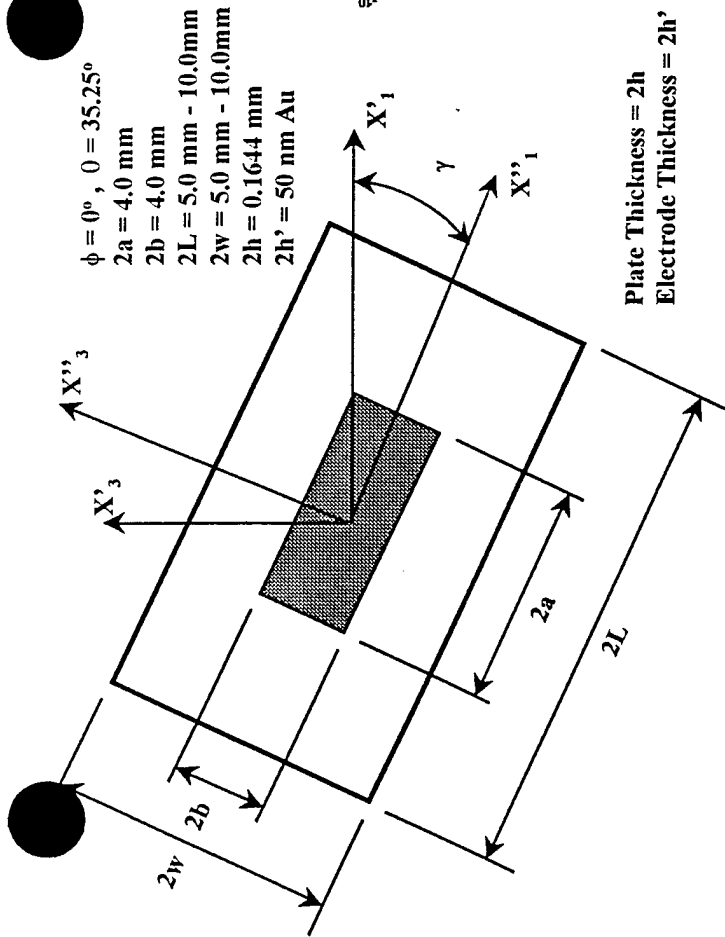
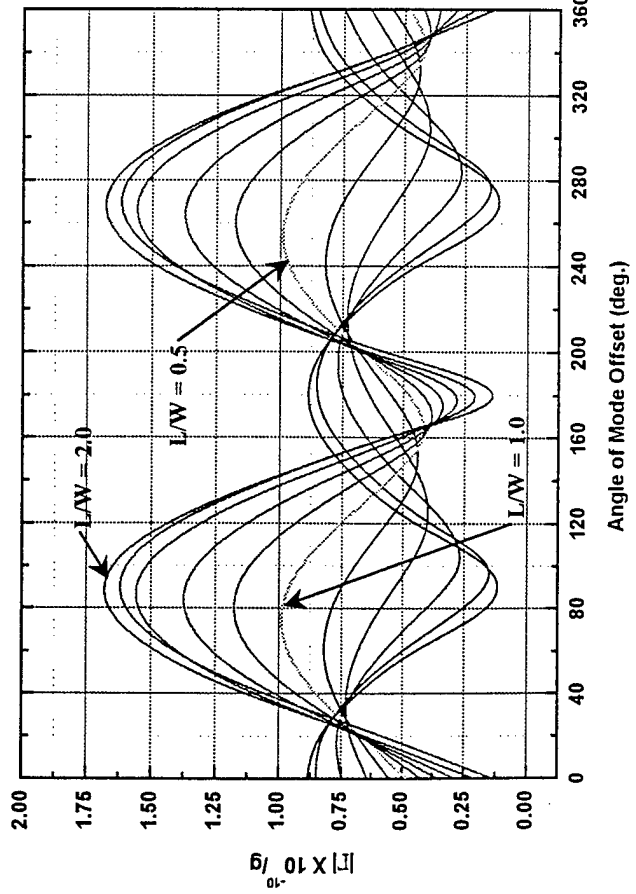


Figure 9.) Sensitivity study for FC Cut



b.)  $\gamma = 20^\circ$



c.)  $\gamma = 40^\circ$

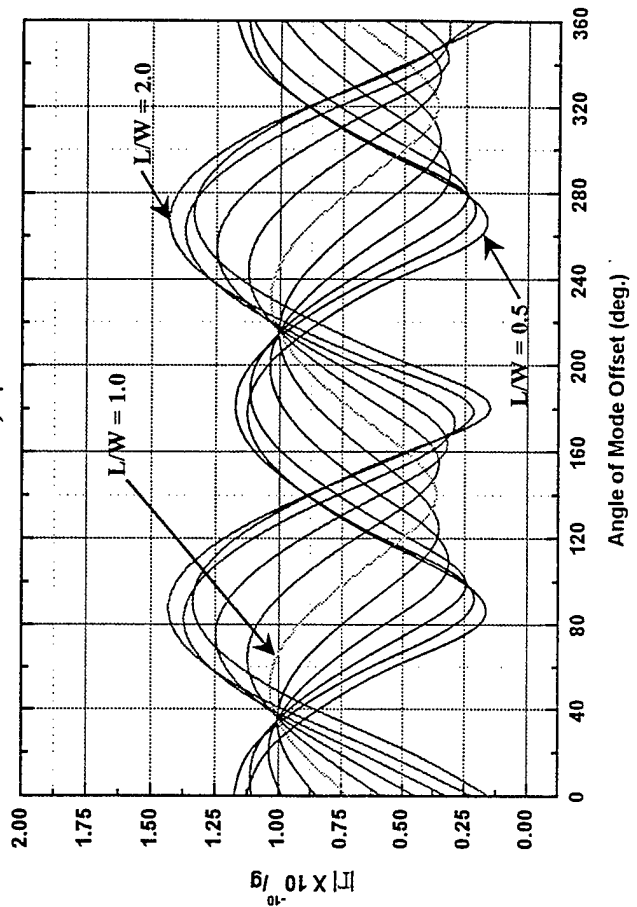


Figure 10.) Sensitivity study for AT Cut

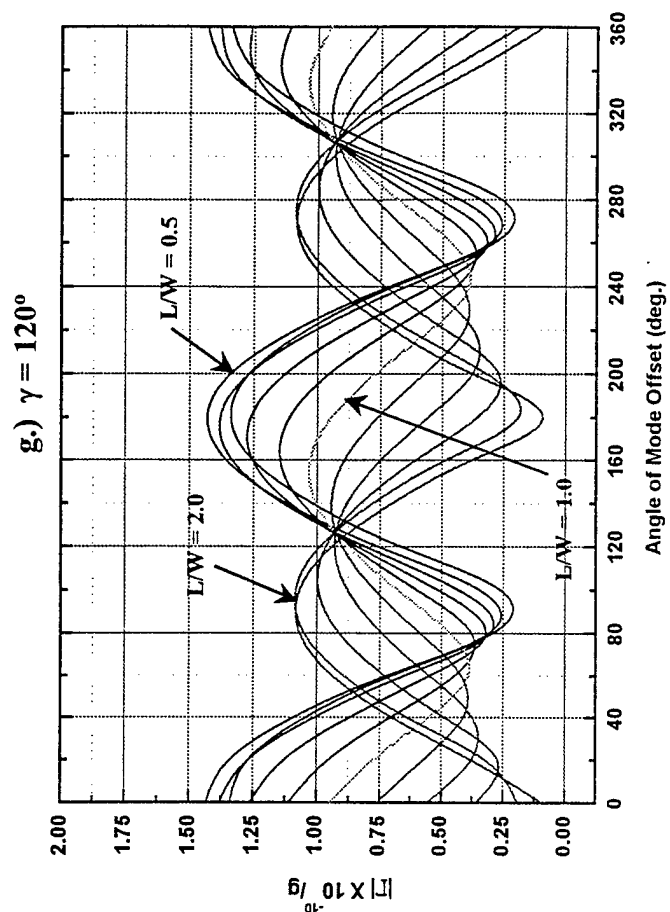
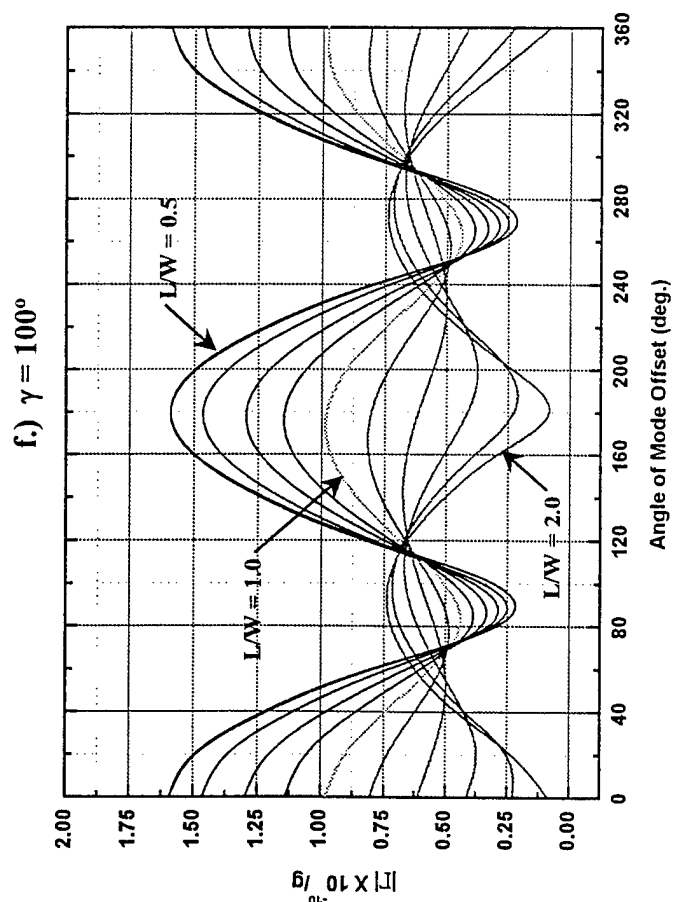
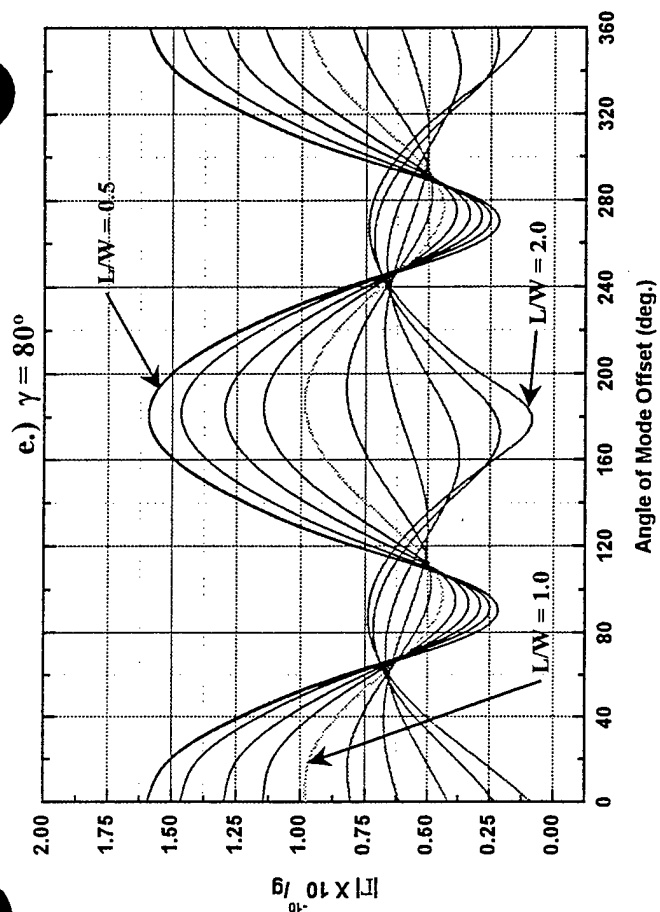
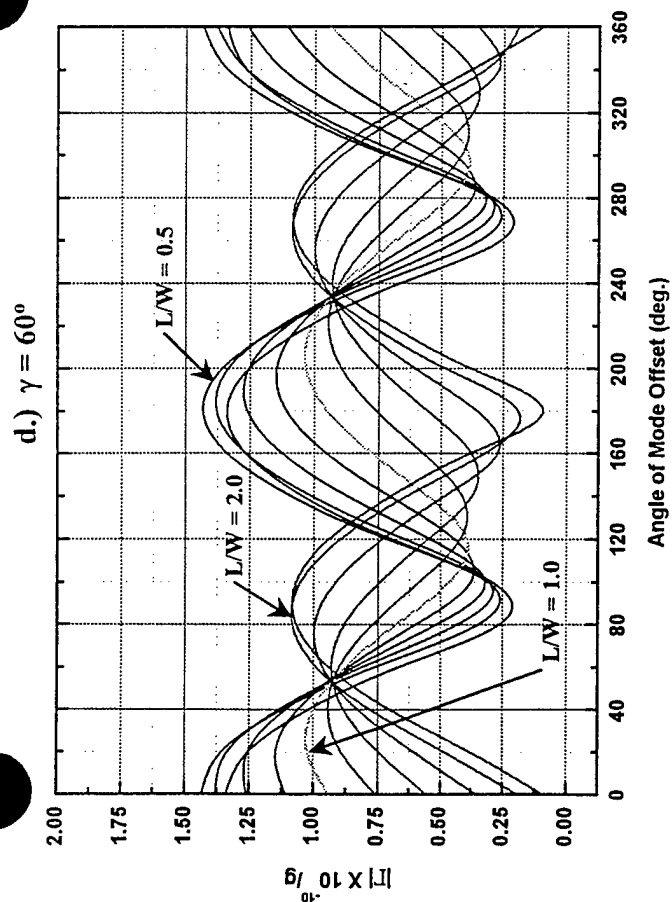


Figure 10.) Sensitivity study for AT Cut



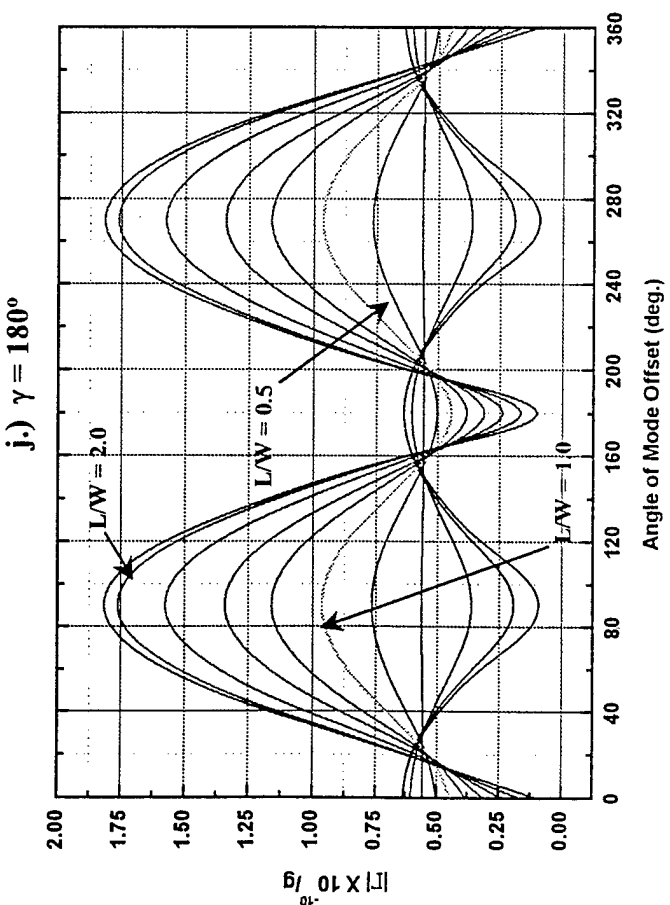
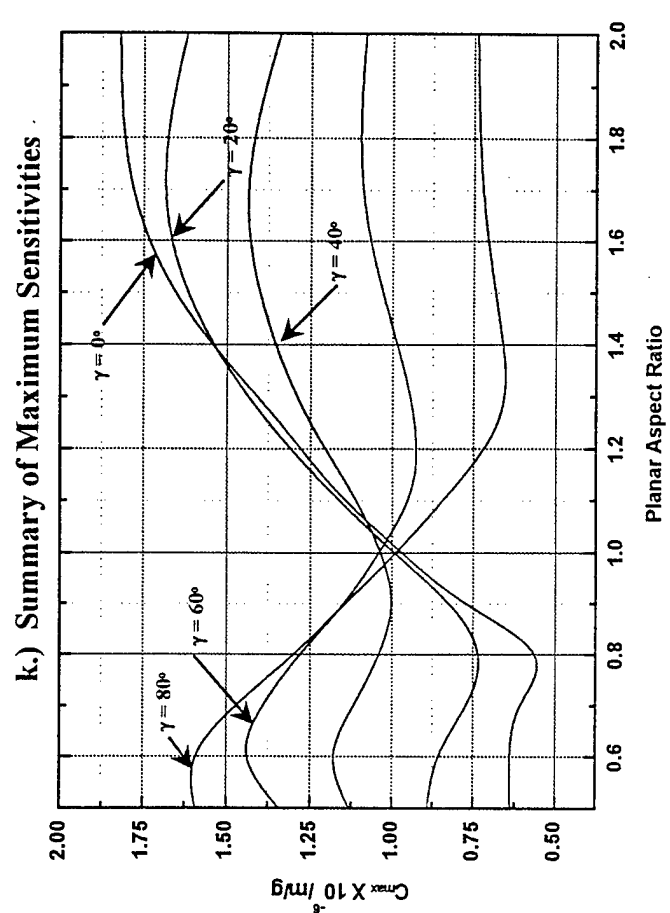
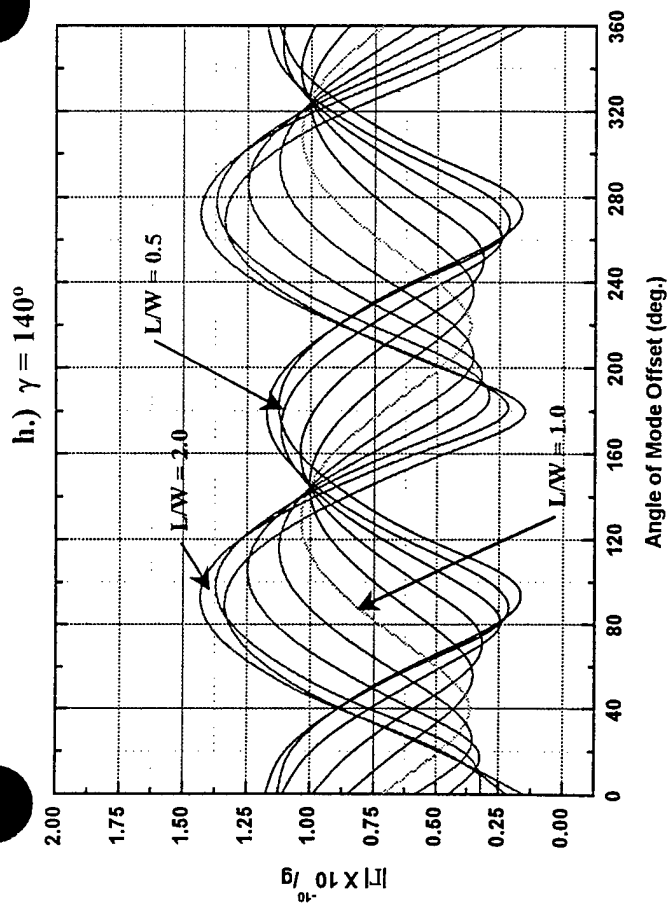
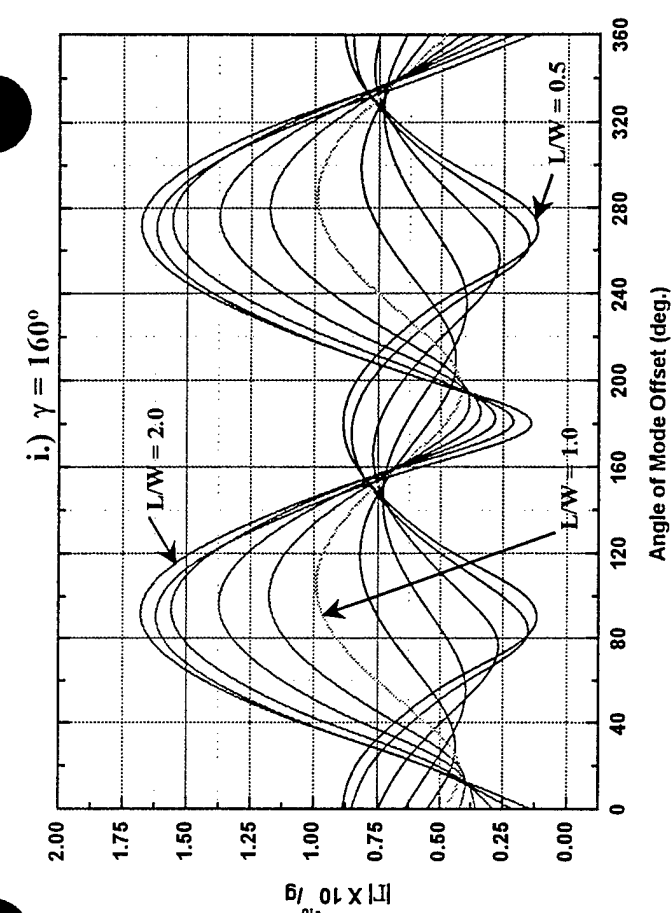


Figure 10.) Sensitivity study for AT Cut

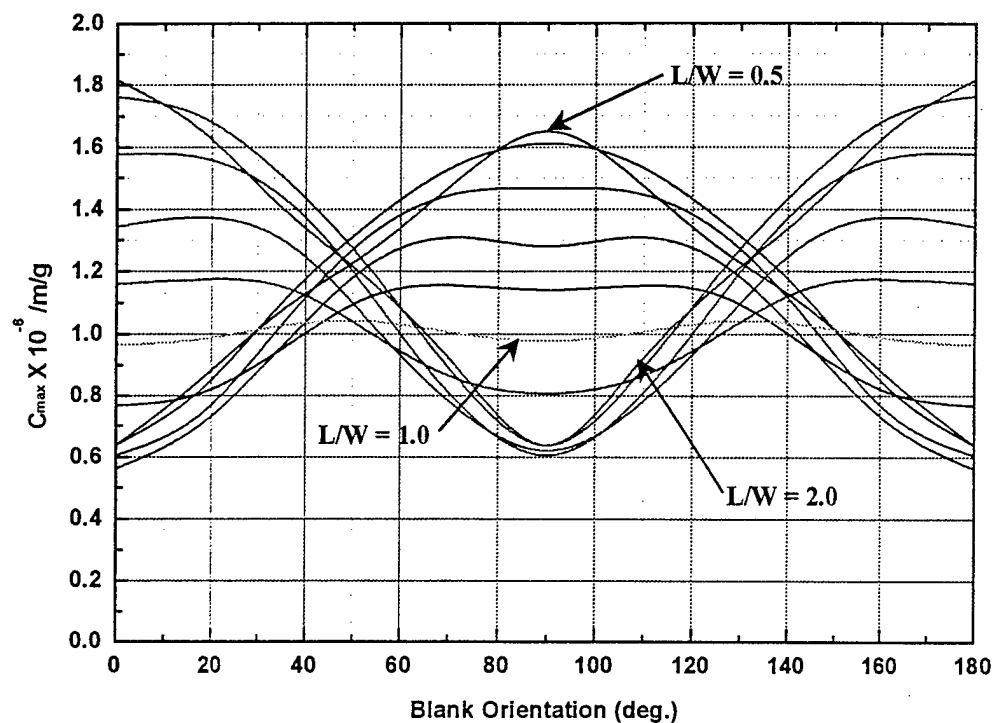


Figure 11.)  $C_{\max}$  vs.  $\gamma$  for AT Cut at various  $L/W$  values for rigid mount along all four edges.

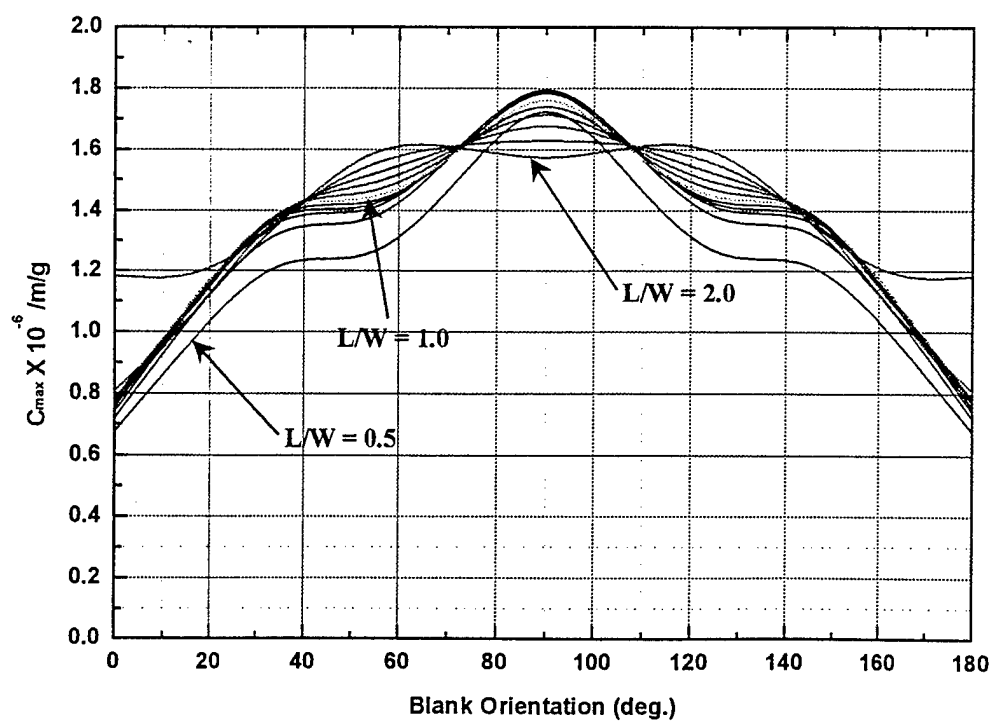
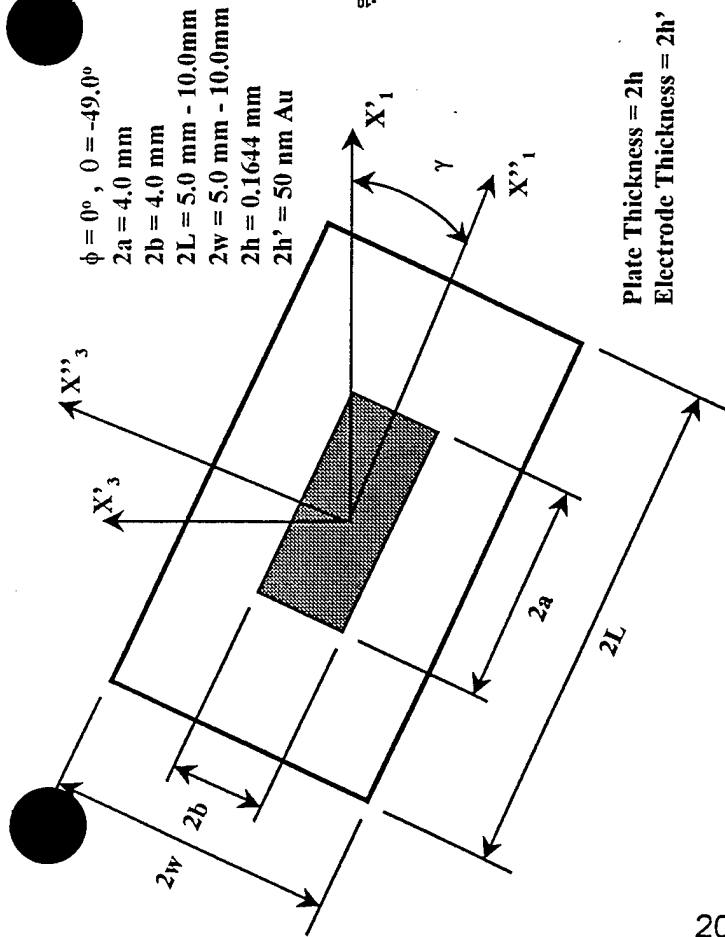
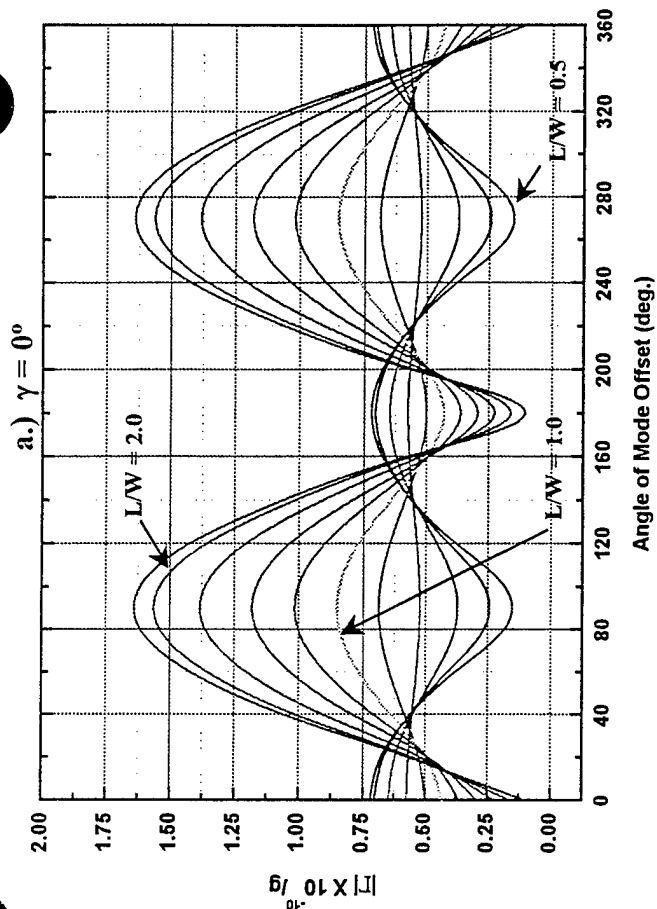


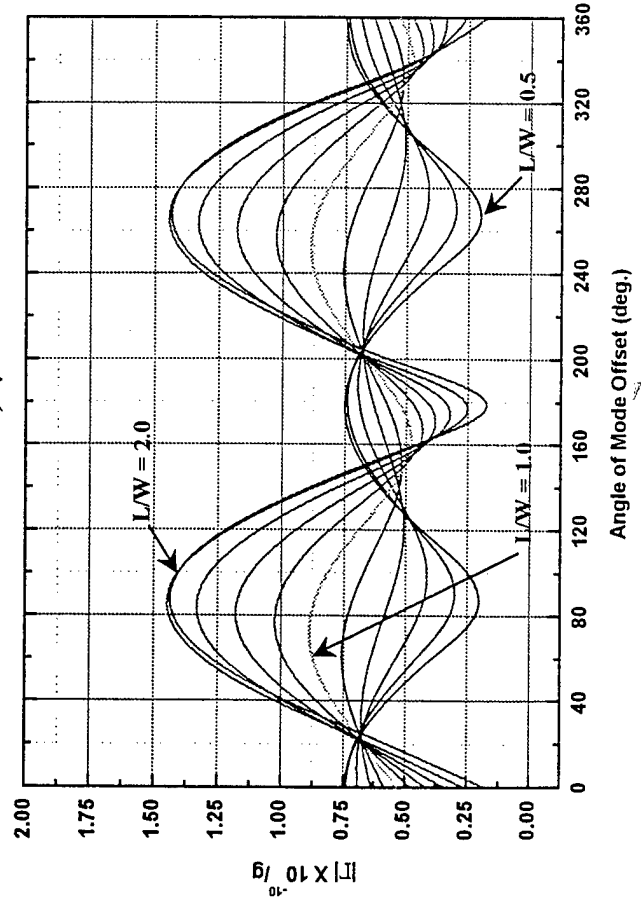
Figure 12.)  $C_{\max}$  vs.  $\gamma$  for AT Cut at various  $L/W$  values for rigid mount along two edges (x-x).



20



b.)  $\gamma = 20^\circ$



c.)  $\gamma = 40^\circ$

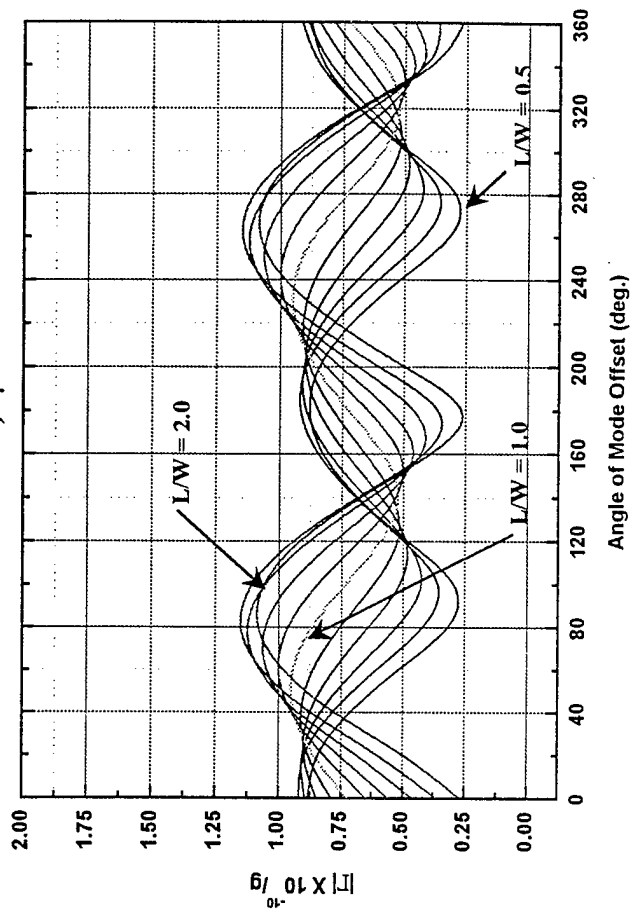


Figure 13.) Sensitivity study for BT Cut

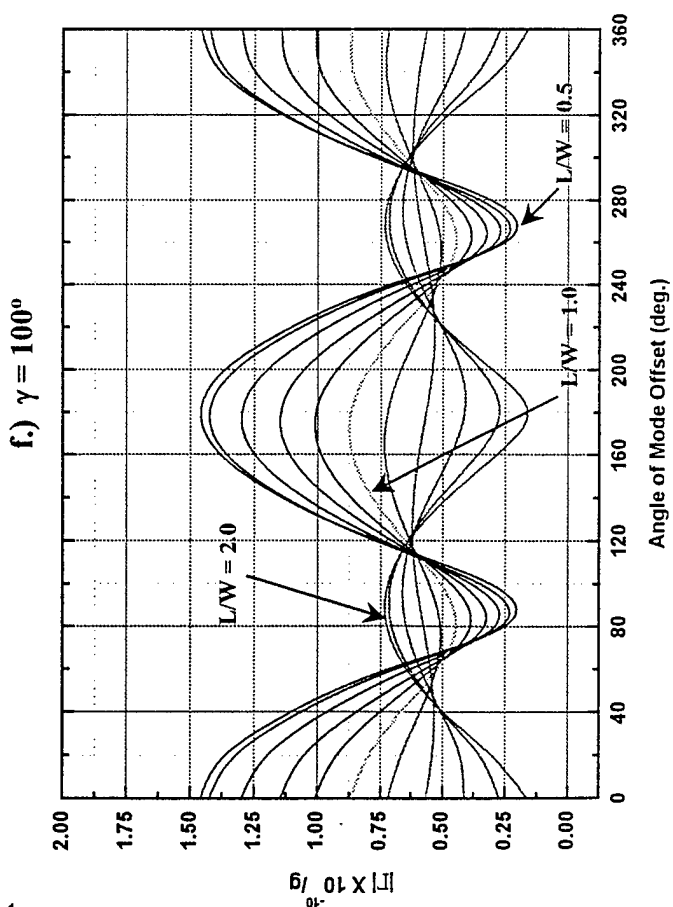
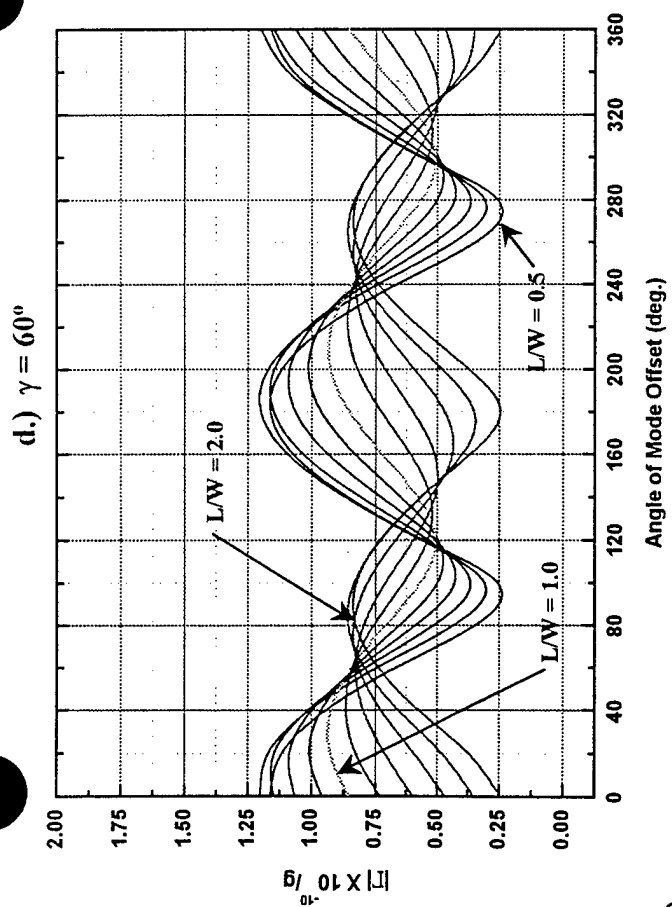
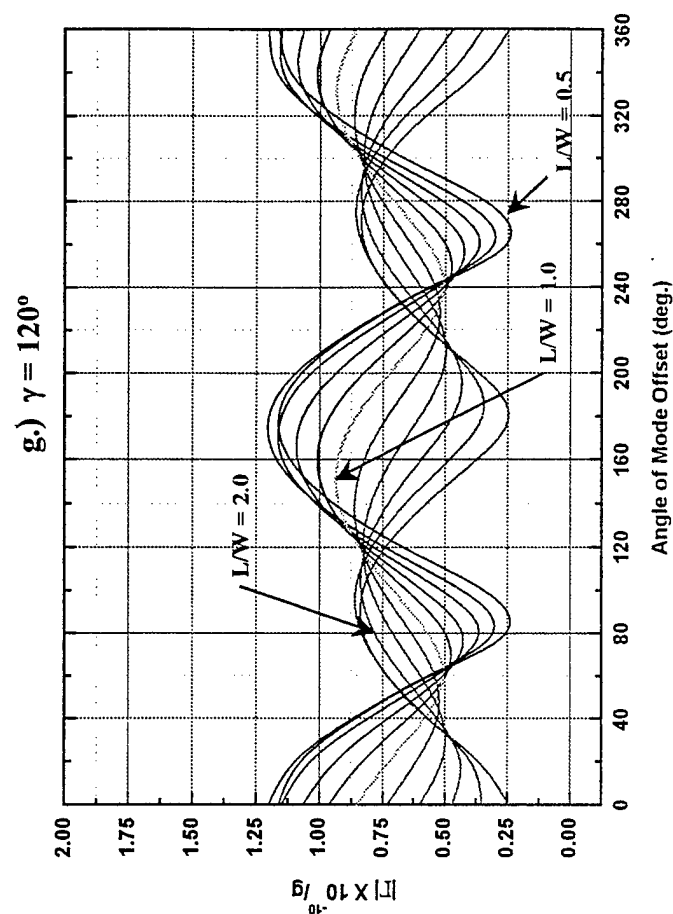
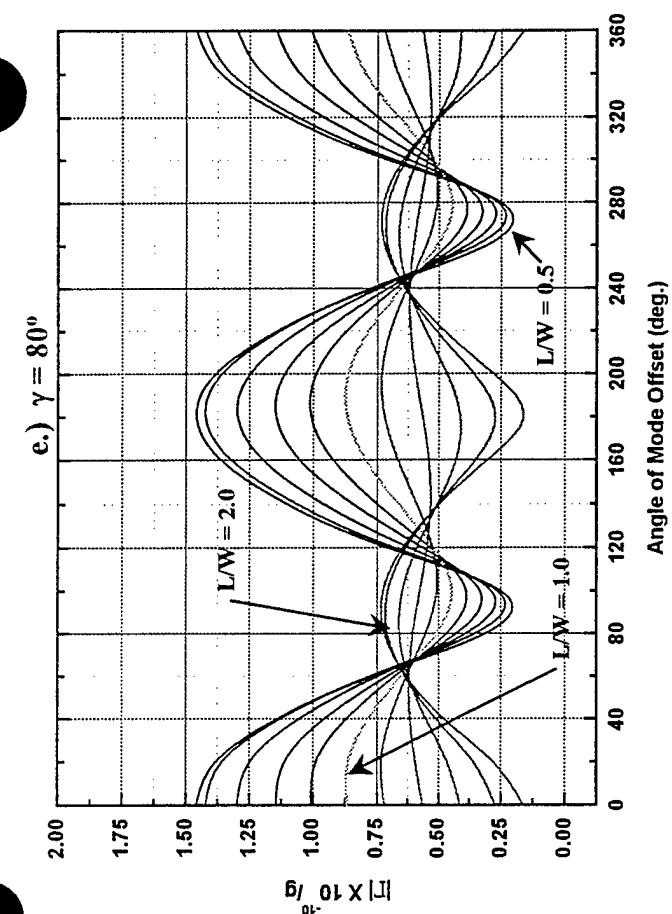
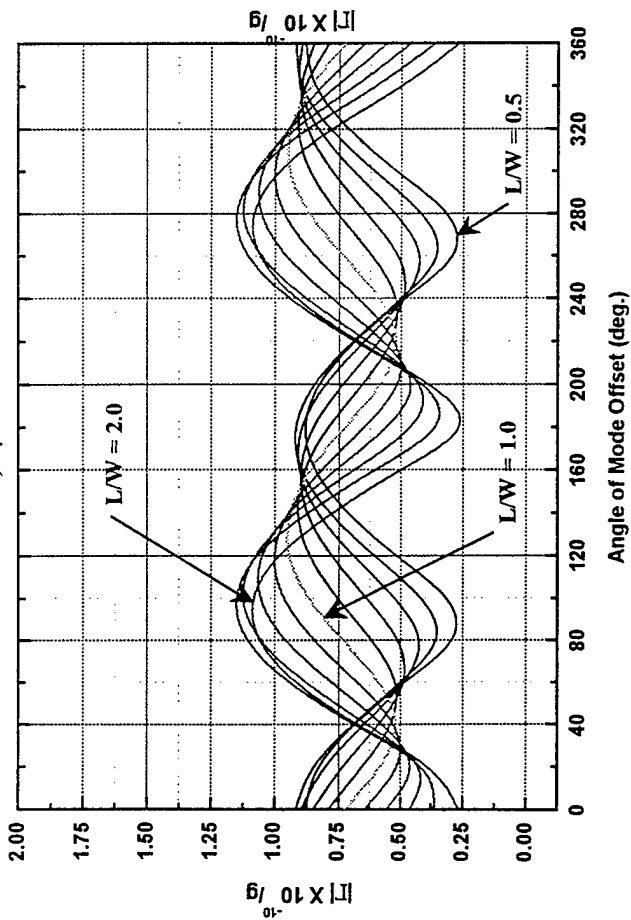
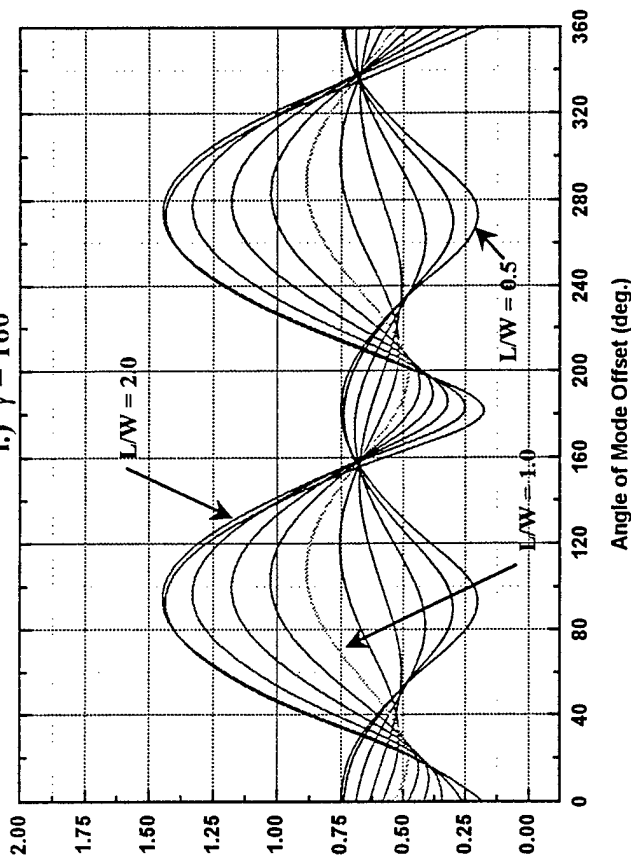


Figure 13.) Sensitivity study for BT Cut

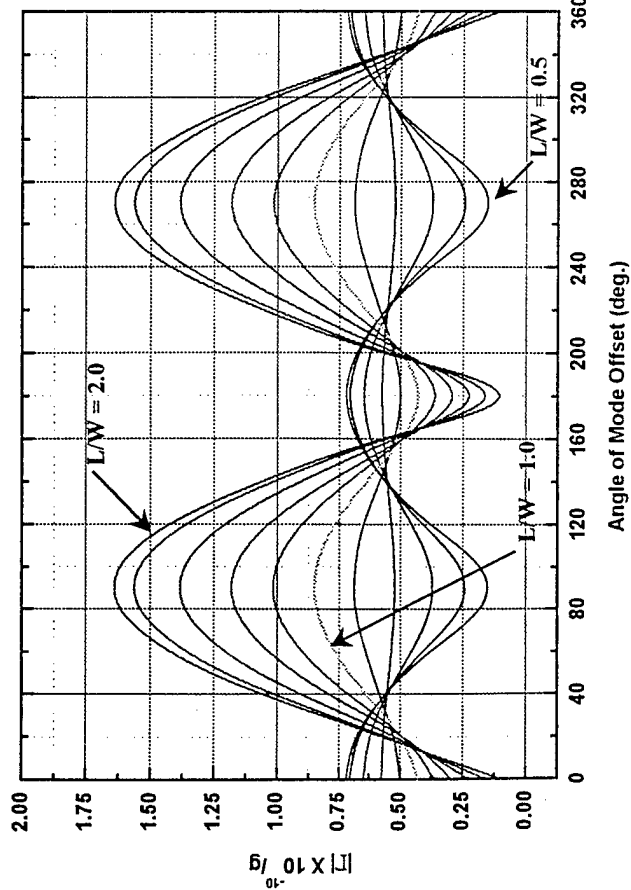
h.)  $\gamma = 140^\circ$



i.)  $\gamma = 160^\circ$



j.)  $\gamma = 180^\circ$



k.) Summary of Maximum Sensitivities

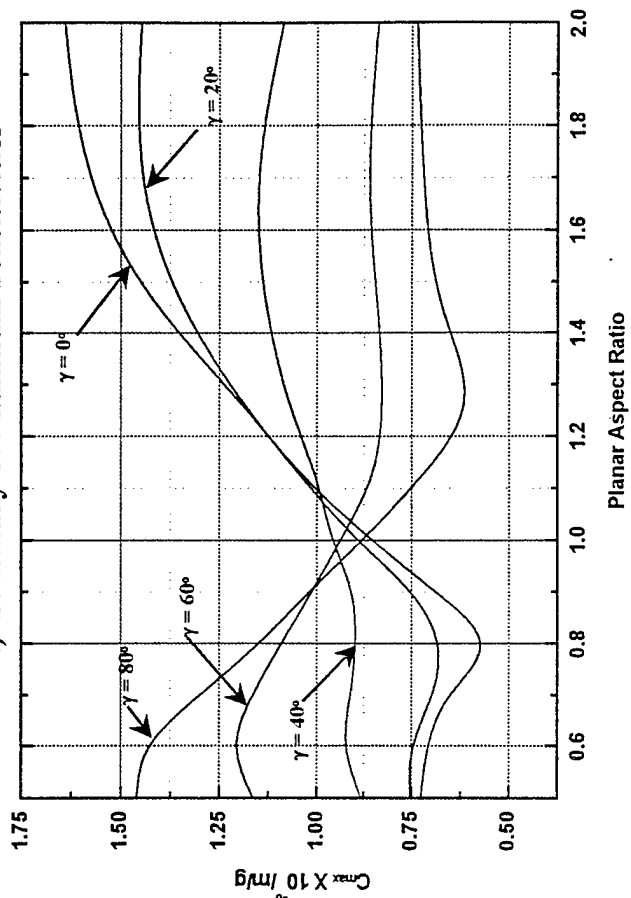


Figure 13.) Sensitivity study for BT Cut

$\phi = 21.93^\circ$ ,  $\theta = 33.93^\circ$   
 $2a = 4.0 \text{ mm}$   
 $2b = 4.0 \text{ mm}$   
 $2L = 5.0 \text{ mm} - 10.0 \text{ mm}$   
 $2w = 5.0 \text{ mm} - 10.0 \text{ mm}$   
 $L_R = 0.0508 \text{ mm}$   
 $w_R = w + 0.5 \text{ mm}$   
 $L_0 = \text{varies}$   
 $H_c = 0.254 \text{ mm}$   
 $2h = 0.1644 \text{ mm}$   
 $2h' = 50 \text{ nm Au}$

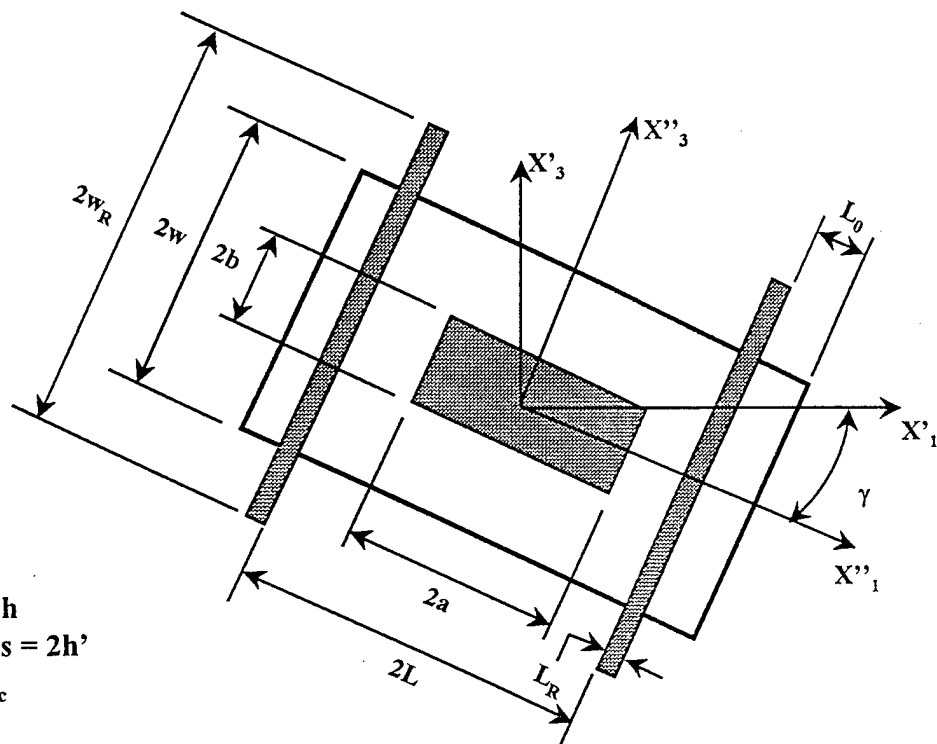


Plate Thickness =  $2h$   
 Electrode Thickness =  $2h'$   
 Ribbon Height =  $H_c$

a.)  $L_0 = 0.25 \text{ mm}$

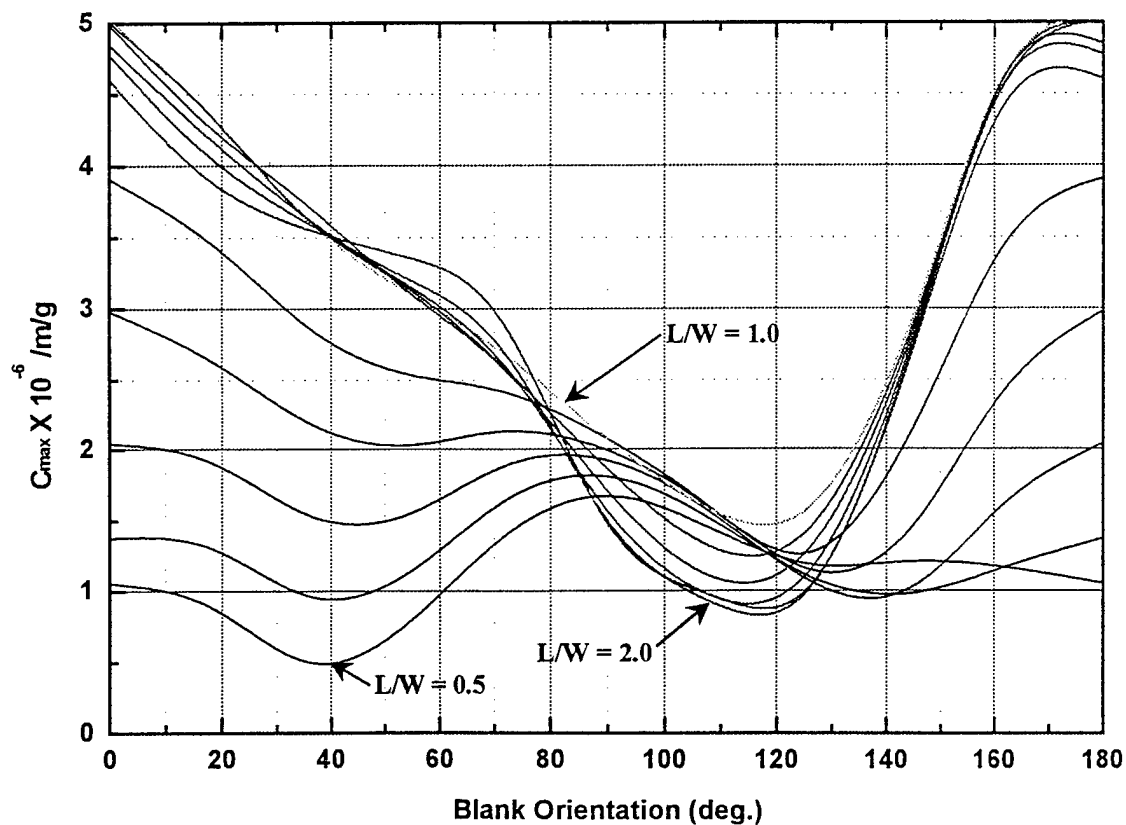


Figure 14.) Mode mispositioning analysis for slotted ribbon mounted rectangular SC Cut plate.

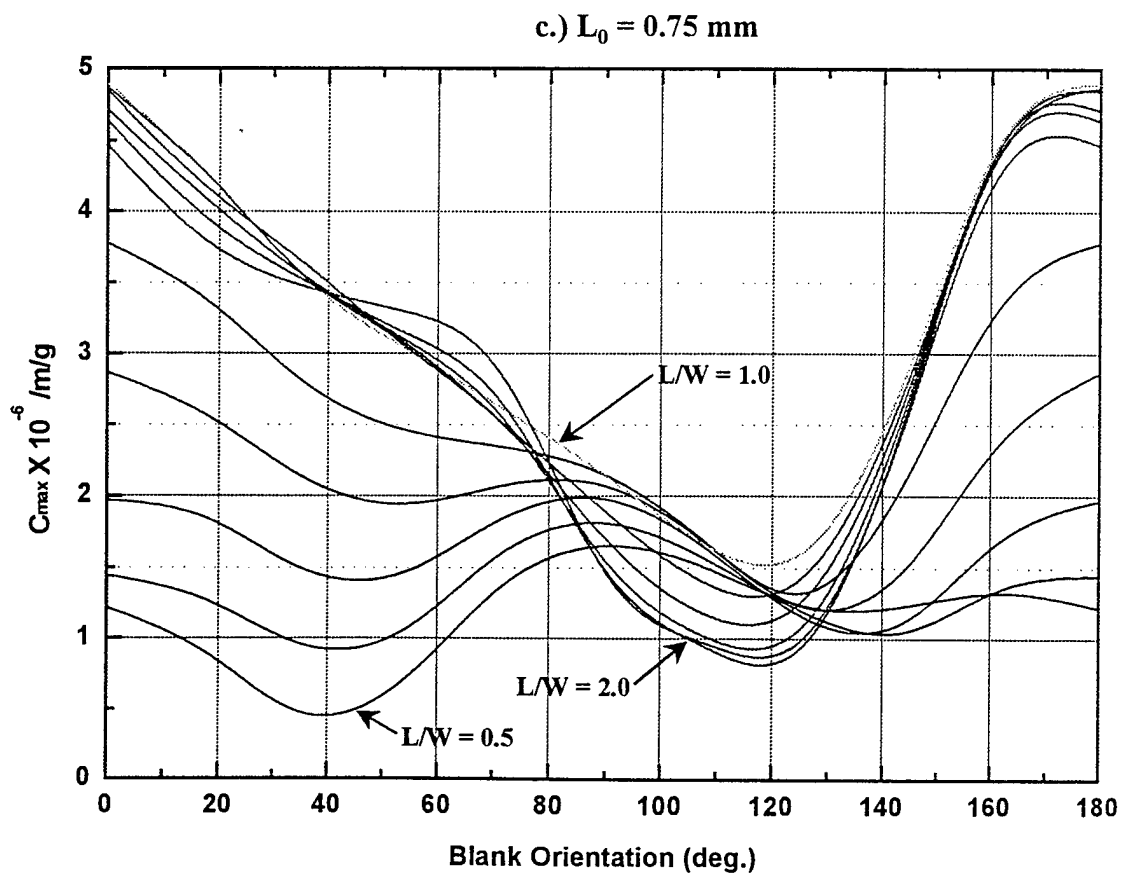
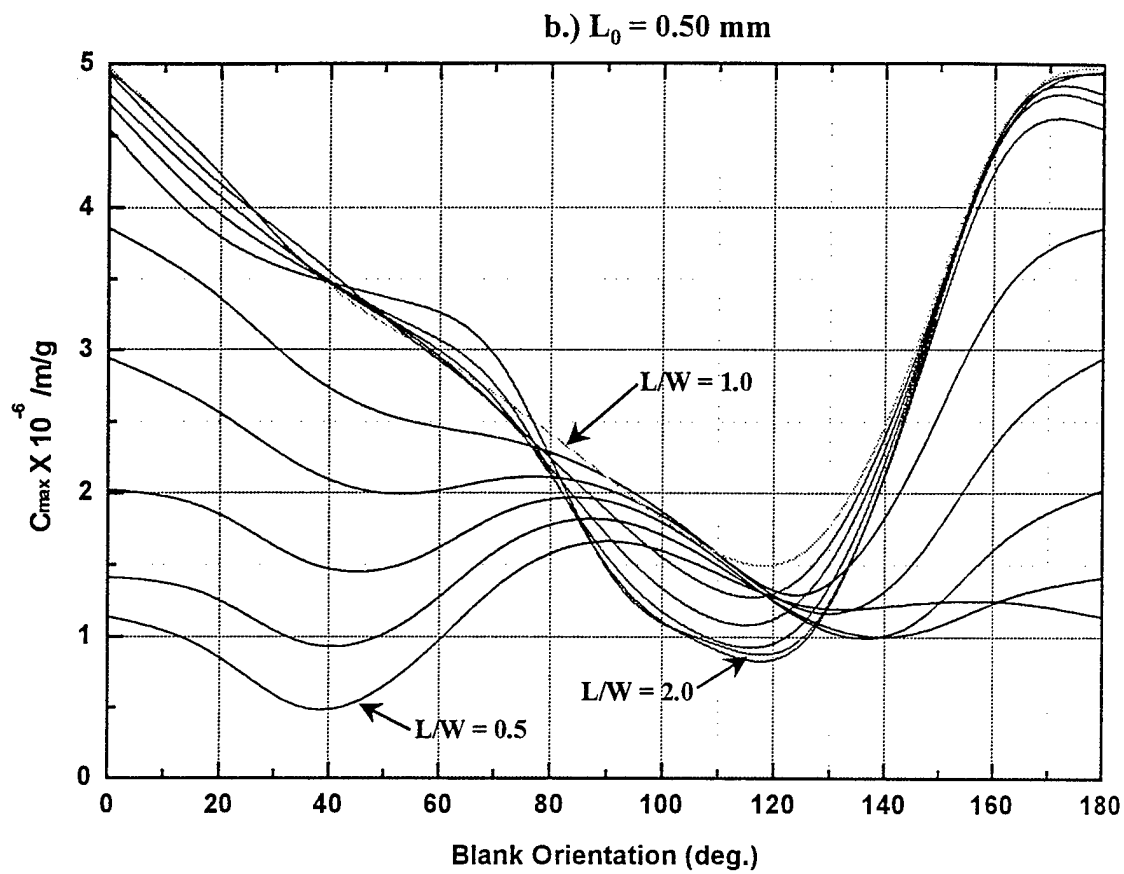


Figure 14.) Mode mispositioning analysis for slotted ribbon mounted rectangular SC Cut plate.

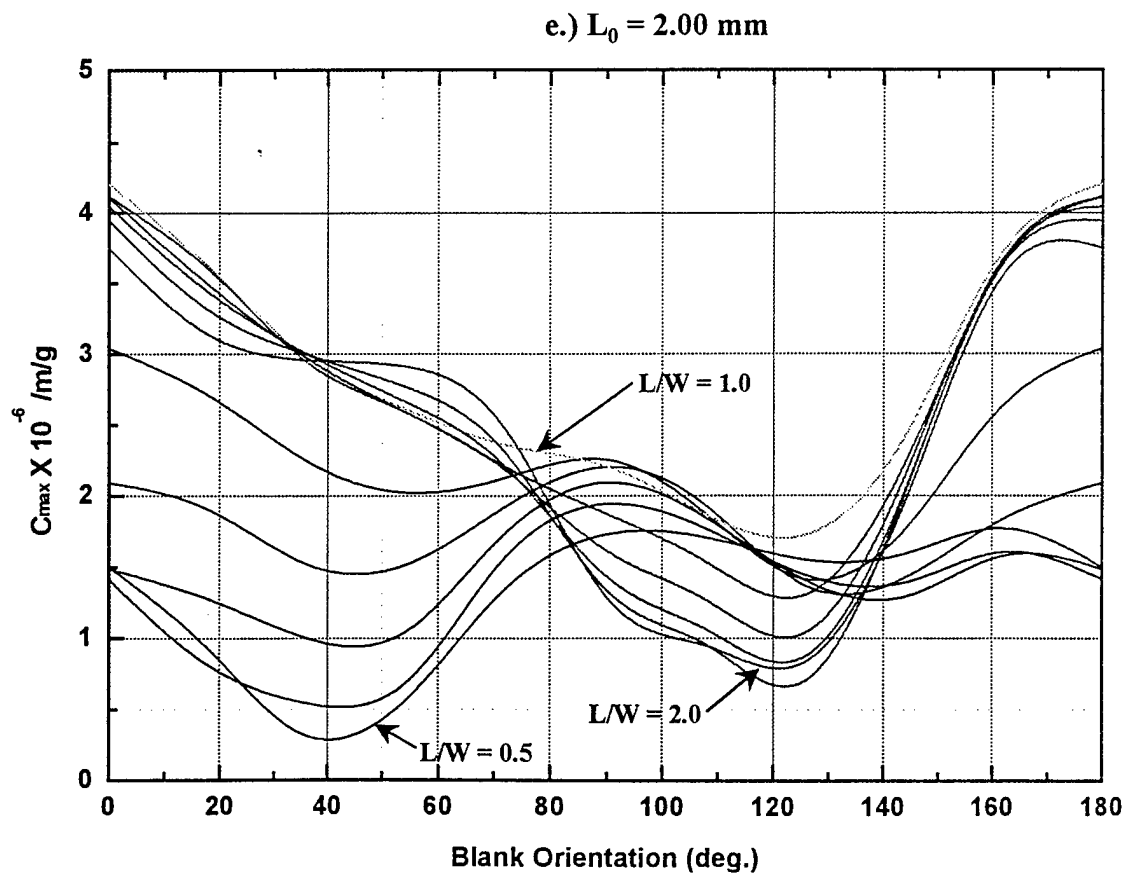
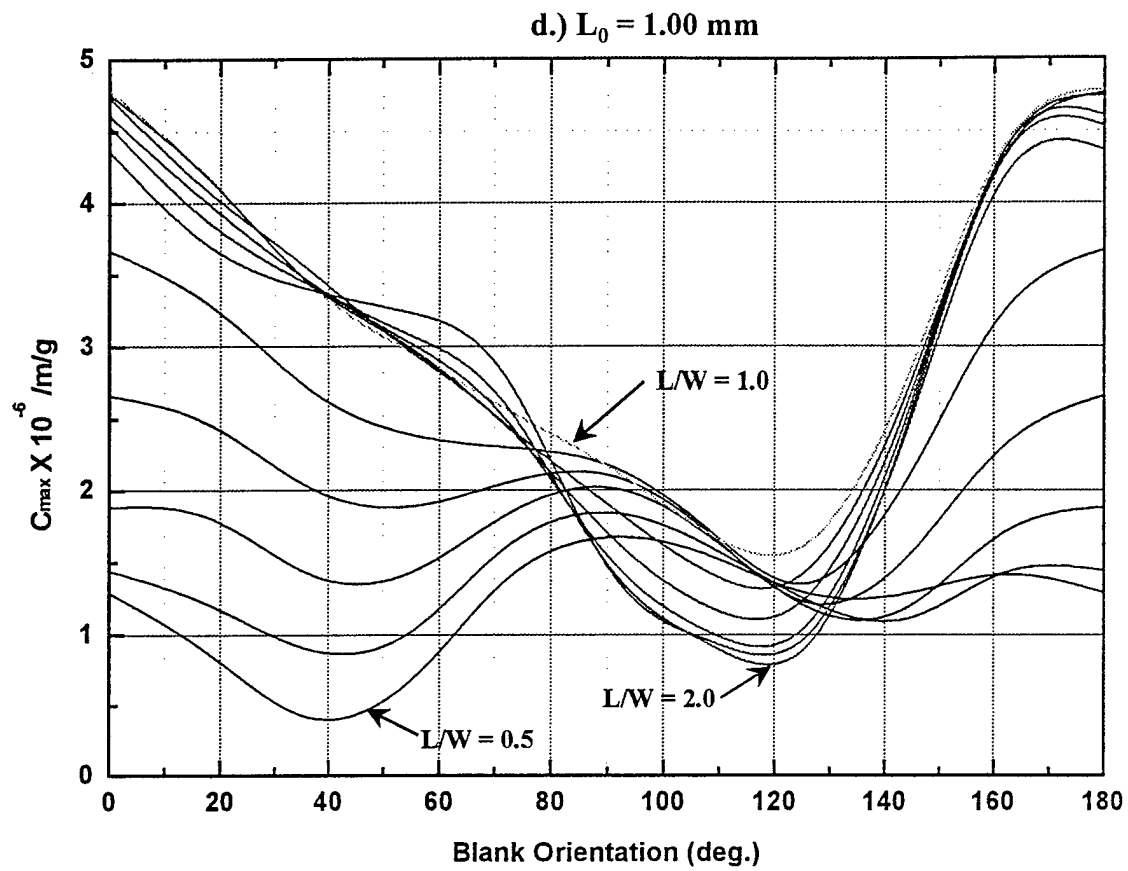
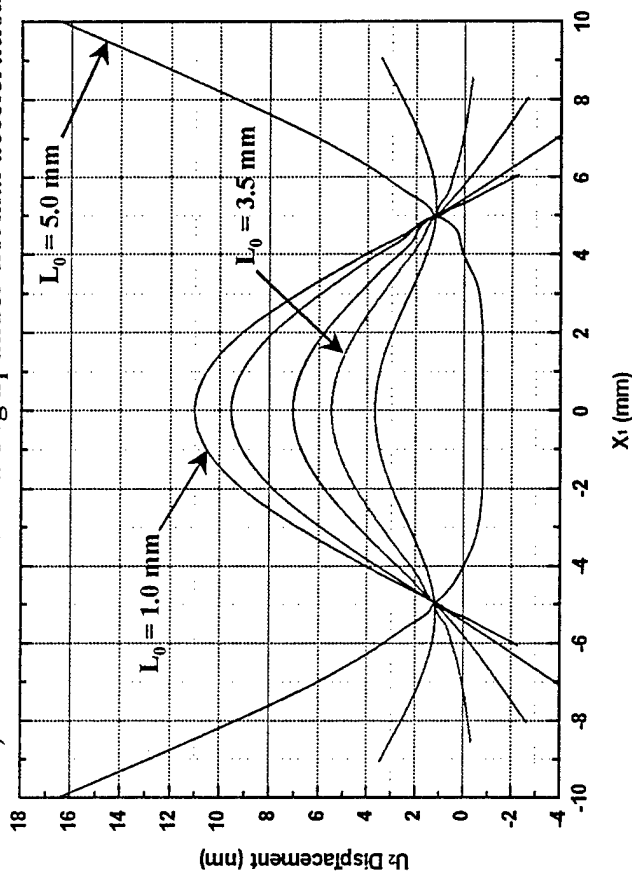


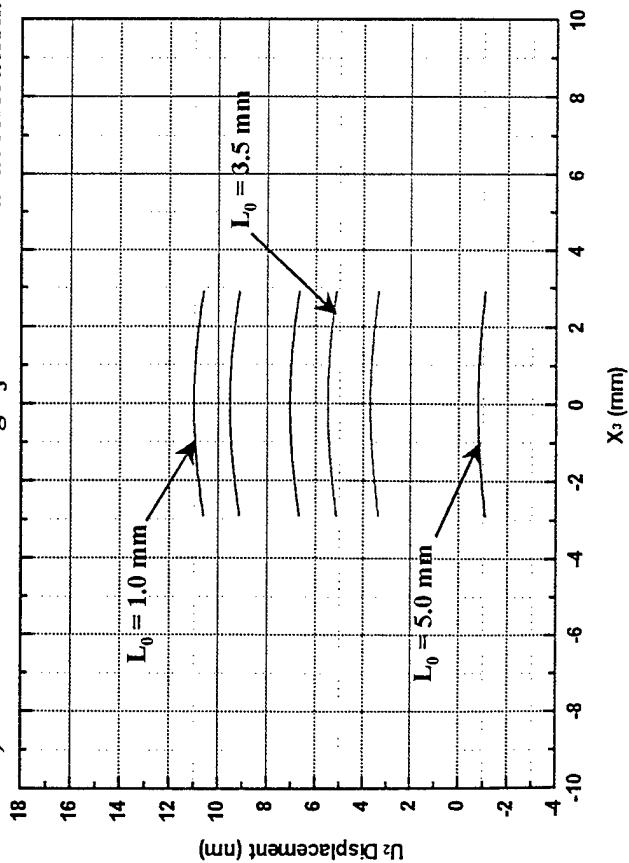
Figure 14.) Mode mispositioning analysis for slotted ribbon mounted rectangular SC Cut plate.



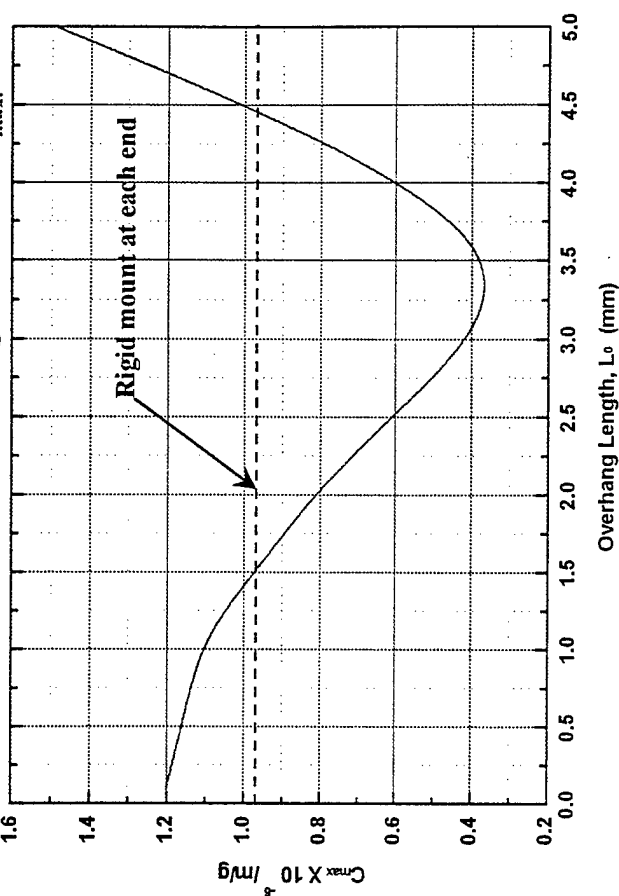
a.) Center deflection along  $x_1$  under normal acceleration.



b.) Center deflection along  $x_3$  under normal acceleration.



c.) Effect of overhang distance on  $C_{max}$ .



$$\phi = 21.93^\circ, \theta = 33.93^\circ$$

$$2a = 4.0 \text{ mm}$$

$$2b = 4.0 \text{ mm}$$

$$2L = 10.0 \text{ mm}$$

$$2w = 5.8 \text{ mm}$$

$$L_R = 0.0508 \text{ mm}$$

$$w_R = w + 0.5 \text{ mm}$$

$$L_0 = \text{varies}$$

$$H_c = 0.254 \text{ mm}$$

$$2h = 0.1644 \text{ mm}$$

$$2h' = 50 \text{ nm Au}$$

$$\gamma = 129.0^\circ$$

$$\text{Plate Thickness} = 2h$$

$$\text{Electrode Thickness} = 2h'$$

$$\text{Ribbon Height} = H_c$$

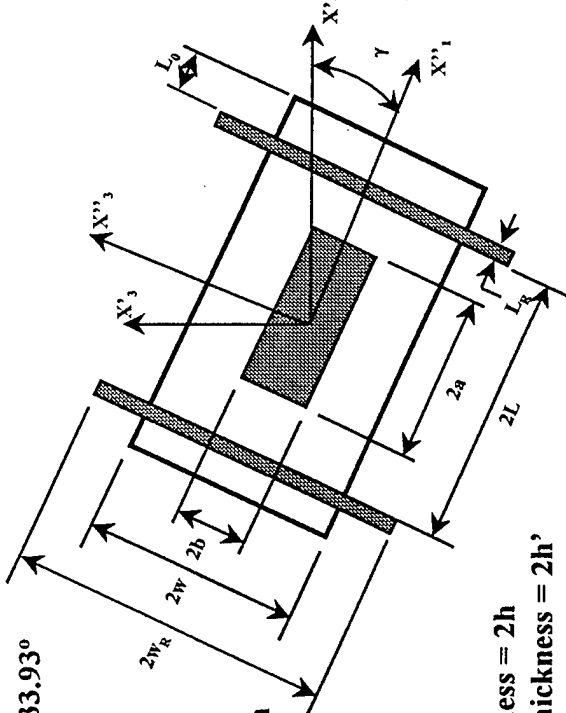


Figure 15.) Effect of overhang distance on the mispositioning coefficient for slotted ribbon mount.

$$\phi = 21.93^\circ, \theta = 33.93^\circ$$

$$2a = 4.0 \text{ mm}$$

$$2b = 4.0 \text{ mm}$$

$$2L_1 = 5.0 \text{ mm} - 10.0 \text{ mm}$$

$$2L_3 = 5.0 \text{ mm} - 10.0 \text{ mm}$$

$$2h = 0.1644 \text{ mm}$$

$$2h' = 50 \text{ nm Au}$$

$$\text{Plate Thickness} = 2h$$

$$\text{Electrode Thickness} = 2h'$$

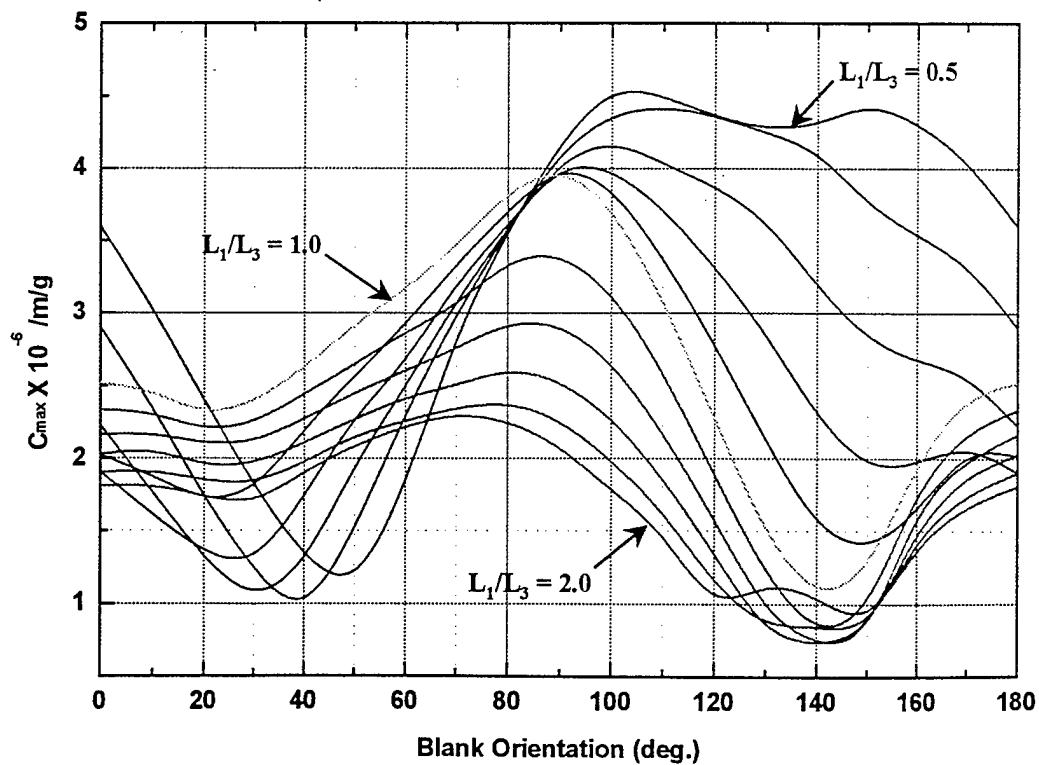
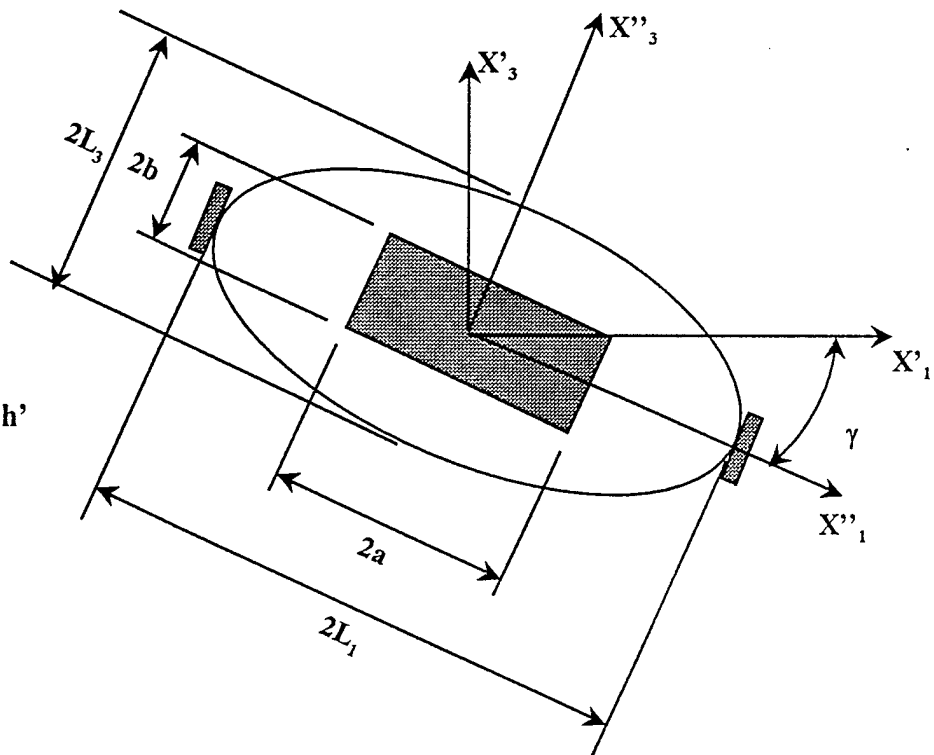


Figure 16.) Mode mispositioning analysis for 2 point mounted elliptical SC Cut Plate.

$\phi = 21.93^\circ$ ,  $\theta = 33.93^\circ$   
 $2a = 4.0 \text{ mm}$   
 $2b = 4.0 \text{ mm}$   
 $2L_1 = 5.0 \text{ mm} - 10.0 \text{ mm}$   
 $2L_3 = 5.0 \text{ mm} - 10.0 \text{ mm}$   
 $2h = 0.1644 \text{ mm}$   
 $2h' = 50 \text{ nm Au}$

Plate Thickness =  $2h$   
 Electrode Thickness =  $2h'$

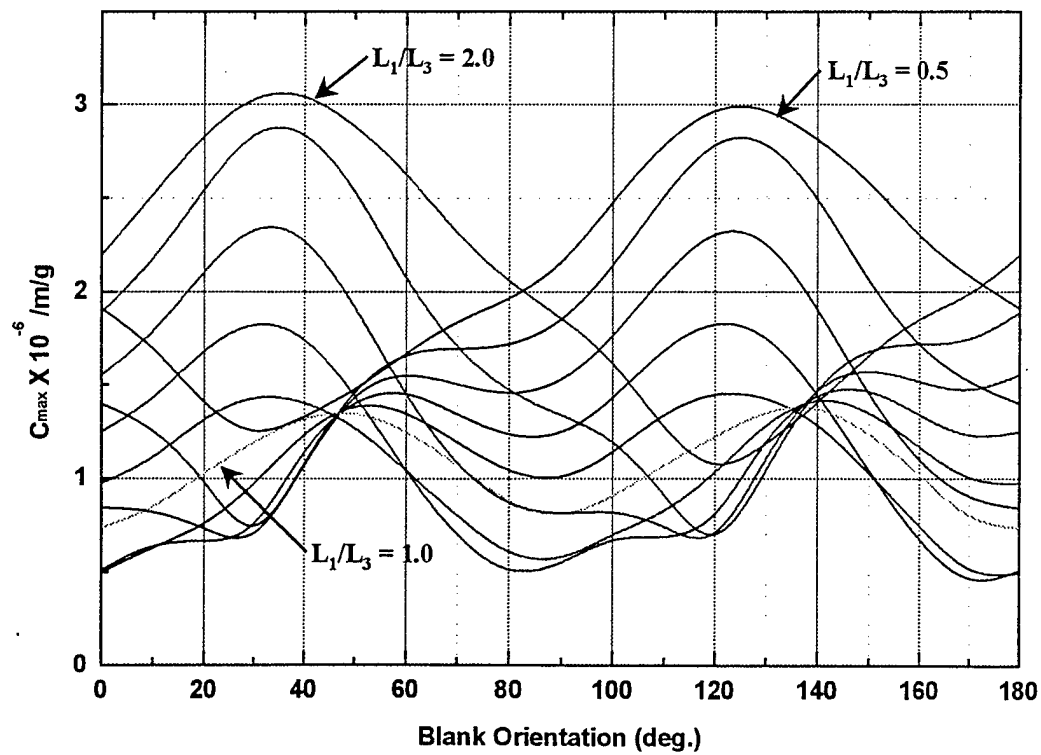
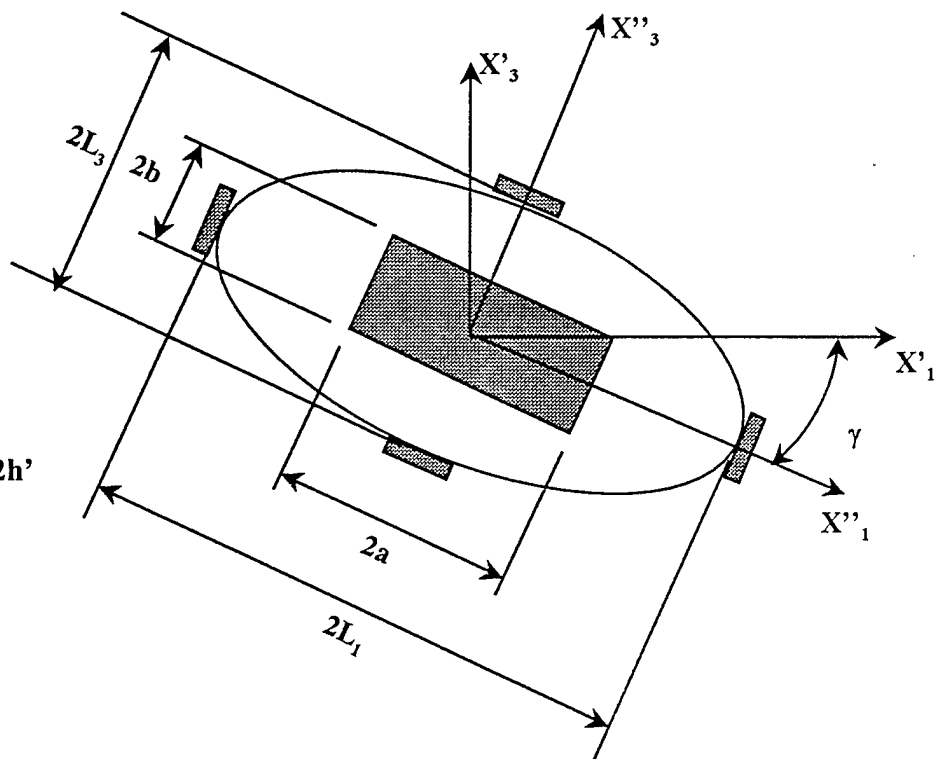


Figure 17.) Mode mispositioning analysis for 4 point mounted elliptical SC Cut plate.

$$\phi = 21.93^\circ, \theta = 33.93^\circ$$

$$2a = 4.0 \text{ mm}$$

$$2b = 4.0 \text{ mm}$$

$$2L_1 = 5.0 \text{ mm} - 10.0 \text{ mm}$$

$$2L_3 = 5.0 \text{ mm} - 10.0 \text{ mm}$$

$$2h = 0.1644 \text{ mm}$$

$$2h' = 50 \text{ nm Au}$$

Plate Thickness =  $2h$

Electrode Thickness =  $2h'$

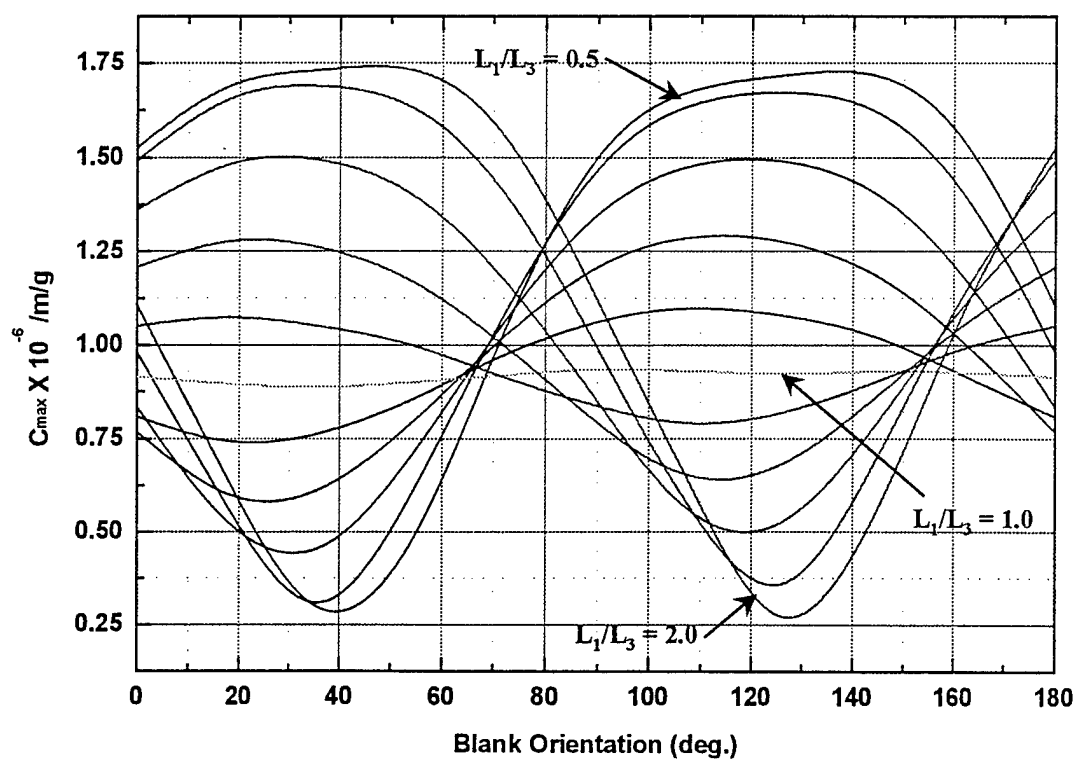
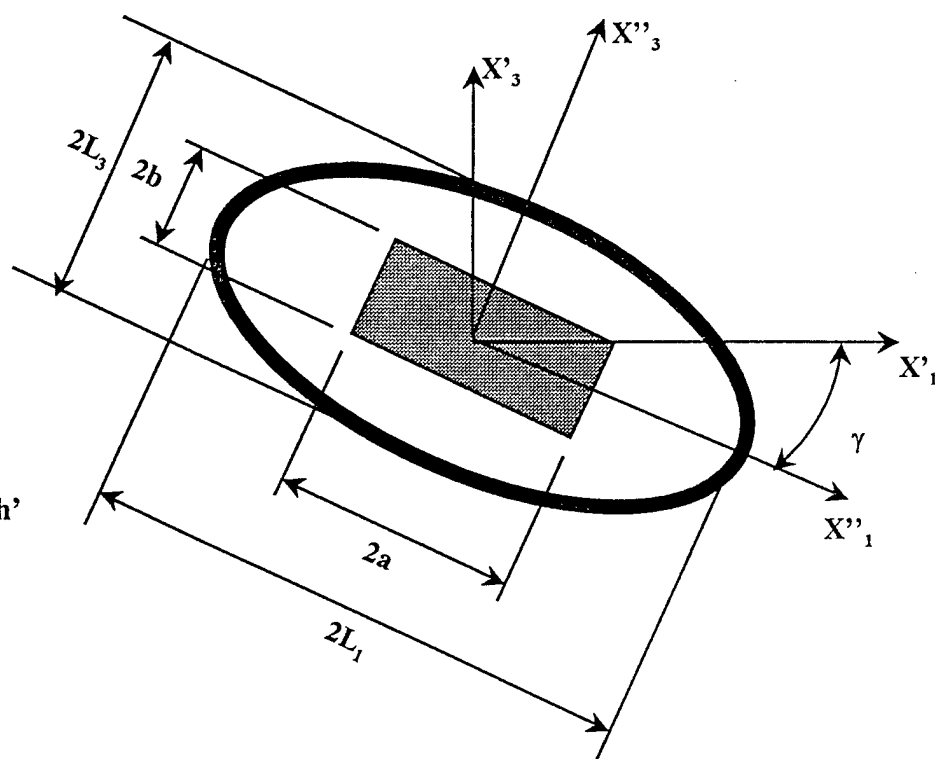
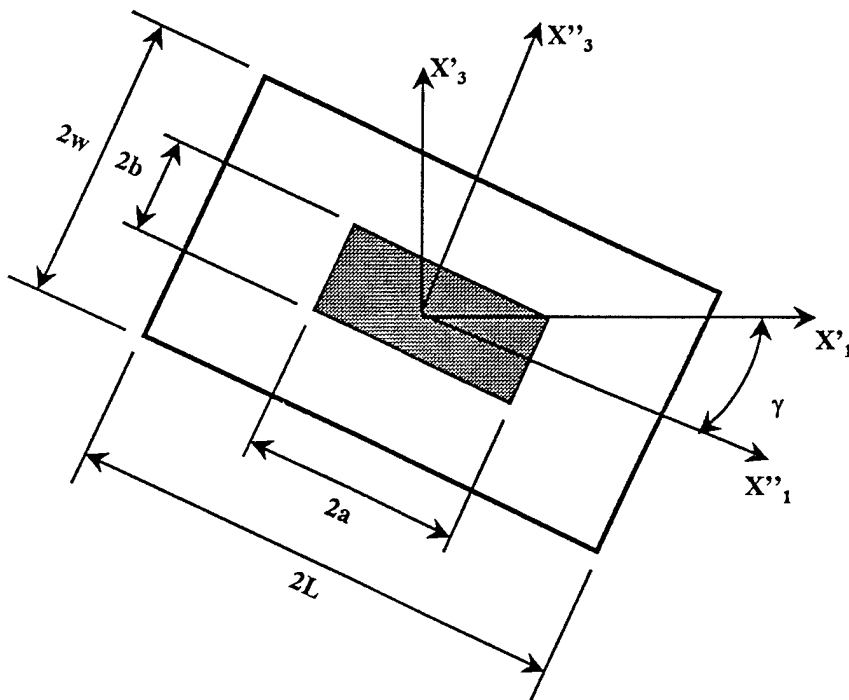


Figure 18.) Mode mispositioning analysis for continuously mounted elliptical SC Cut plate.



$$\begin{aligned}\phi &= 21.93^\circ, \theta = 33.93^\circ \\ 2a &= K \cdot 4.0 \text{ mm} \\ 2b &= K \cdot 4.0 \text{ mm} \\ 2L &= K \cdot 10.0 \text{ mm} \\ 2w &= K \cdot 5.0 \text{ mm} \\ 2h &= K \cdot 0.1644 \text{ mm} \\ 2h' &= 50 \text{ nm Au} \\ \gamma &= 128.0^\circ \\ K &= \text{Geometric Scale Factor}\end{aligned}$$

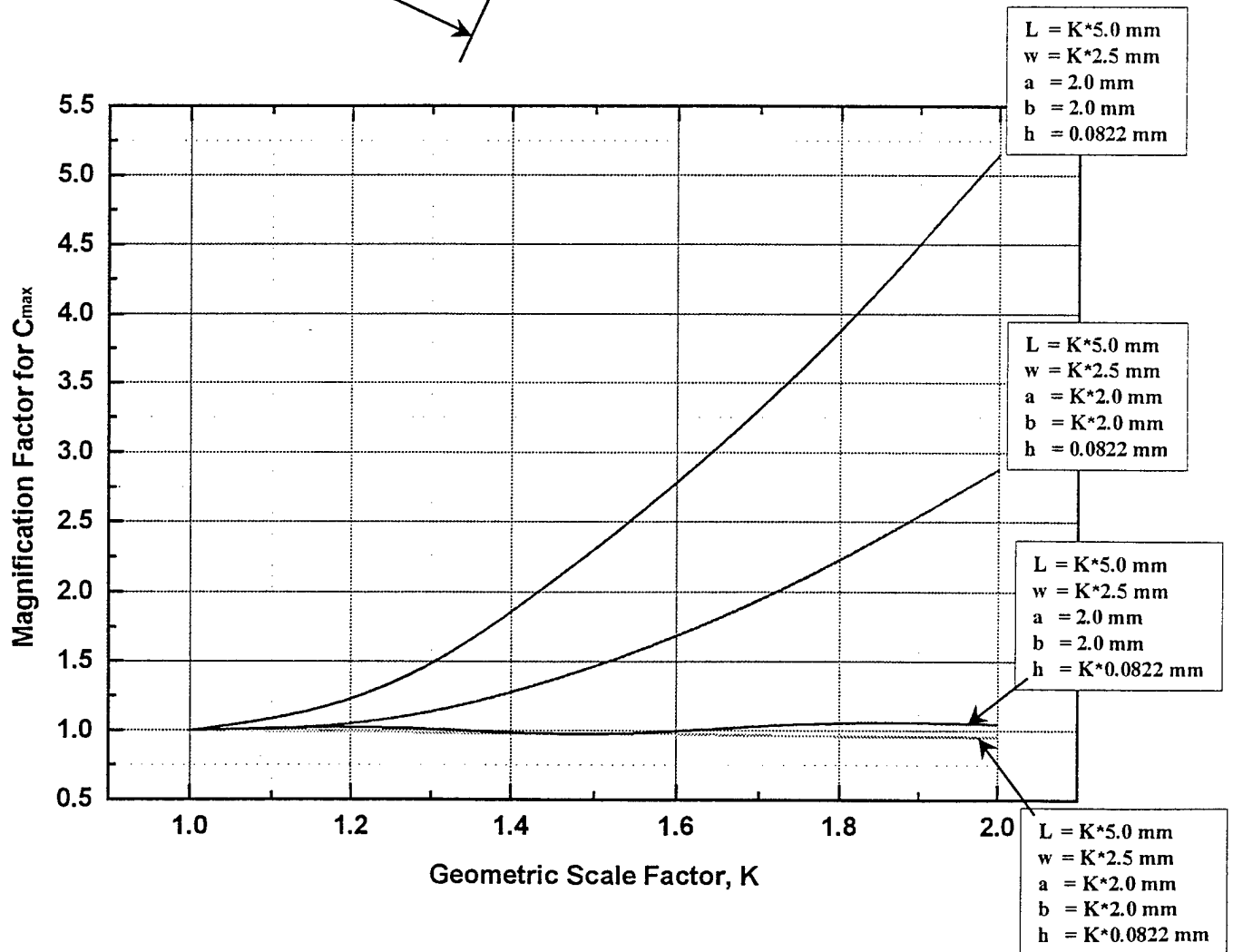
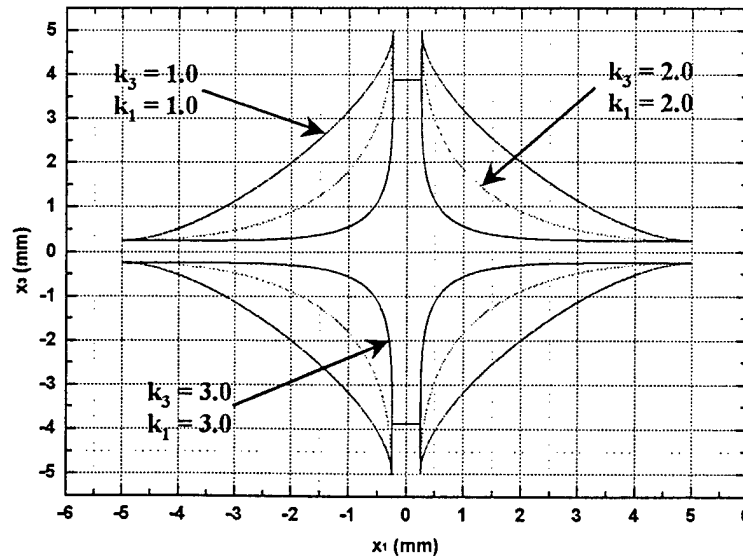
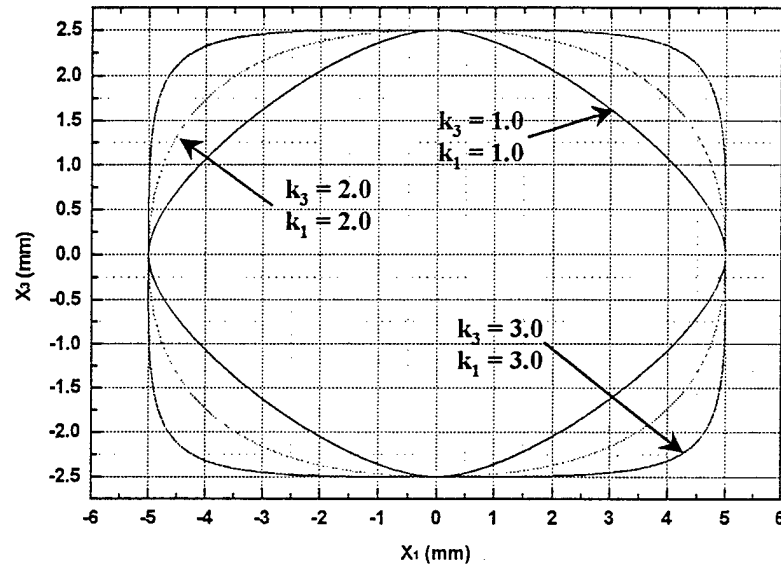
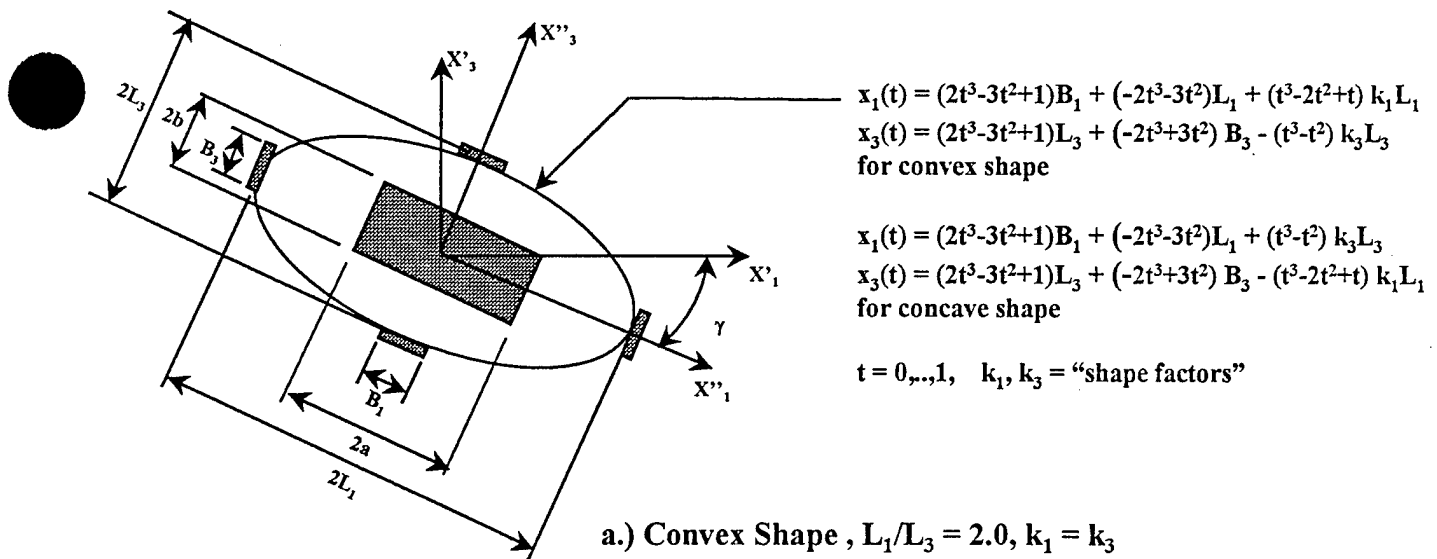


Figure 19.) Effect of geometric scale on the mispositioning coefficient for a rectangular SC Cut plate.



**Figure 20.) Geometry for 4 point mounted plate with cubic shaped boundary used for shape optimization studies.**

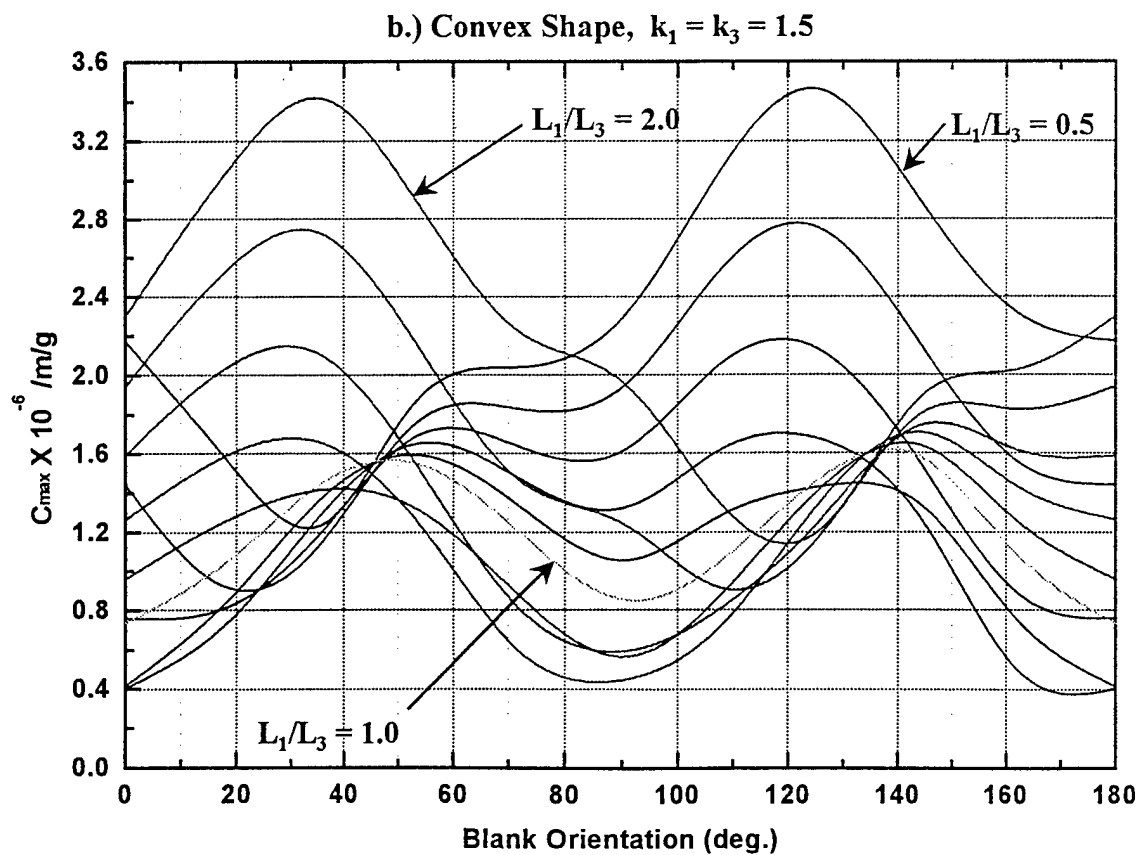
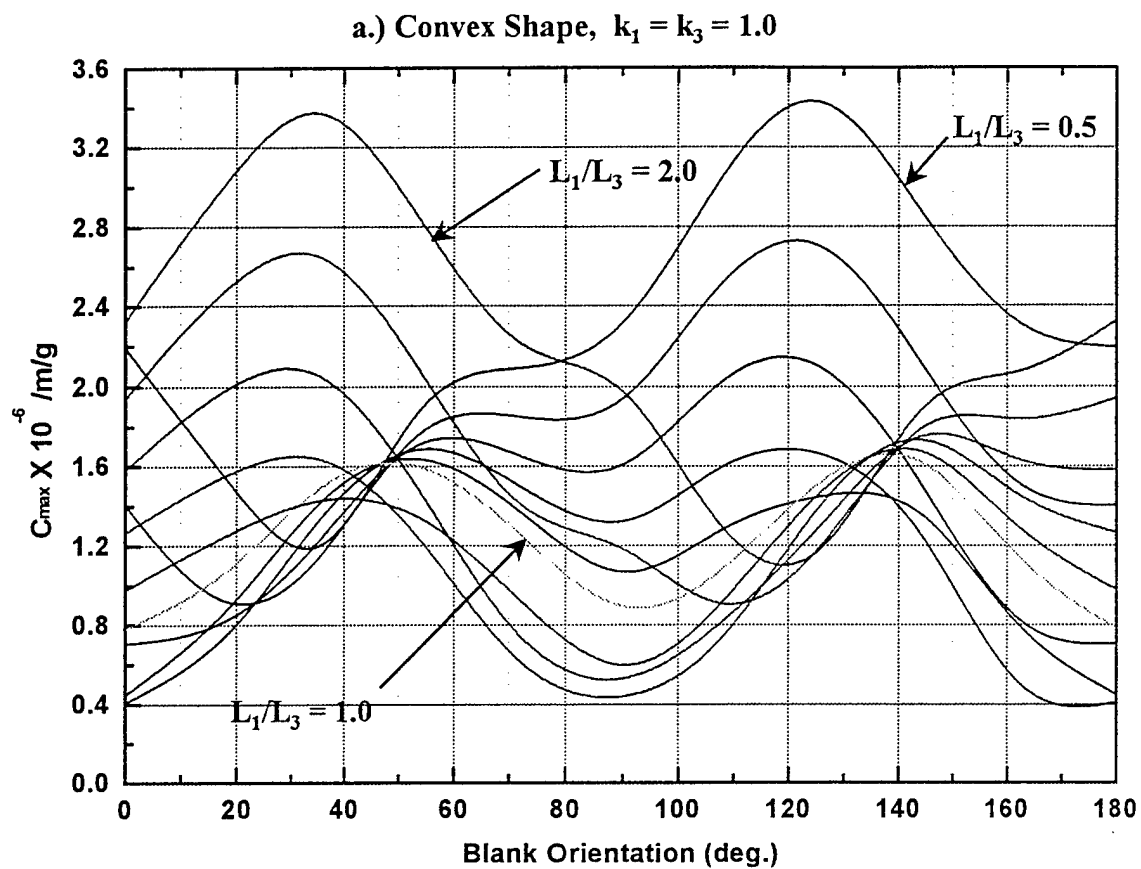
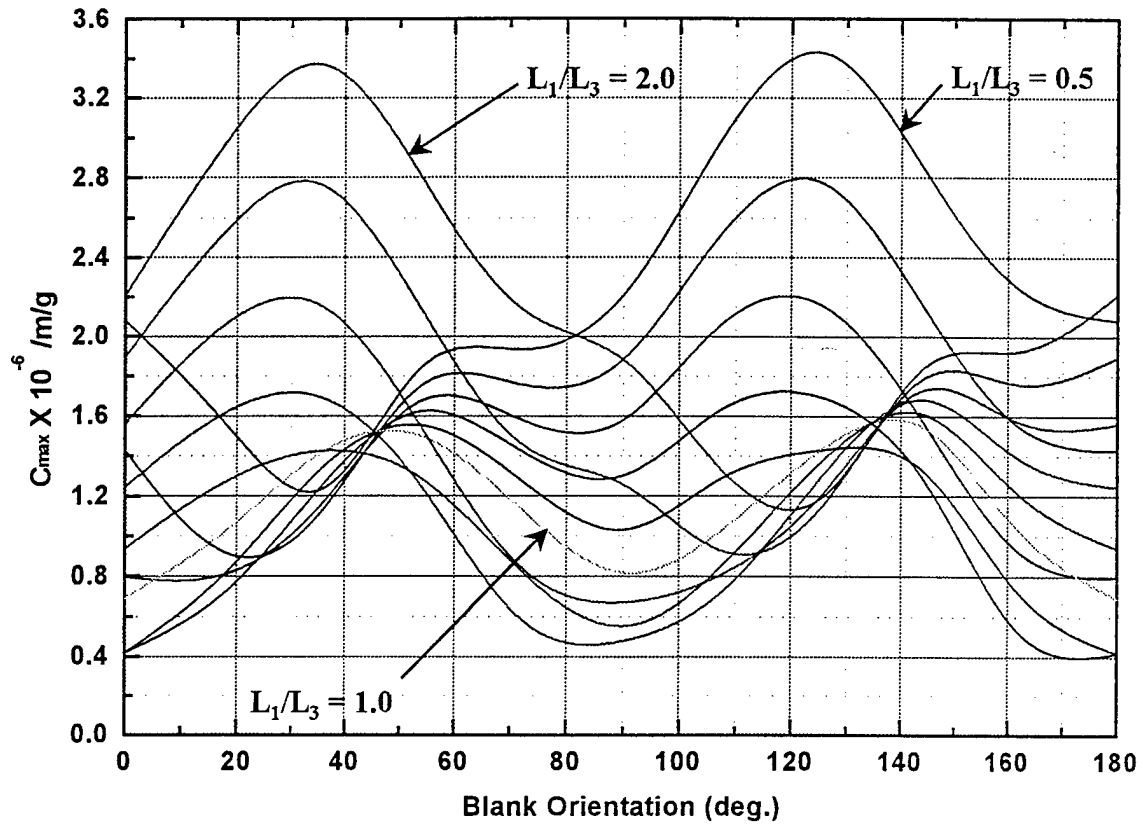


Figure 21.)  $C_{\max}$  vs. blank orientation for convex and concave blank geometries.

c.) Convex Shape,  $k_1 = k_3 = 2.0$



d.) Convex Shape,  $k_1 = k_3 = 2.5$

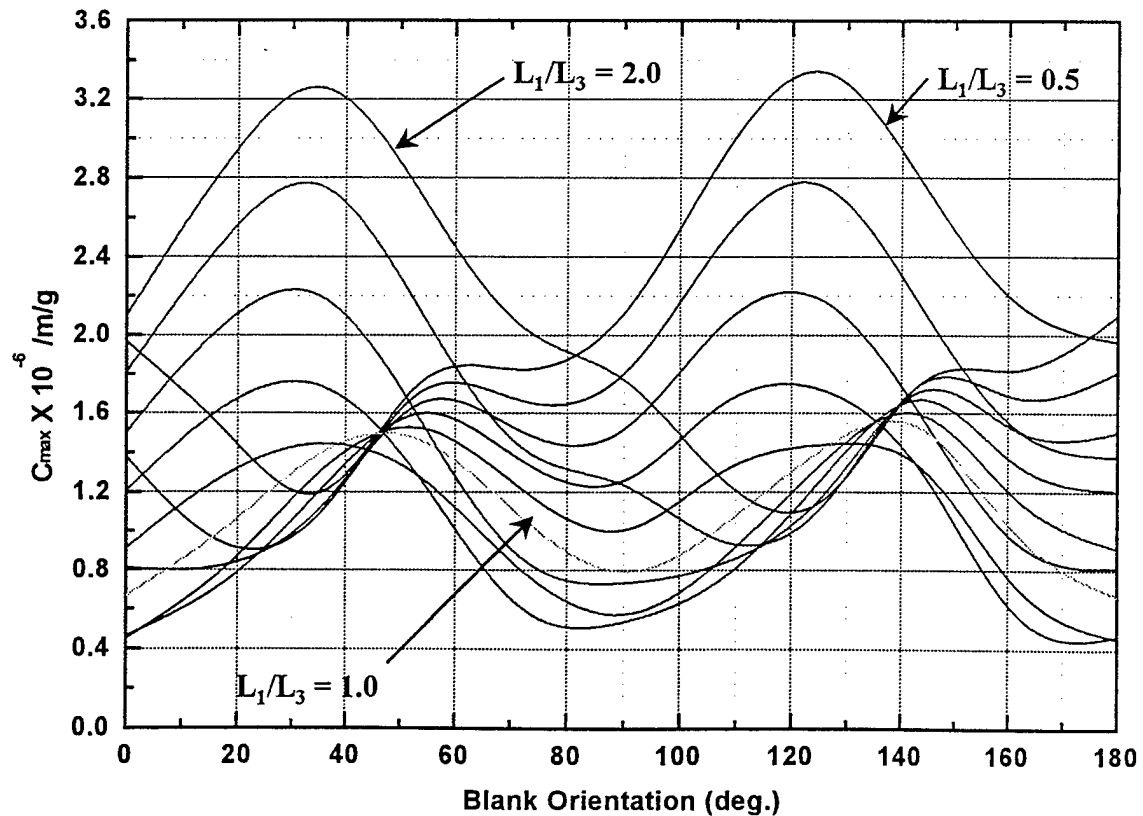


Figure 21.)  $C_{\max}$  vs. blank orientation for convex and concave blank geometries.



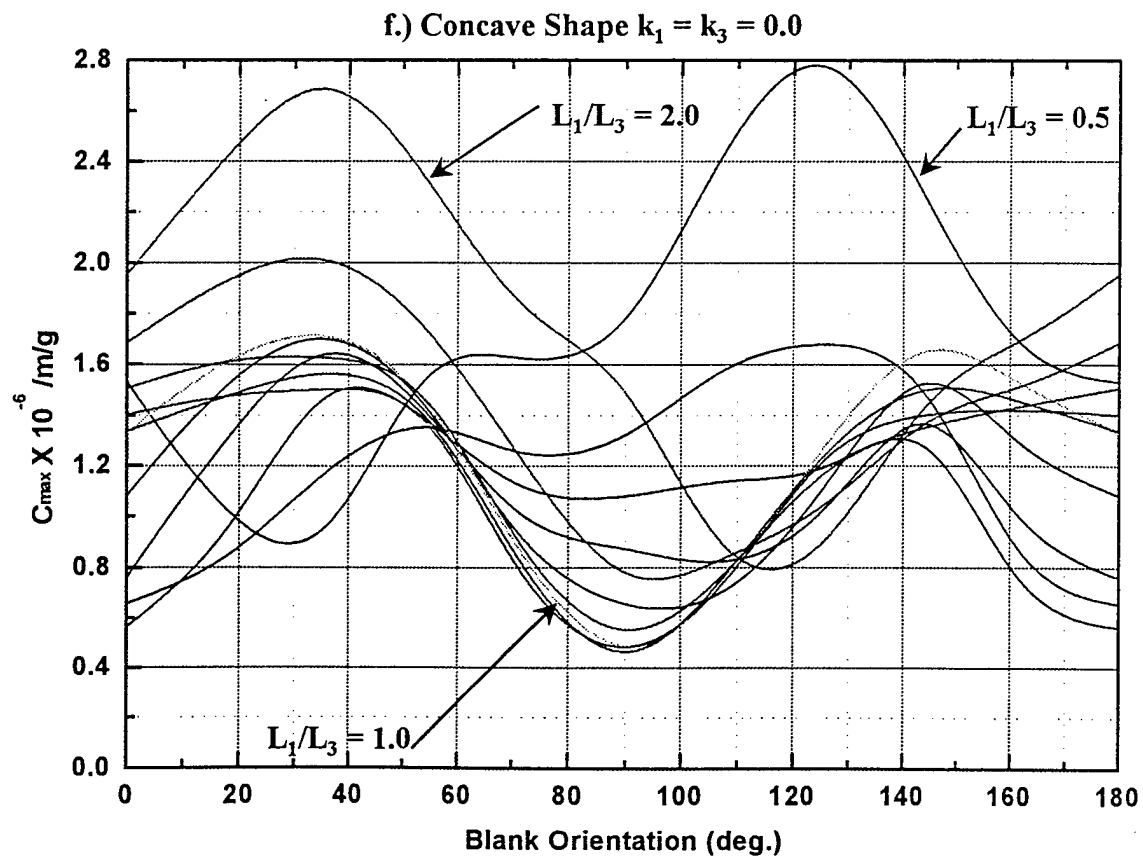
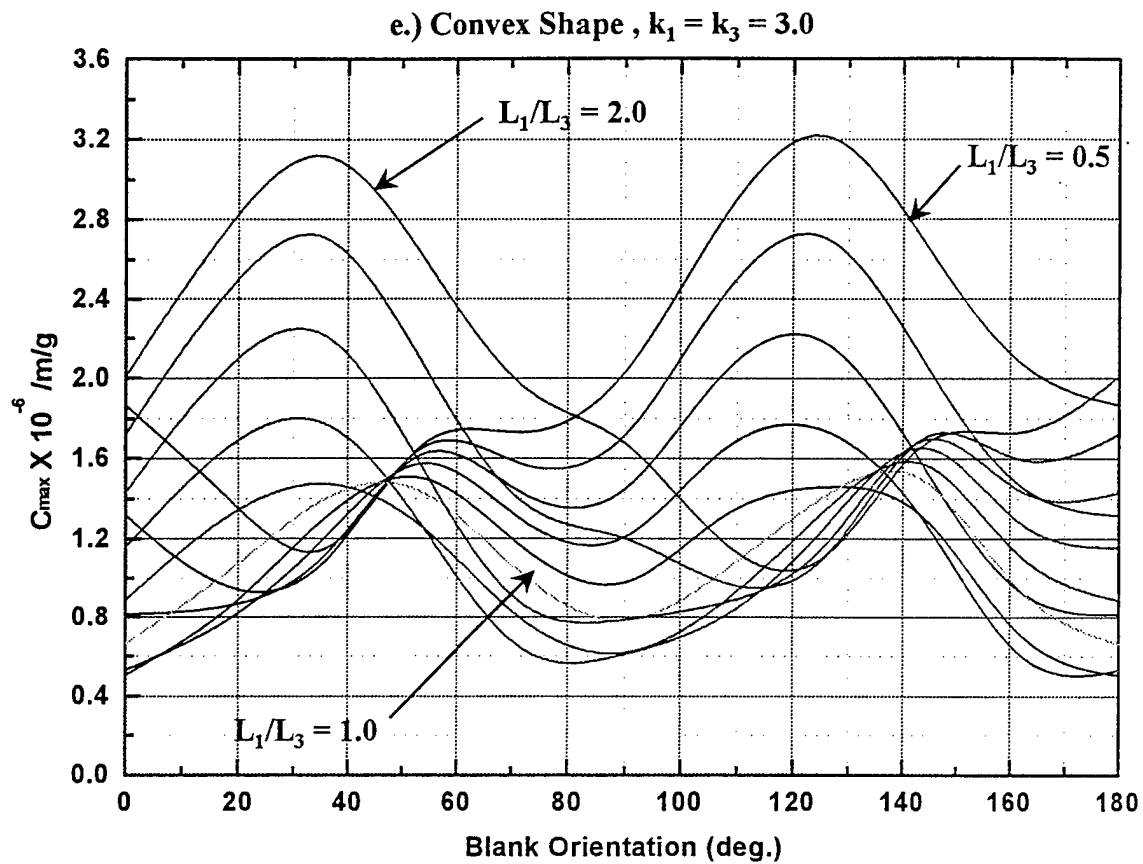
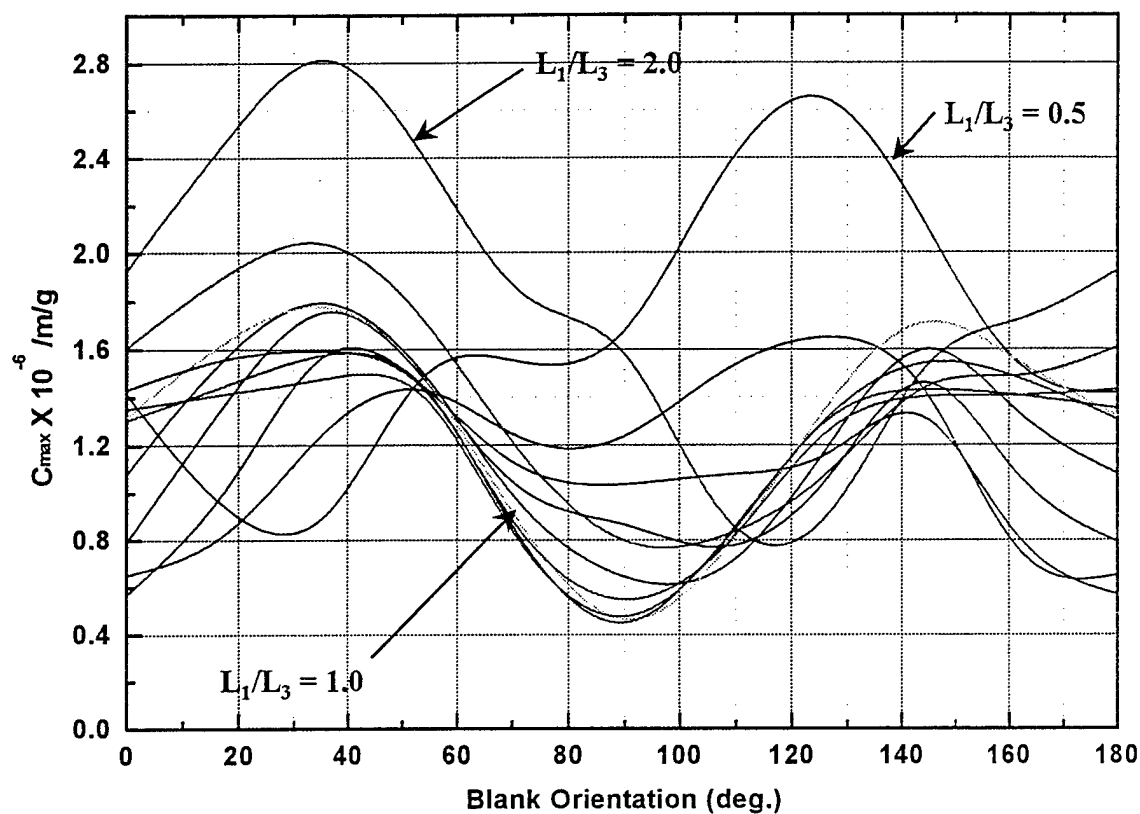


Figure 21.)  $C_{\max}$  vs. blank orientation for convex and concave blank geometries.

g.) Concave Shape,  $k_1 = k_3 = 0.25$



h.) Concave Shape,  $k_1 = k_3 = 0.50$

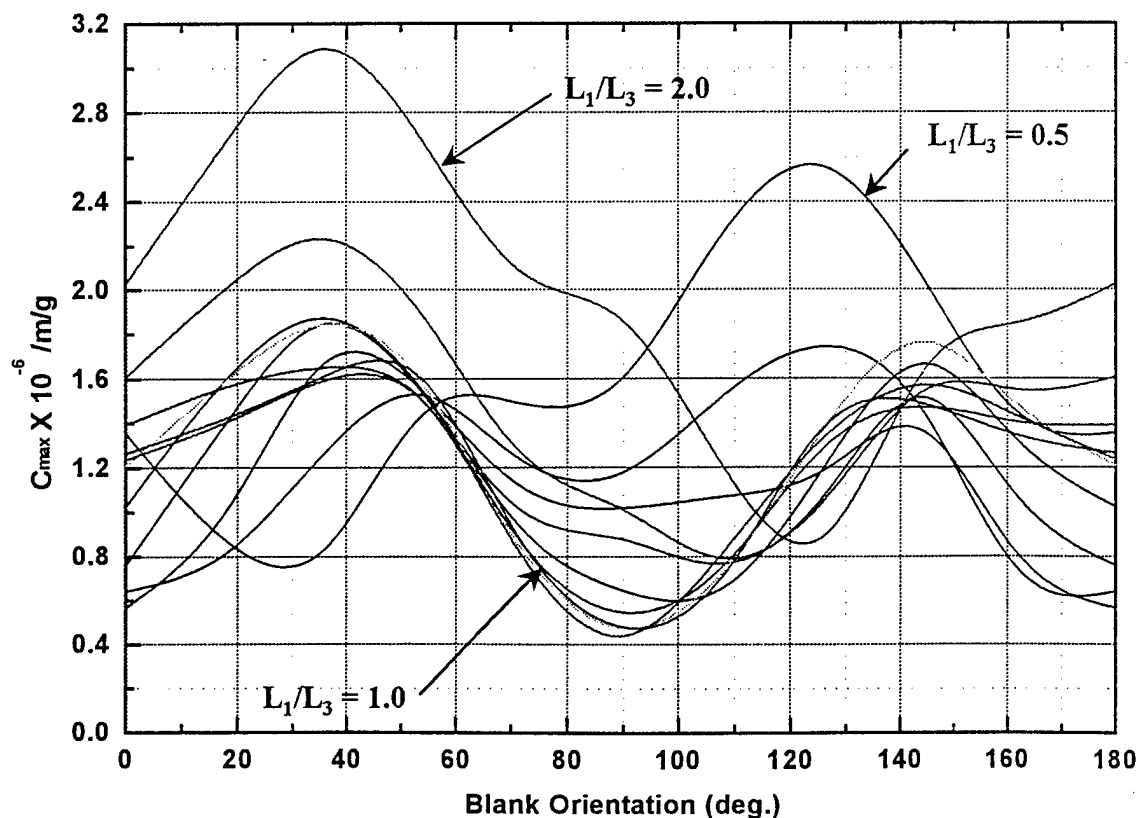


Figure 21.)  $C_{\max}$  vs. blank orientation for convex and concave blank geometries.

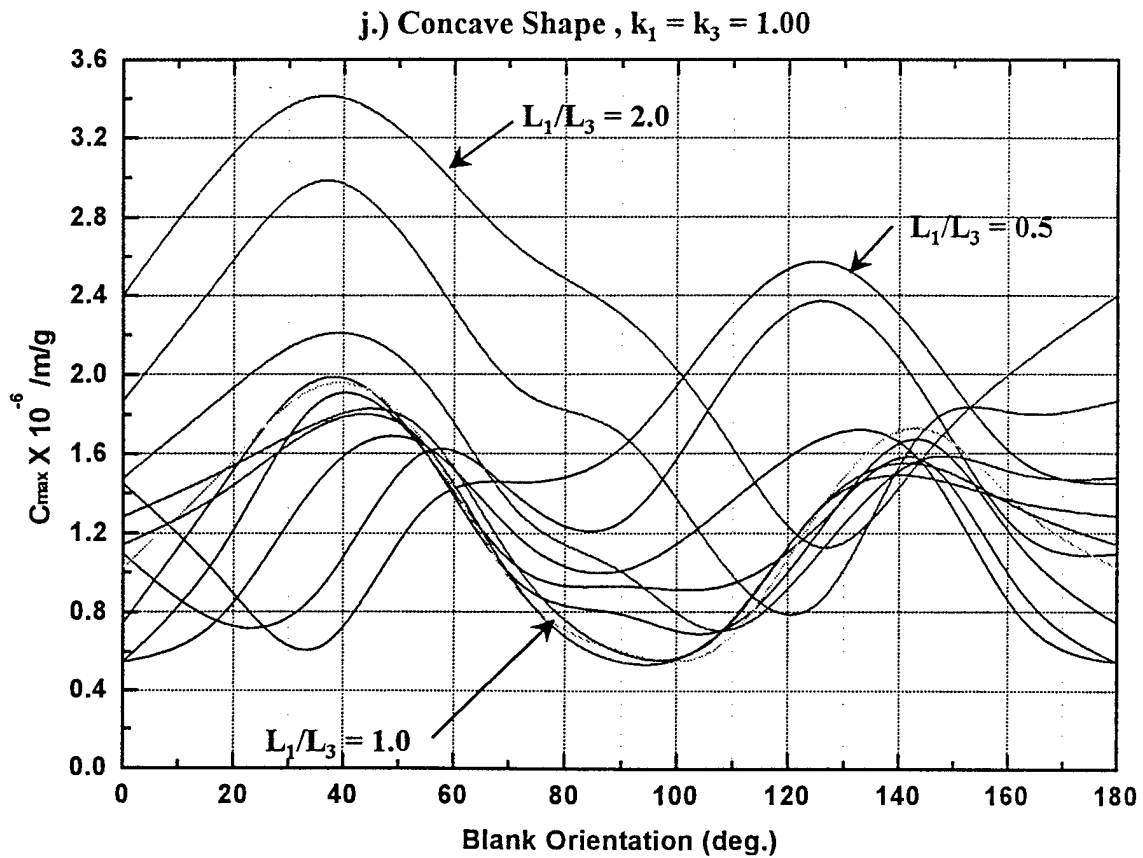
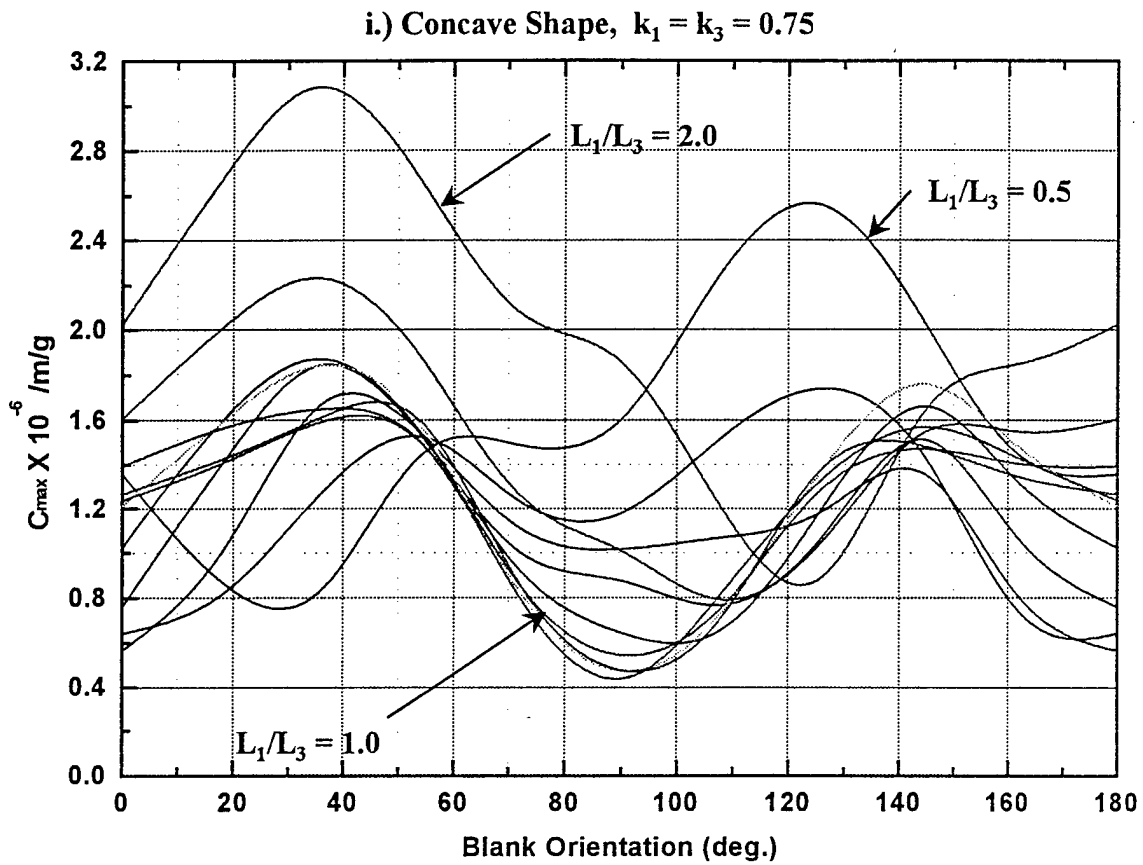


Figure 21.)  $C_{\max}$  vs. blank orientation for convex and concave blank geometries.

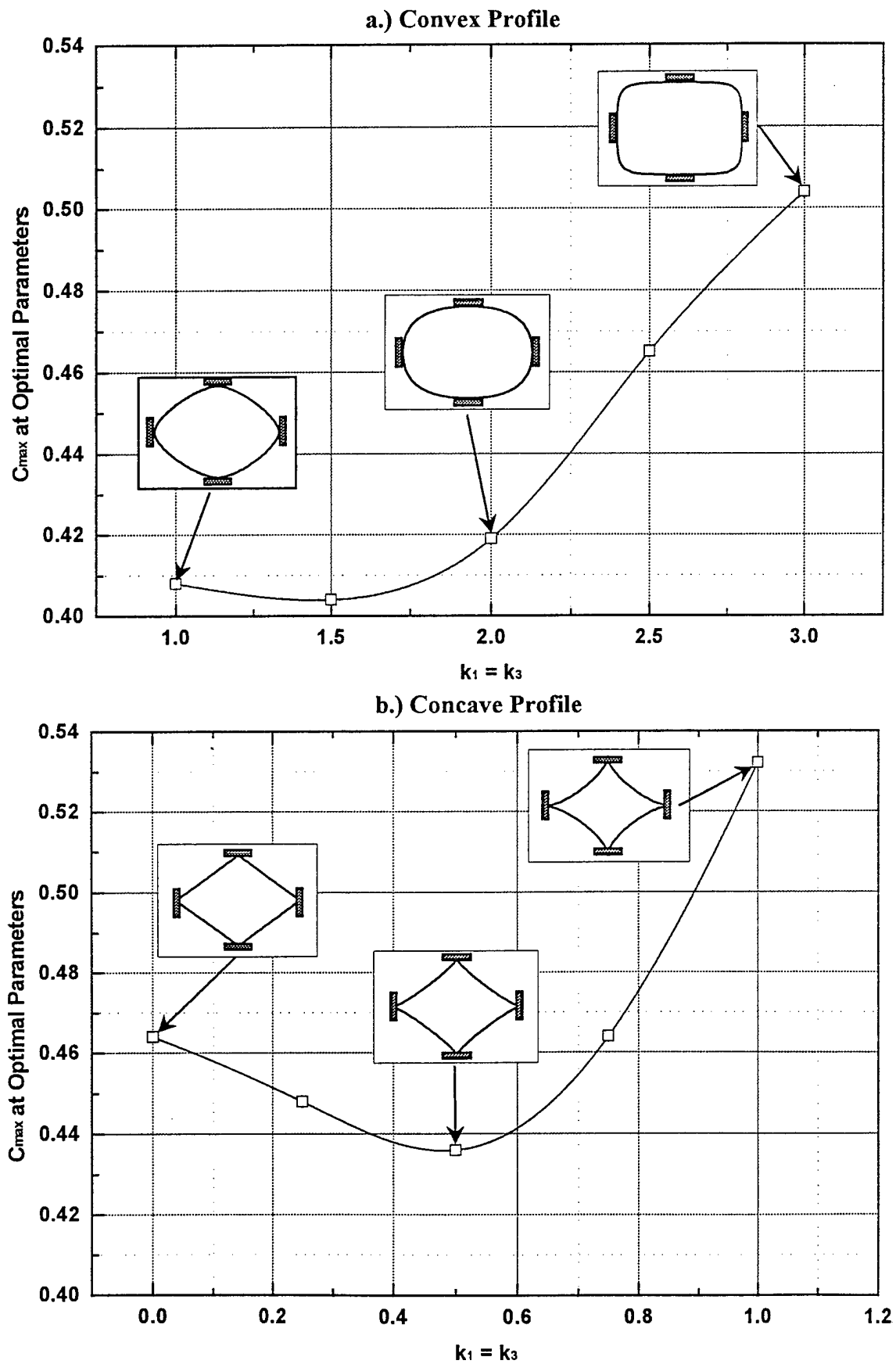


Figure 22.) Minimum  $C_{\max}$  vs. shape factor for convex and concave blank geometries.

Geometry and Crystal Cut	$L_1, L_3$ (mm)	Blank Orientation (deg.)	$C_{\max}$ at Optimal Point ( $\times 10^{-6}$ )	Other Parameters
Rectangular SC Cut	$L_1 = 4.176$ $L_3 = 2.500$	128.0	0.249	
Rectangular AT Cut	$L_1 = 2.500$ $L_3 = 3.172$	0.0	0.502	
Rectangular FC Cut	$L_1 = 2.500$ $L_3 = 4.352$	33.0	0.341	
Rectangular $\phi = 10.0$ $\theta = 33.93$	$L_1 = 2.500$ $L_3 = 3.440$	23.0	0.388	
Rectangular $\phi = 20.0$ $\theta = 33.93$	$L_1 = 2.500$ $L_3 = 3.730$	37.0	0.264	
Rectangular $\phi = 25.0$ $\theta = 33.93$	$L_1 = 2.500$ $L_3 = 5.000$	43.0	0.228	

Geometry and Crystal Cut	$L_1, L_3$ (mm)	Blank Orientation (deg.)	$C_{\max}$ at Optimal Point ( $\times 10^{-6}$ )	Other Parameters
Ellipse, 2 point mount SC Cut	$L_1 = 4.176$ $L_3 = 2.500$	141.0	0.743	
Ellipse, 4 point mount SC Cut	$L_1 = 2.500$ $L_3 = 3.172$	0.0	0.500	
Ellipse, fixed SC Cut	$L_1 = 2.500$ $L_3 = 4.352$	128.00	0.246	
Rectangular, slotted ribbon mount SC Cut	$L_1 = 5.000$ $L_3 = 2.900$	129.0	0.382	$L_0 = 3.5$ mm
Shape blank SC Cut	$L_1 = 2.500$ $L_3 = 5.000$	0.0	0.40	$k_1 = 1.0-1.5$ $k_3 = 1.0-1.5$ (convex)

Figure 23.) Summary of results from non-linear optimization study.

## Part 2: Report on The Theoretical and Experimental Results for Optimization of the Acceleration Sensitivity of Rectangular Crystal Resonators

### Introduction

Theoretical and experimental results for the acceleration sensitivity of rectangular AT and SC Cut crystal resonators are presented. In a previous paper [1], a detailed theoretical analysis was presented on the g-sensitivity of crystal resonators with non-circular geometry. This work was also described in detail in the interim report [2], which is also presented in more detail as the first part of this report.

The present study focuses on the realization of various designs taken from the first analysis. Rectangular AT Cut crystal resonators have been fabricated and mounted in a rigid two-ended configuration and a two-ended with overhang configuration. The effect of support spacing on the g-sensitivity for these crystals is discussed and the results are compared with conventional rigid mounting (no overhang). Rectangular SC Cut crystals have also been fabricated and the effect of blank orientation on the g-sensitivity for these crystals is presented. A brief discussion of the g-sensitivity measurement technique is also presented.

Manufacturing precision crystal resonators with low acceleration sensitivity continues to be a major challenge in the production of ultra stable frequency sources for many applications, such as GPS. The fundamental problem faced in producing real resonators is that the acceleration sensitivity can be very sensitive to manufacturing tolerances for a particular design. Misplacement of the electrode plating, misalignment of the crystal blank in the supports, and inaccuracies in the amount and distribution of adhesive all lead to appreciable degradation in the g-sensitivity of manufactured resonators. In a previous paper [1], theoretical results were presented for the analysis of the acceleration sensitivity of singly and doubly rotated crystal resonators with non-circular geometry. The results of this study showed that a substantial improvement could be obtained by using crystal blanks with rectangular geometry, and more recent results have shown that there are definite optimal blank dimensions for particular mounting schemes. In general, it has been found that the major effects are the planar aspect ratio and orientation of the plate. The analytical studies have also revealed that blank size reduction at a given frequency and the use of interior supports which result in "overhangs" on the mounted crystal may also play a role in improving the g-sensitivity of crystal resonators. Based on the developed design criteria, AT and SC cut rectangular resonators have been fabricated using a variety of mounting strategies and blank orientations. Experimental results for these crystals are presented along with the corresponding theoretical predictions.

### Measurement Technique

The setup shown in figure (1) is used for measurement of discrete resonators. The method is a variant of the technique reported by Filler [3] and others, in which a crystal oscillator is mechanically mounted on a vibration table, and a low frequency sinusoidal vibration field is applied. The effect is simple frequency modulation with a very low modulation index, and the relationship between the sideband levels and the g-sensitivity is shown to be:

$$\gamma = \frac{2\omega_v}{a\omega_0} 10^{L/20}$$

where  $L$  is the sideband level in dBc,  $\gamma$  is the g-sensitivity,  $a$  is the g level,  $\omega_v$  is the vibration frequency, and  $\omega_0$  is the oscillator frequency.

In the case of discrete crystal measurement, the crystal is physically mounted on the vibration table with a thin coaxial cable connecting it to a 180° hybrid transformer. On the balancing port of the hybrid a matched cable length with capacitive trimmer is used to cancel out the  $C_0$  of the resonator and the connecting cable. This is a convenient network as it gives a frequency response which is symmetrical about the series resonance. This is a passive network, and the signal source is an external synthesizer (in our case we used an HP3335) set to the crystal's series resonance. The relationship between the sideband levels and the g-sensitivity is now defined by the equation:

$$\gamma = \frac{\sqrt{4\omega_v^2 + \omega_3^2}}{\omega_0 a} 10^{L/20}$$

where  $\omega_3$  is the 3 dB bandwidth of the crystal response.

For a vibration environment for this test, a frequency of 70 Hz has been found to be convenient, with a level of 10g peak acceleration. This avoids interaction with 60 Hz or 50 Hz mains frequencies and gives a workable displacement level. Lower frequencies can be used to good effect to increase the vibration induced sideband levels, but this can result in rather high mechanical displacements. A fixture has been made to enable the devices to be conveniently measured in three mutually orthogonal axes.

The HP4396 Network / Spectrum Analyzer is particularly well suited to this measurement as it is one of a genera of instruments which performs its IF filtering by an FFT technique. This enables it to operate with relatively short sweep times even with resolution bandwidths as low as 1 Hz. The measurement sequence is set up in the instrument's internal programming language, and starts with the analyzer in 'Network' mode and the synthesizer switched off. Successive sweeps are used to determine the center frequency and bandwidth of the resonator. Then the instrument is switched to 'Spectrum' mode, and the synthesizer is set to the center frequency of the response. For a 70 Hz vibration frequency, a span of 300 Hz is set up on the spectrum analyzer, centered on the synthesizer frequency, with a resolution bandwidth of 1 Hz. The instrument markers are used to determine the sideband levels relative to the carrier, and this information is used to calculate the g-sensitivity directly.

For some devices, motional parameters were also characterized using a Transat CNA test station. This system uses a pi-network as a measurement port and performs impedance measurements in a pre-defined sequence around the crystal resonance. These data are manipulated using the method described in the IEC444-5 measurement standard to derive the  $C_0$ ,  $C_1$ ,  $R_1$  and  $Q$  of each resonator.

## Discussion of Results

The first study consists of a rectangular AT Cut resonator mounted into a Vectron S-Type ceramic package, as shown in figure (2). This package has shelves at two opposite ends, which allow for double-ended mounting. These crystals were fabricated with a rectangular electrode that is centered with respect to the crystal blank and mount. These crystals were directly mounted to the ceramic with manually dispensed conductive epoxy adhesive. Shown in figure (3) are the results of an experiment performed on this configuration for different blank frequencies. In this experiment a single ended, or cantilever, mount was used. As expected, the

component of  $\Gamma$  normal to the crystal plate dominates the g-sensitivity of these devices with a nominal value of about  $3 \times 10^{-9}/g$ . Interesting to note from this plot is how the spread in the data tends to increase (particularly above 30 MHz), while the average value remains relatively constant at  $3 \times 10^{-9}/g$ . As the frequency increases, the plate thickness decreases, and it appears that the sensitivity of  $\Gamma$  to manufacturing imperfections likewise increases. The likely source of manufacturing imperfections in these devices is the inaccuracy of adhesive distribution inherent in the mounting process. At 30.0 MHz and  $R = 2.5\%$ , an AT Cut crystal is roughly 0.0021 in thick, and at 40.0 MHz, this value drops to 0.0016 in. Considering a typical adhesive thickness of 0.001 in – 0.002 in, it appears that as the crystal thickness approaches the adhesive thickness, the mispositioning sensitivity effect becomes substantial and the spread in the results increases.

Figures (4) – (7) show the results of a study carried out on a 16.384 MHz rectangular AT Cut crystal mounted in the same configuration. A series of crystals were built in both the  $X'$  and  $Z'$  elongated configurations, and mounted with both single and double-ended methods. The results obtained show very different behavior for the four different configurations. The best results were obtained from the  $Z'$ -elongated crystals with double ended mounting, resulting in nominal  $\Gamma$  values at  $5 \times 10^{-10}/g$  and a spread of roughly  $2 \times 10^{-10}/g$ . The worst cases were found with the  $X'$ -elongated crystals. The  $X'$ -elongated devices with double-ended mount showed nominal values of  $2 \times 10^{-9}/g$  –  $3 \times 10^{-9}/g$  with a huge spread in the data. One plausible explanation for these differences is the difference in energy trapping found in these two orientations. The AT Cut traps better along the  $Z'$  direction than it does along the  $X'$  direction. This means that for the  $Z'$ -elongated plate the mode shape is better centered and center-localized which leads to good symmetry and less interaction of acoustic energy with the mounts.

Figure (8) shows the results of a study carried out on very small rectangular crystals. A set of 0.140 in X 0.060 in crystals used in the Vectron K-Type oscillator were mounted using four different schemes. These crystals showed relatively low numbers in the  $1 \times 10^{-9}/g$  –  $5 \times 10^{-9}/g$  range, but did not exhibit any meaningful trend. The results here show a relatively large spread with no noticeable differences between different mounting methods. These crystals were mounted to ceramic using conductive epoxy adhesive. It is likely here that the distribution of adhesive plays a role in the scattering of the data.

Figures (9) – (12) show the results of a theoretical study done with the previously developed software [1]. In this study, a rectangular crystal was considered as continuously mounted onto a pair of supporting bars with epoxy adhesive, resulting in an overhang on each side. The calculations were performed for various beam spacings and overhang lengths for a plate width of 0.076 in. and a frequency of 20 MHz. As seen in figure (11), there are optimal dimensions for which the g-sensitivity of this configuration can be made very small. Figure (12) shows the results of a similar study performed on a 0.210 in X 0.076 in  $Z'$ -elongated, 20MHz crystal. In figure 12.a the actual  $\Gamma$  components are shown separately, and it is noted that the normal component of the g-sensitivity changes sign at a beam spacing of roughly 0.125 in. This is a very important point because it means that the normal g-sensitivity can be made arbitrarily small by optimizing the beam spacing for a particular crystal.

To test this hypothesis, a series of rectangular AT Cut crystals were fabricated and mounted onto a lead frame structure as shown in figure (13). The lead frame was photo-chemically etched from stainless steel with pull-tabs which are removed after bonding to the substrate. This structure provides a very accurate geometry, and the pull-tab approach enables connections to be easily made to the crystal electrodes. Once the pull-tabs have been removed, a crystal with



dual-ended termination of metallization is mounted with conductive epoxy as shown in figure 13.b. For this purpose, a base-plating mask was developed with alignment marks to help center the blank onto the mount.

Figures (14) – (16) show the results obtained from these crystals for beam spacing of 0.120, 0.130, 0.140, and 0.150 in. It is observed here that the trend in the data is towards an optimal value of 0.140 in – 0.150 in, which follows the theoretical data in principle, with a shift in the best value from the 0.125 in prediction. It should also be noted from figure (15) that the in-plane  $\Gamma$  components remain relatively constant at  $1.2 \times 10^{-10}/g$ . Figure (16) shows a comparison of results obtained by driving fundamental and 3<sup>rd</sup> overtone modes in the same devices. The third overtone results reveal a slight minimum at the 0.140 in spacing. It was also found in these crystals that the spread in results for the 3<sup>rd</sup> overtone was tighter than that of the fundamental. This is likely caused by the superior energy trapping found in the 3<sup>rd</sup> overtone as compared with the fundamental.

Based on these preliminary results, two larger groups of resonators, a total of 120 units, were carefully manufactured to the same design with a 0.140" beam spacing. One group was plated to optimize the resonator performance at 20 MHz on the fundamental mode and the second group was optimized for third overtone operation at 60 MHz. Initially these devices were measured with the passive technique, but the absolute measurement resolution with this method is in the order of  $1.10^{-10}$  for 20 MHz resonators with Q factors below 100,000. Since many of the units are well below this value in at least one axis, oscillators were made for use on the vibration fixture. For this type of resonator this improves the measurement resolution by an order of magnitude. The results are summarized below:

#### 20 MHz Fundamental Units

	Q factor	$R_1$	$C_0$	$C_1$	$\Gamma_1$	$\Gamma_2$	$\Gamma_3$	$ \Gamma $
Mean	73.9	19.0	4.2	6.32	0.09	0.15	0.11	0.22
$\sigma$	18.7	9.1	0.9	0.17	0.05	0.09	0.06	0.08
Min	19.7	11.9	3.7	5.99	0.01	0.01	0.03	0.09
Max	106.3	67.1	7.4	6.61	0.20	0.38	0.27	0.46

#### 60 MHz 3<sup>rd</sup> Overtone Units

	Q factor	$R_1$	$C_0$	$C_1$	$\Gamma_1$	$\Gamma_2$	$\Gamma_3$	$ \Gamma $
Mean	47.5	102.2	3.9	0.59	0.08	0.16	0.17	0.27
$\sigma$	11.2	27.1	0.1	0.05	0.06	0.11	0.09	0.10
Min	27.6	62.3	3.5	0.46	0.01	0.01	0.02	0.10
Max	67.7	162.3	4.1	0.72	0.25	0.52	0.36	0.63

In these results,  $\Gamma_2$  is the normal component.  $\Gamma_1$  and  $\Gamma_3$  are the in-plane components, with  $\Gamma_3$  along the short axis and  $\Gamma_1$  along the length of the blank. The full distributions are tabulated in Appendix A and shown graphically in fig 17 a to d. It is clear from these results that it is practical to obtain g-sensitivity results for this class of resonator in the low parts in  $10^{10}$  per g, and that in this case the choice of overtone is not a dominant parameter.

Figure (18) shows the results of a study done on rectangular SC Cut resonators. In this study, a series of rectangular 20 MHz SC Cut resonators with nominal dimensions of 0.220 in X 0.090 in were fabricated by dicing the blanks from larger wafers at oblique orientations with respect to the Z' axis of the crystal. These crystals were mounted into the ceramic S-Type package as

shown in figure (2) and the  $\Gamma$  components measured. The results obtained from these crystals show a wide variation with the best values obtained at 0, 22.5, and 90°. The worst values seen in these devices were obtained at -22.5, -45.0, and -67.5°. At the best orientations nominal values of less than  $1 \times 10^{-9}/g$  were obtained, but overall the performance of these crystals was found to be poorer than the equivalent AT Cut devices.

The final study to discuss is shown in figures (19) – (21). In this study, a series of slotted clips were fabricated by photochemical etching of 0.003 in thick stainless steel, as shown in figure (19). Using these clips, a rectangular 20 MHz AT Cut Z'-elongated crystal was mounted to a ceramic substrate with small mounting blocks as shown in figure (20). Several devices were fabricated at different clip spacings, and these results are shown in figure (21). As with the lead frame devices, the in-plane  $\Gamma$  components are constant at roughly  $1-2 \times 10^{-10}/g$ , while the normal components vary with support spacing. In general, the results obtained with these devices were not as good as those obtained with the lead frames. It had been expected that the improved symmetry through the thickness obtained with the slotted clips would improve the g-sensitivity (particularly the in-plane components) of these devices. It is possible that the high profile obtained with the mounting blocks in combination with their relatively large mass degrades the performance of these devices. Future efforts with the slotted clip mounts should focus on lower profile mounts.

## Part Two Conclusions

Very low g-sensitive resonators can be manufactured using rectangular AT Cut Z'-elongated crystals with a double-ended mount that incorporates a small overhang of the crystal beyond the mount. For a well made device in this configuration, the in-plane components will remain constant at roughly  $1-2 \times 10^{-10}/g$  while optimal crystal length and beam spacing can adjust the normal component. It appears that devices of this type can be reliably fabricated with a total  $\square$  of  $2.0-3.0 \times 10^{-10}/g$  for fundamental or 3<sup>rd</sup> overtone with a reasonable yield. To produce better devices, methods for reducing the in-plane components must be addressed. The most obvious way to achieve this is by improving the symmetry of the mount in the thickness direction. Furthermore, crystal attachment methods must be improved to minimize the spread in the data.

## References

- [1] J.T. Stewart and D.S. Stevens, "Design Optimization for Acceleration Sensitivity", Proceedings of the 1998 IEEE International Frequency Control Symposium, pp. 852 – 860.
- [2] J. Stewart, "A Report on The Design Optimization of Singly and Doubly Rotated Crystal Resonators Which Minimize The Sensitivity of The Acceleration Sensitivity to Manufacturing Imperfections", Interim report submitted as part of US Army contract # N66001-97-C-8635.
- [3] R.L. Filler, "The Acceleration Sensitivity of Quartz Crystal Oscillators: A Review", IEEE Transactions on Ultrasonics, Ferroelectrics, and Frequency Control, Vol. 35, No. 3, pp. 297-305, May 1988.

# Appendix A: Tabulated results

g-sensitivity results for lead frame design, 20 MHz fundamental, 0.140" beam spacing

Unit #	Frequency (MHz)	Q (k)	R1 (ohms)	C0 (pF)	C1 (fF)	$\Gamma_1$ ( $10^{-9}/g$ )	$\Gamma_2$ ( $10^{-9}/g$ )	$\Gamma_3$ ( $10^{-9}/g$ )	$ \Gamma $ ( $10^{-9}/g$ )
1	20.061	80.5	15.5	4.0	6.35	0.01	0.01	0.13	0.13
2	20.006	91.4	14.2	3.8	6.12	0.04	0.23	0.24	0.33
3	19.996	79.0	15.3	4.0	6.57	0.01	0.27	0.05	0.27
5	20.088	82.4	14.7	4.0	6.55	0.08	0.31	0.06	0.33
6	20.036	73.8	17.7	4.1	6.08	0.10	0.24	0.09	0.28
7	20.044	85.4	14.6	4.2	6.39	0.06	0.01	0.14	0.15
8	20.048	90.3	13.9	4.0	6.34	0.06	0.04	0.05	0.09
9	20.029	96.0	13.0	3.9	6.39	0.03	0.28	0.05	0.29
10	20.048	19.7	67.1	4.2	5.99	0.09	0.11	0.12	0.19
11	20.005	49.1	26.6	3.9	6.09	0.09	0.09	0.12	0.17
12	20.005	67.2	17.9	4.0	6.61	0.08	0.25	0.09	0.28
13	20.046	70.2	17.2	4.0	6.59	0.08	0.29	0.06	0.31
14	20.064	92.1	14.2	4.0	6.06	0.10	0.04	0.19	0.22
16	20.036	86.9	13.9	4.2	6.60	0.15	0.05	0.10	0.19
17	19.995	95.6	12.9	4.0	6.43	0.04	0.22	0.03	0.23
18	20.054	80.3	15.6	3.8	6.33	0.11	0.14	0.23	0.29
19	20.013	69.5	17.8	3.9	6.42	0.13	0.18	0.11	0.25
20	20.052	27.6	44.3	4.0	6.49	0.11	0.03	0.10	0.15
21	20.023	72.4	17.0	4.0	6.45	0.11	0.17	0.13	0.24
22	20.032	83.5	15.2	4.0	6.26	0.18	0.16	0.10	0.26
23	20.049	75.0	16.2	4.0	6.54	0.15	0.09	0.22	0.28
24	20.014	91.4	14.0	3.8	6.20	0.07	0.17	0.05	0.19
25	20.057	80.8	16.1	3.8	6.11	0.17	0.12	0.15	0.26
26	20.012	87.4	14.2	6.9	6.39	0.04	0.20	0.25	0.32
27	20.072	54.7	22.7	6.9	6.37	0.04	0.13	0.07	0.15
28	20.038	84.6	14.8	4.0	6.36	0.06	0.21	0.14	0.26
30	20.052	46.5	28.0	3.8	6.10	0.05	0.15	0.03	0.16
31	20.068	79.9	16.0	3.9	6.20	0.05	0.01	0.08	0.09
32	20.075	32.1	39.3	3.8	6.28	0.08	0.38	0.25	0.46
33	20.024	68.3	18.2	3.9	6.40	0.05	0.15	0.04	0.16
34	20.045	88.7	13.8	4.0	6.50	0.08	0.29	0.15	0.34
35	20.012	63.1	19.3	3.9	6.53	0.04	0.16	0.12	0.20
37	20.020	81.3	15.4	3.8	6.34	0.09	0.12	0.09	0.17
38	20.071	58.4	22.4	3.9	6.06	0.03	0.10	0.27	0.29
39	20.037	85.0	14.5	3.9	6.45	0.13	0.34	0.18	0.41
40	20.010	98.9	12.9	4.0	6.25	0.02	0.25	0.05	0.26
41	20.050	93.8	13.1	4.0	6.48	0.19	0.15	0.07	0.25
42	20.065	59.2	20.9	4.1	6.42	0.16	0.15	0.10	0.24
43	20.033	60.7	21.3	3.9	6.15	0.05	0.03	0.22	0.23
44	20.048	93.0	13.4	4.0	6.36	0.08	0.06	0.05	0.11
45	20.014	83.5	14.6	7.0	6.53	0.15	0.13	0.11	0.23
46	20.052	73.2	17.3	3.9	6.27	0.07	0.04	0.08	0.11

48	20.031	82.5	15.9	4.1	6.05	0.09	0.21	0.08	0.24
49	20.039	106.3	11.9	4.1	6.26	0.03	0.13	0.08	0.16
50	20.078	69.1	18.5	4.1	6.21	0.03	0.08	0.07	0.11
51	20.055	40.3	31.5	3.8	6.25	0.11	0.02	0.08	0.14
52	20.045	82.5	16.0	3.7	6.00	0.07	0.10	0.17	0.21
54	20.047	74.1	16.5	3.9	6.51	0.07	0.15	0.14	0.22
55	20.049	92.5	14.2	3.9	6.03	0.09	0.01	0.14	0.17
56	20.019	85.8	15.1	7.4	6.14	0.18	0.24	0.07	0.31
57	20.043	59.9	21.4	4.1	6.20	0.13	0.17	0.05	0.22
58	20.072	36.4	34.9	4.1	6.26	0.17	0.09	0.08	0.21
60	20.063	83.3	14.6	4.2	6.52	0.16	0.14	0.07	0.22
62	20.024	51.4	25.0	4.1	6.19	0.05	0.09	0.07	0.12
63	19.987	55.1	22.4	4.1	6.46	0.06	0.12	0.06	0.15
64	20.057	87.5	14.3	7.0	6.33	0.08	0.15	0.08	0.19
65	20.035	69.4	18.2	4.0	6.28	0.06	0.18	0.05	0.20
66	20.024	77.9	15.7	4.1	6.51	0.20	0.14	0.16	0.29

g-sensitivity results for lead frame design, 60 MHz 3<sup>rd</sup> overtone, 0.140" beam spacing

Unit #	Frequency (MHz)	Q (k)	R1 (ohms)	C0 (pF)	C1 (fF)	$\Gamma_1$ (10 <sup>-9</sup> /g)	$\Gamma_2$ (10 <sup>-9</sup> /g)	$\Gamma_3$ (10 <sup>-9</sup> /g)	$ \Gamma $ (10 <sup>-9</sup> /g)
102	59.981	67.7	64.8	4.0	0.61	0.02	0.17	0.03	0.17
103	59.956	66.7	64.4	4.0	0.62	0.07	0.37	0.18	0.42
104	59.875	56.1	78.1	4.0	0.61	0.01	0.01	0.18	0.18
105	59.852	65.6	62.3	4.1	0.65	0.05	0.10	0.29	0.31
106	59.872	39.4	127.4	3.9	0.53	0.03	0.08	0.19	0.21
107	59.940	57.5	70.6	3.9	0.65	0.03	0.17	0.04	0.18
108	59.984	49.2	90.2	4.1	0.60	0.02	0.22	0.07	0.23
109	59.961	38.6	117.1	3.9	0.59	0.19	0.26	0.04	0.32
110	59.881	38.9	109.7	4.0	0.62	0.25	0.22	0.04	0.34
111	59.980	48.9	102.8	3.6	0.53	0.10	0.03	0.13	0.17
112	59.849	38.4	104.1	4.0	0.66	0.01	0.52	0.36	0.63
113	59.991	52.1	90.9	4.1	0.56	0.08	0.31	0.02	0.32
114	59.813	38.2	112.1	4.0	0.62	0.17	0.12	0.16	0.26
115	59.913	47.1	87.6	4.1	0.64	0.08	0.20	0.04	0.22
116	59.747	50.8	84.9	4.0	0.62	0.18	0.18	0.03	0.26
117	59.919	59.9	70.1	3.8	0.63	0.06	0.09	0.20	0.23
118	59.850	51.5	88.6	3.7	0.58	0.04	0.16	0.19	0.25
120	59.884	61.6	66.6	4.0	0.65	0.03	0.16	0.19	0.25
121	59.923	57.1	75.3	3.9	0.62	0.09	0.01	0.20	0.22
122	59.959	54.8	104.5	3.5	0.46	0.10	0.02	0.21	0.23
123	59.864	60.6	68.8	4.1	0.64	0.07	0.19	0.20	0.28
124	59.896	58.7	83.0	3.9	0.55	0.04	0.16	0.11	0.20
125	59.872	65.0	64.0	4.1	0.63	0.14	0.04	0.14	0.20
127	59.851	45.4	98.5	4.1	0.59	0.01	0.08	0.28	0.29
129	59.825	52.6	84.1	3.9	0.60	0.20	0.16	0.23	0.34
134	59.989	34.8	138.4	4.0	0.55	0.05	0.08	0.03	0.10
135	59.983	44.0	108.2	3.9	0.56	0.07	0.15	0.29	0.33

138	59.899	44.0	103.5	3.8	0.58	0.04	0.14	0.30	0.33
139	59.882	35.3	133.4	3.9	0.56	0.04	0.07	0.23	0.24
141	59.780	43.5	121.6	3.7	0.50	0.10	0.18	0.04	0.21
142	59.919	37.6	130.9	3.7	0.54	0.03	0.20	0.12	0.24
144	60.012	36.9	132.5	3.9	0.54	0.03	0.02	0.20	0.20
145	59.894	35.2	124.2	3.9	0.61	0.02	0.04	0.21	0.21
146	59.870	27.6	134.2	3.9	0.72	0.09	0.06	0.20	0.23
147	60.030	47.4	105.7	3.7	0.53	0.13	0.14	0.16	0.25
148	59.953	58.3	74.9	3.9	0.61	0.04	0.09	0.24	0.26
149	59.938	52.0	98.8	3.7	0.52	0.06	0.14	0.22	0.27
150	59.925	56.8	86.9	3.8	0.54	0.02	0.19	0.14	0.24
151	59.827	28.7	149.4	3.8	0.62	0.03	0.25	0.22	0.33
155	59.779	30.6	153.8	3.9	0.57	0.15	0.23	0.08	0.29
156	59.855	34.6	122.5	3.8	0.63	0.01	0.11	0.23	0.26
158	59.773	53.9	85.5	3.8	0.58	0.08	0.14	0.18	0.24
159	59.862	31.6	142.6	3.8	0.59	0.14	0.26	0.12	0.32
161	59.876	48.8	117.5	3.8	0.46	0.14	0.47	0.35	0.60
162	59.885	32.6	162.3	3.8	0.50	0.05	0.02	0.22	0.23

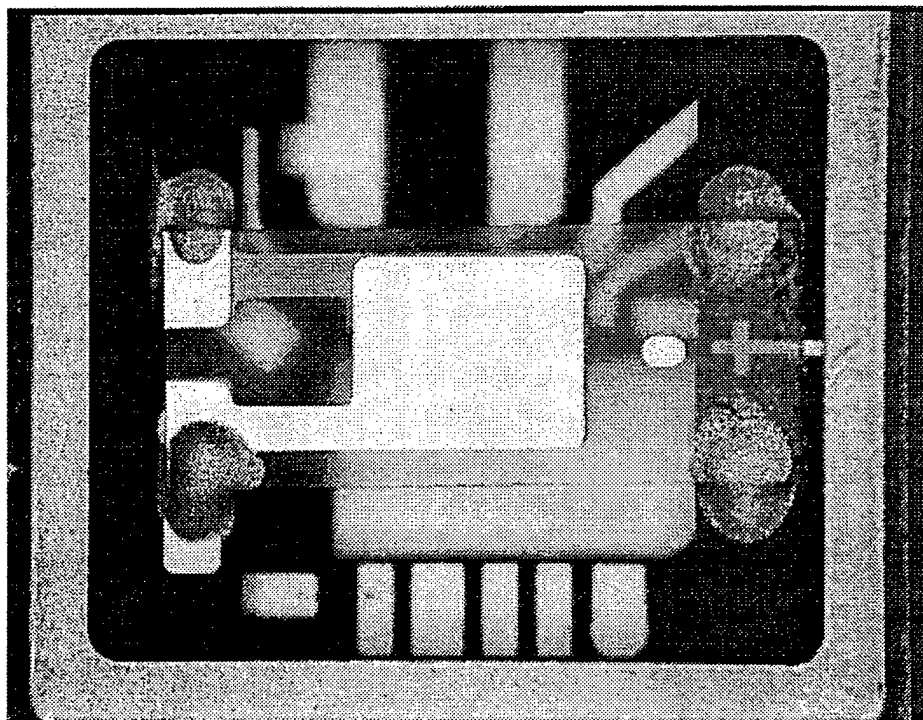
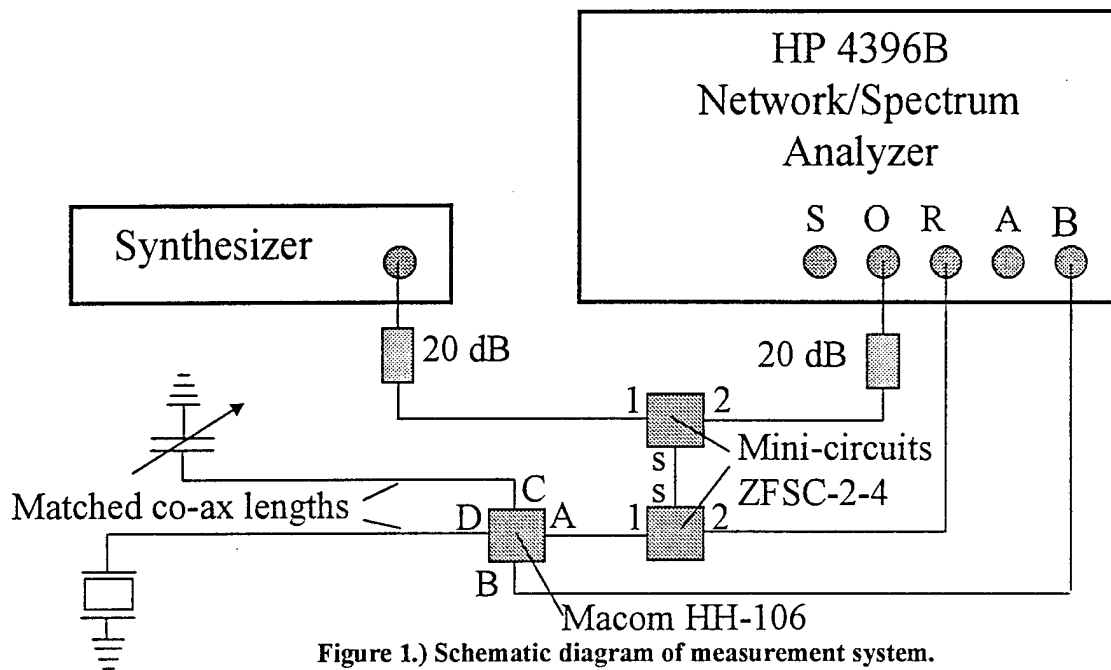


Figure 2.) Rectangular AT/SC Cut crystal with double-ended mount in S-Type ceramic package.

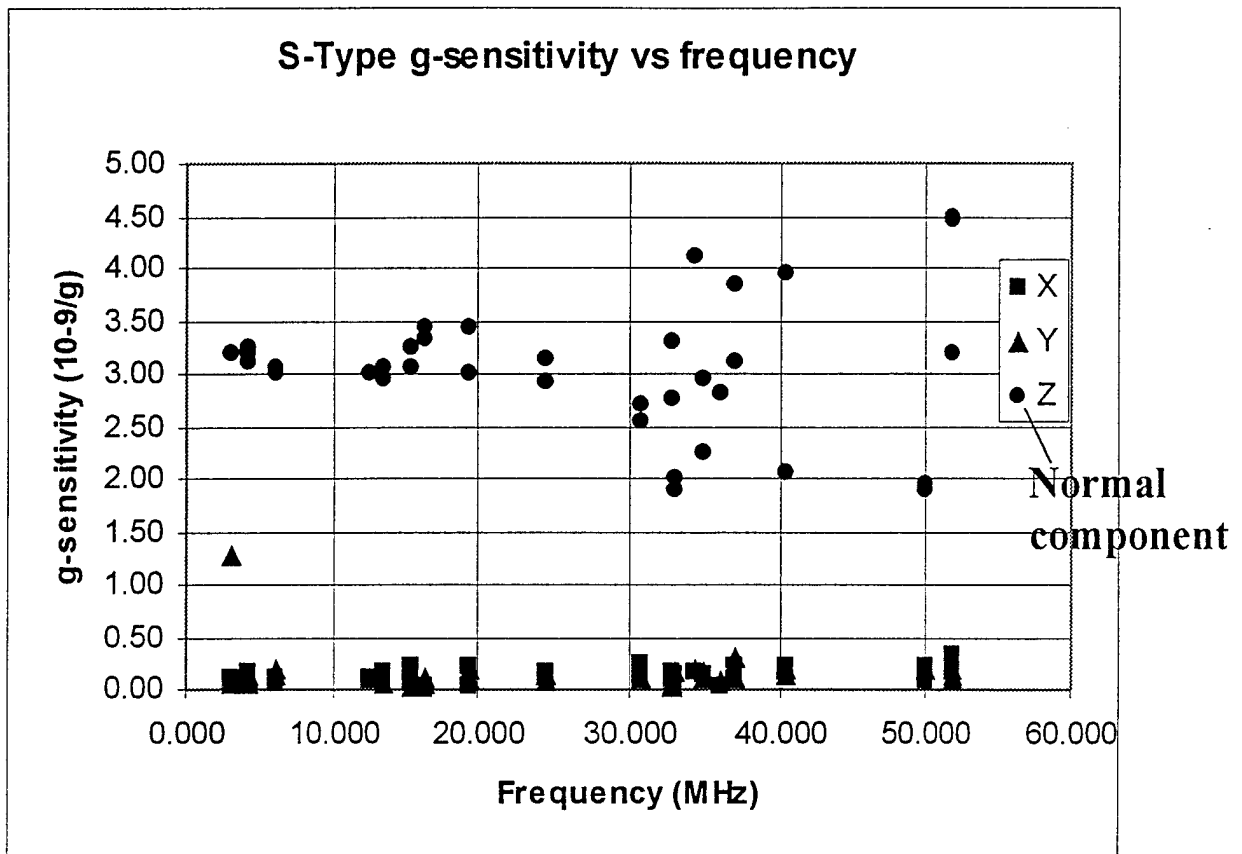


Figure 3.)  $\Gamma$  Vs. Frequency for rectangular AT Cut plate.

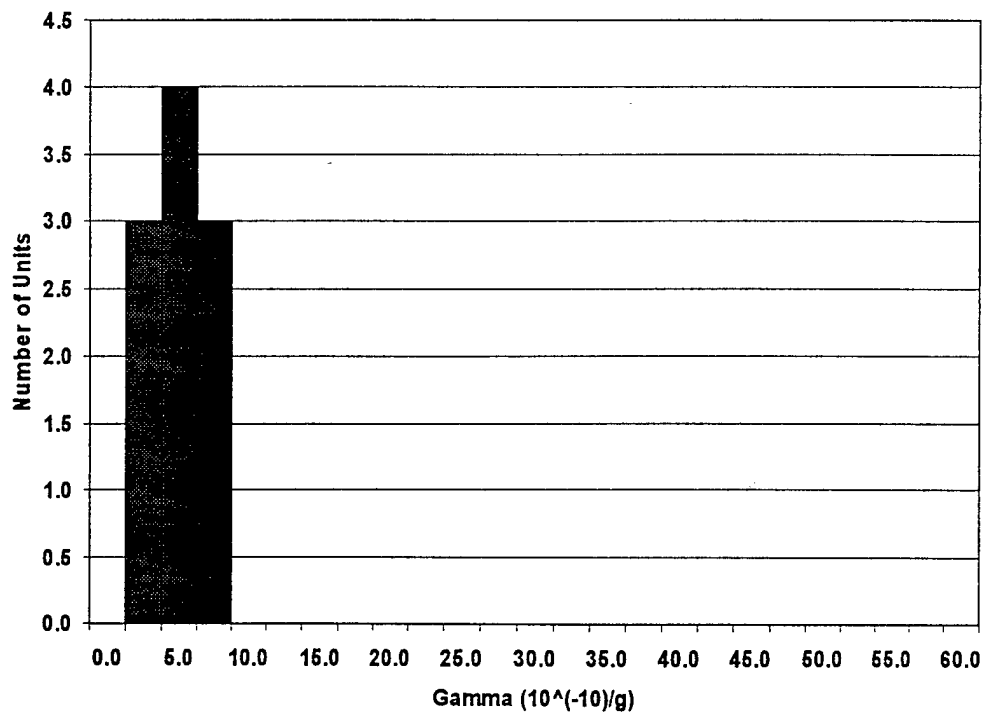


Figure 4.) Distribution of results - Z' elongated, double-ended mount.

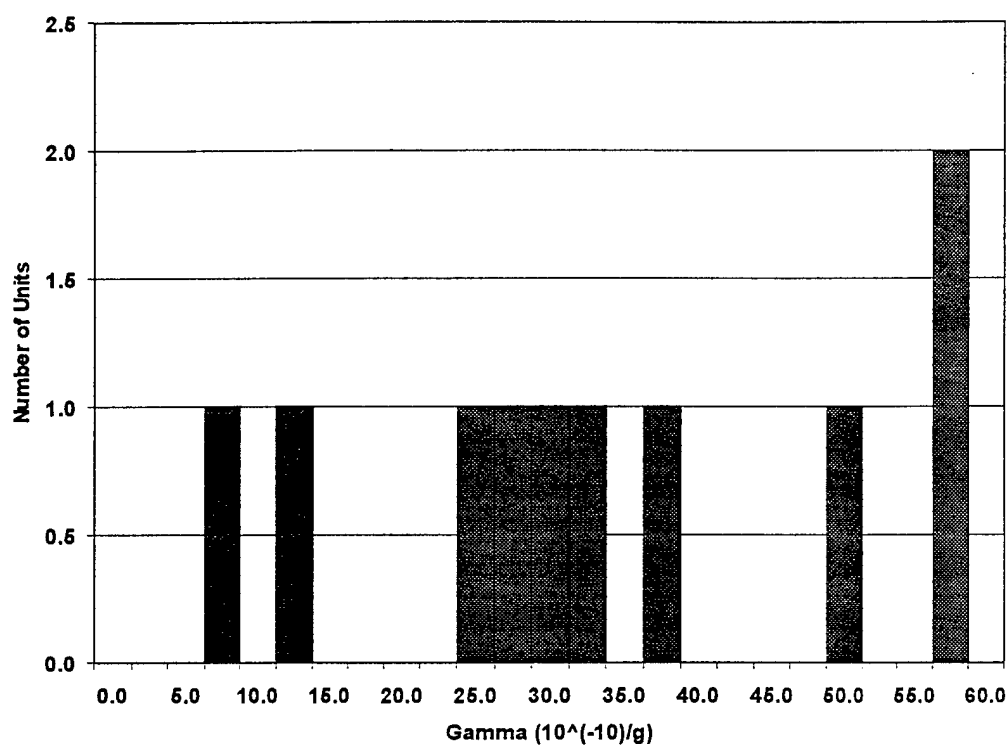


Figure 5.) Distribution of results - X' elongated, double-ended mount.

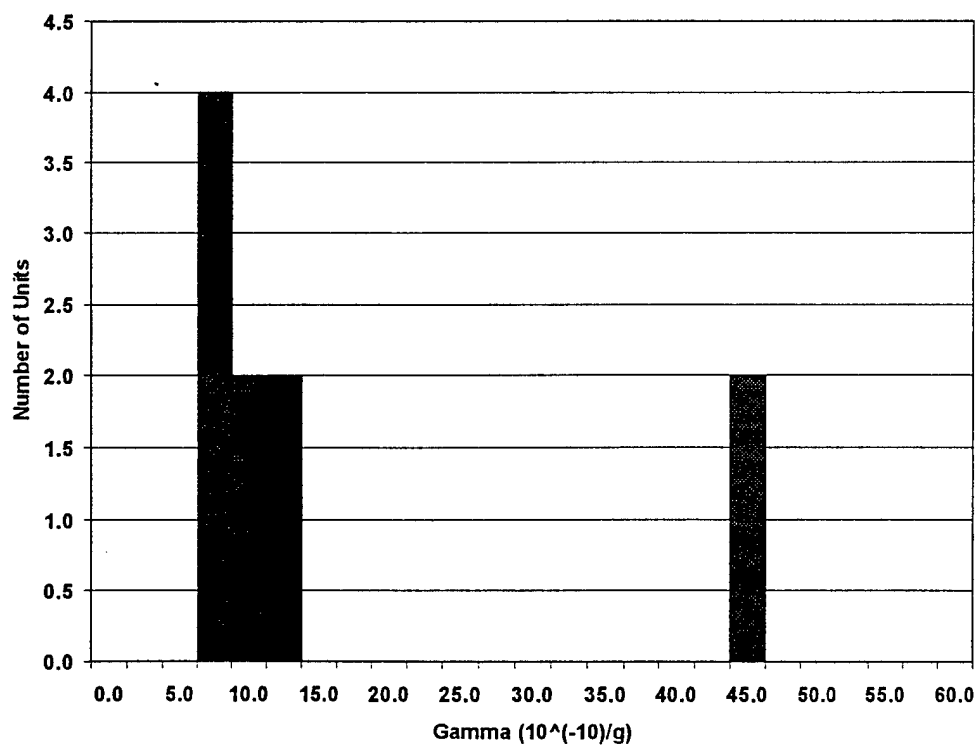


Figure 6.) Distribution of results - Z' elongated, single-end mount.



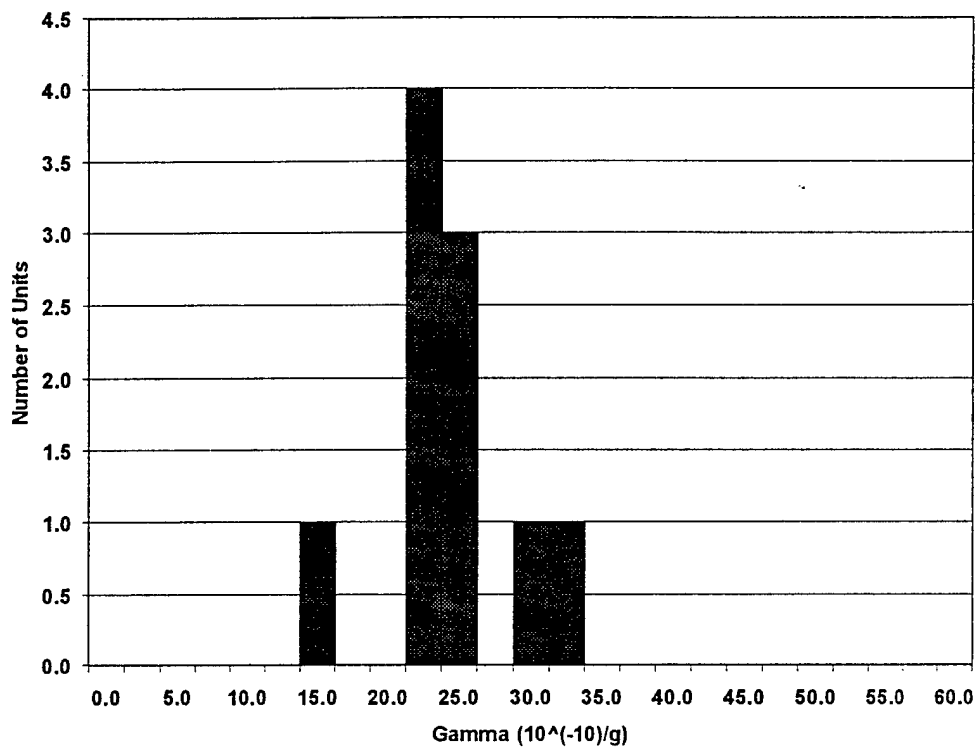


Figure 7.) Distribution of results - X' elongated, single-end mount.

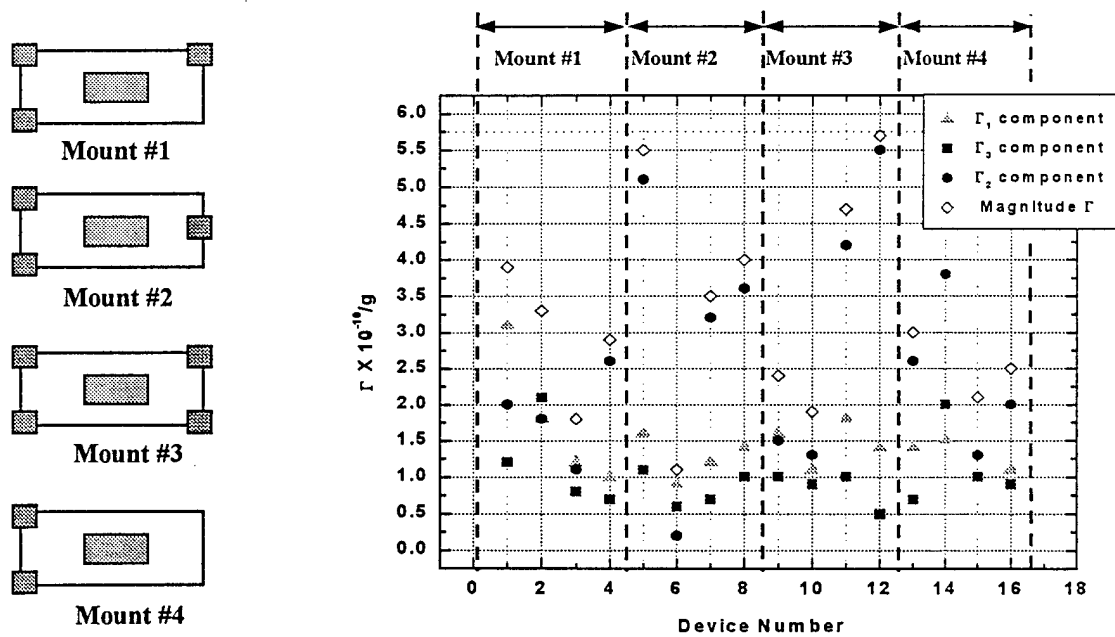


Figure 8.) Distribution of results for small K-Type crystals, AT Cut.

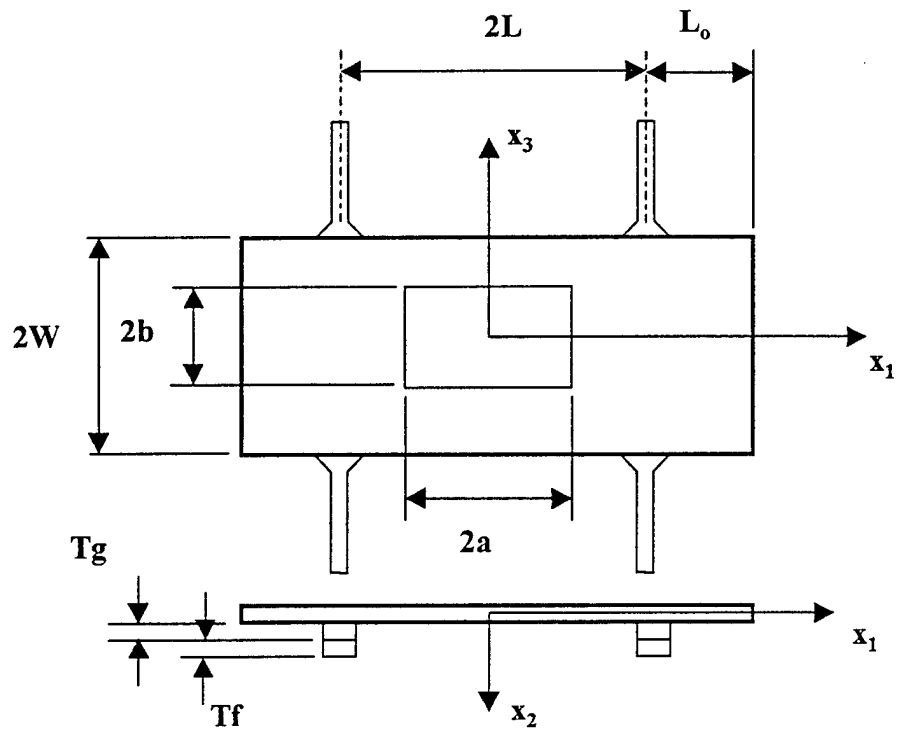


Figure 9.) Geometry used for FEA study on rectangular AT Cut with overhang mount.

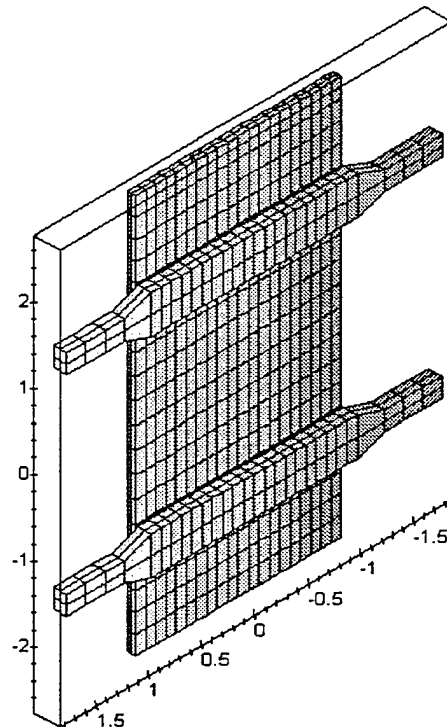


Figure 10.) Typical FEA model used for study on rectangular AT Cut with overhang mount.

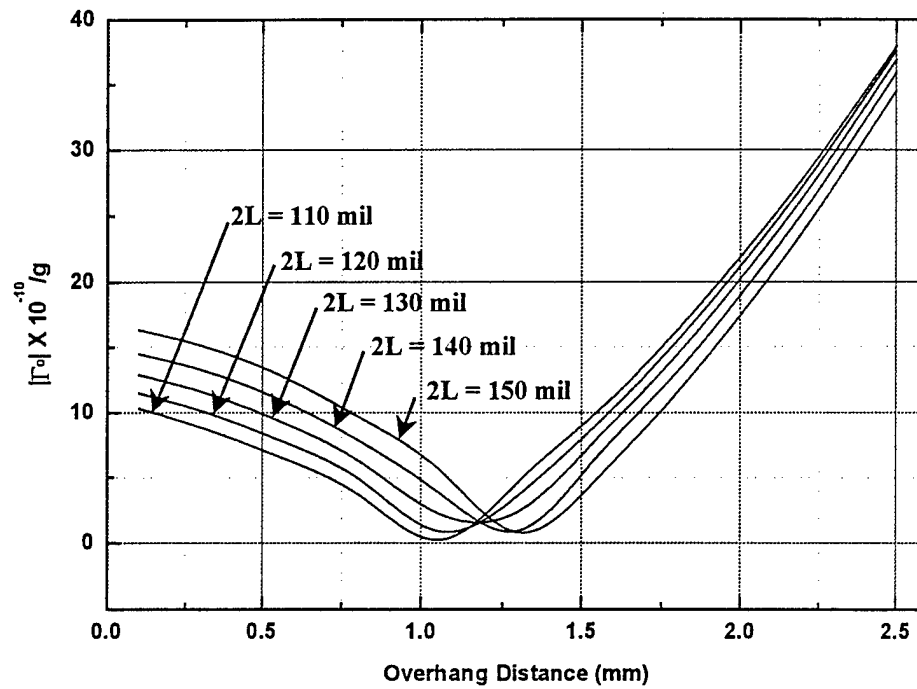


Figure 11.a.) Variation of  $\Gamma$  with overhang length for various values of support beam spacing.

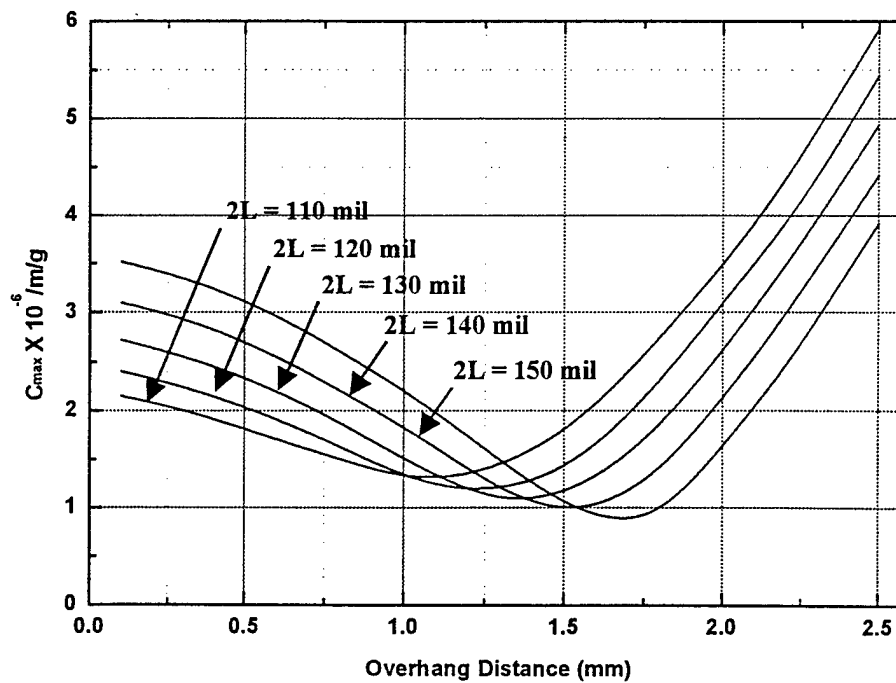


Figure 11.b.) Variation of  $C_{\max}$  with overhang length for various values of support beam spacing.

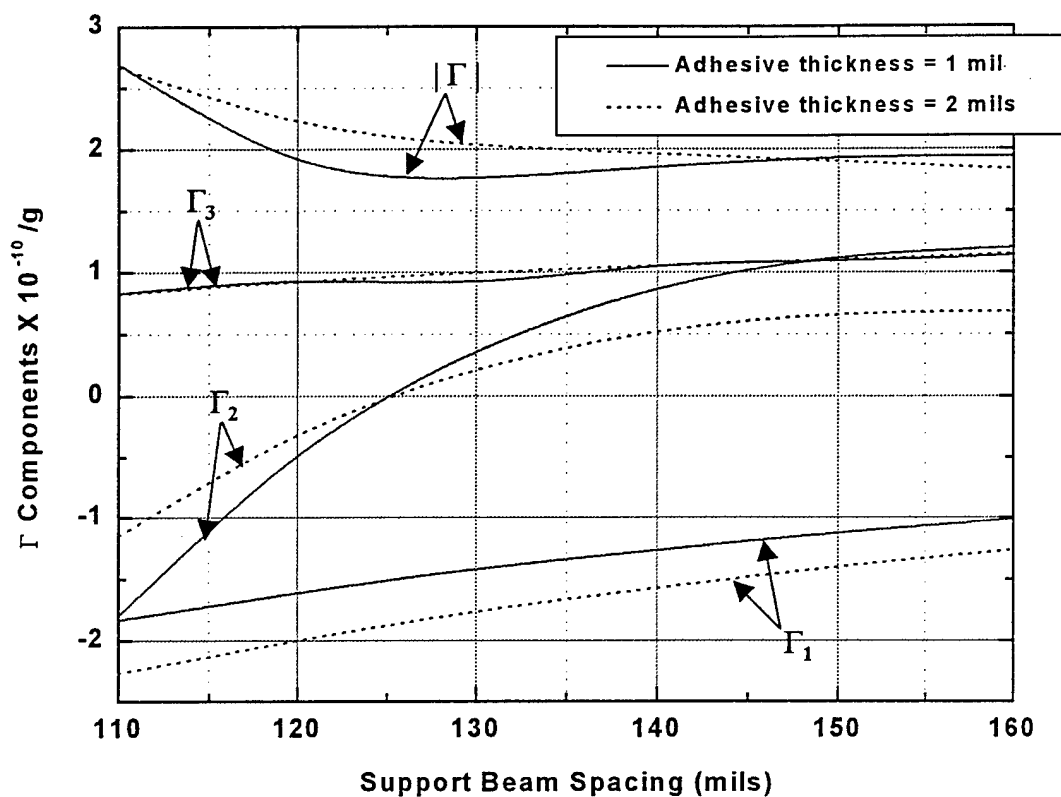


Figure 12.a.) Variation of  $\Gamma$  components with support beam spacing, 0.210 in length crystal.

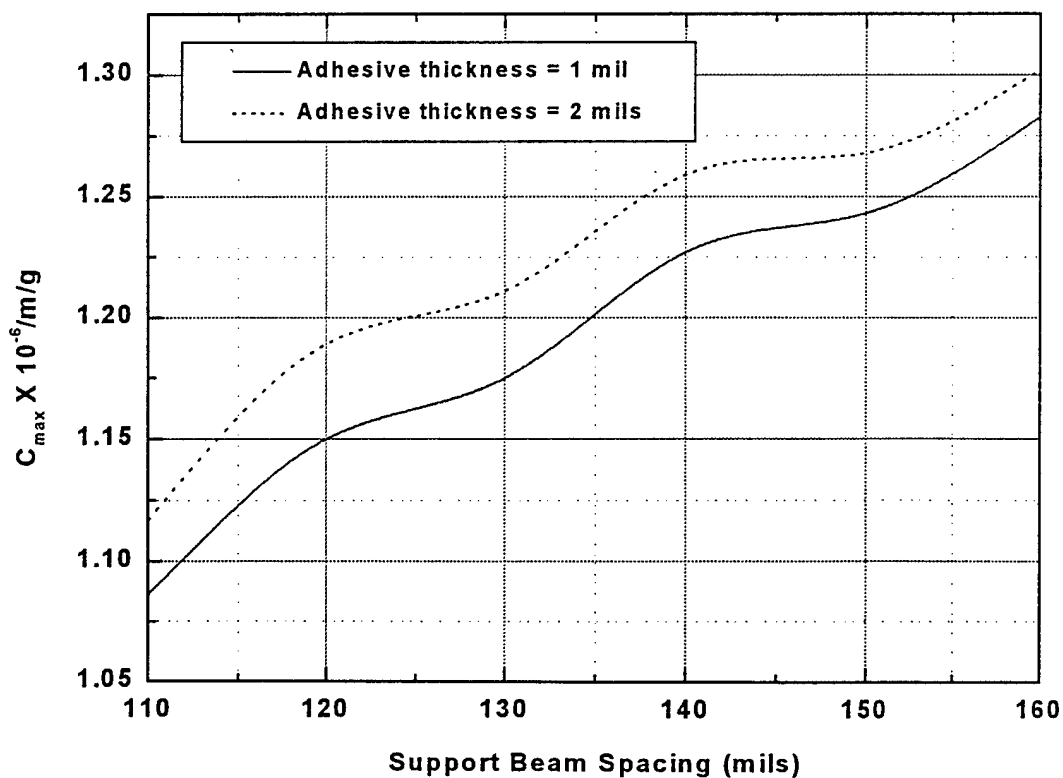


Figure 12.b.) Variation of  $C_{max}$  with support beam spacing, 0.210 in length crystal.

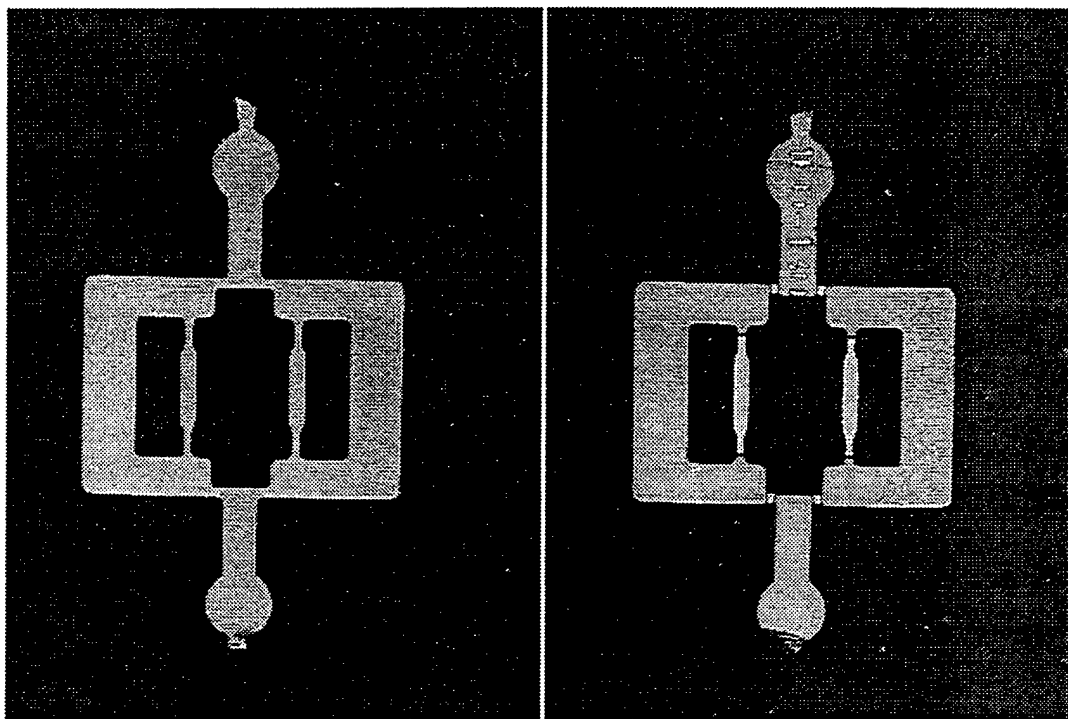


Figure 13.a.) Photochemical-Etched lead frame.

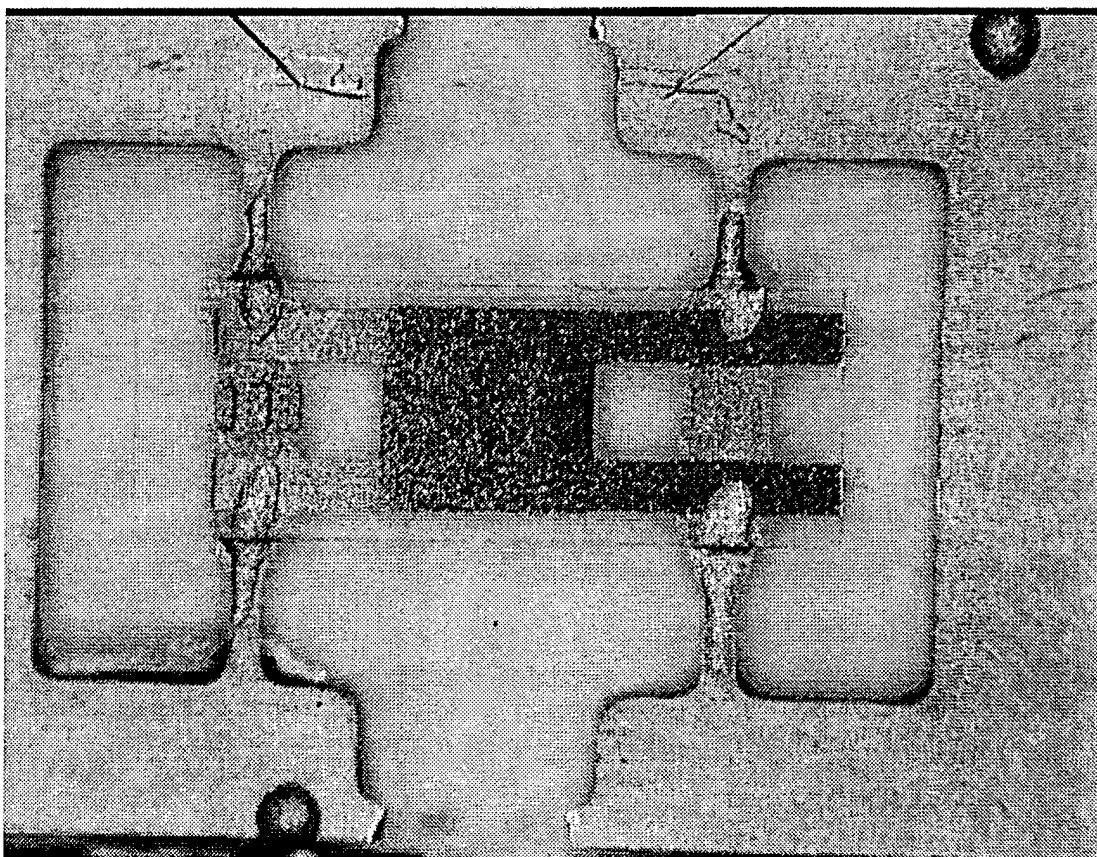


Figure 13.b.) Lead frame mounted Rectangular AT Cut crystal.

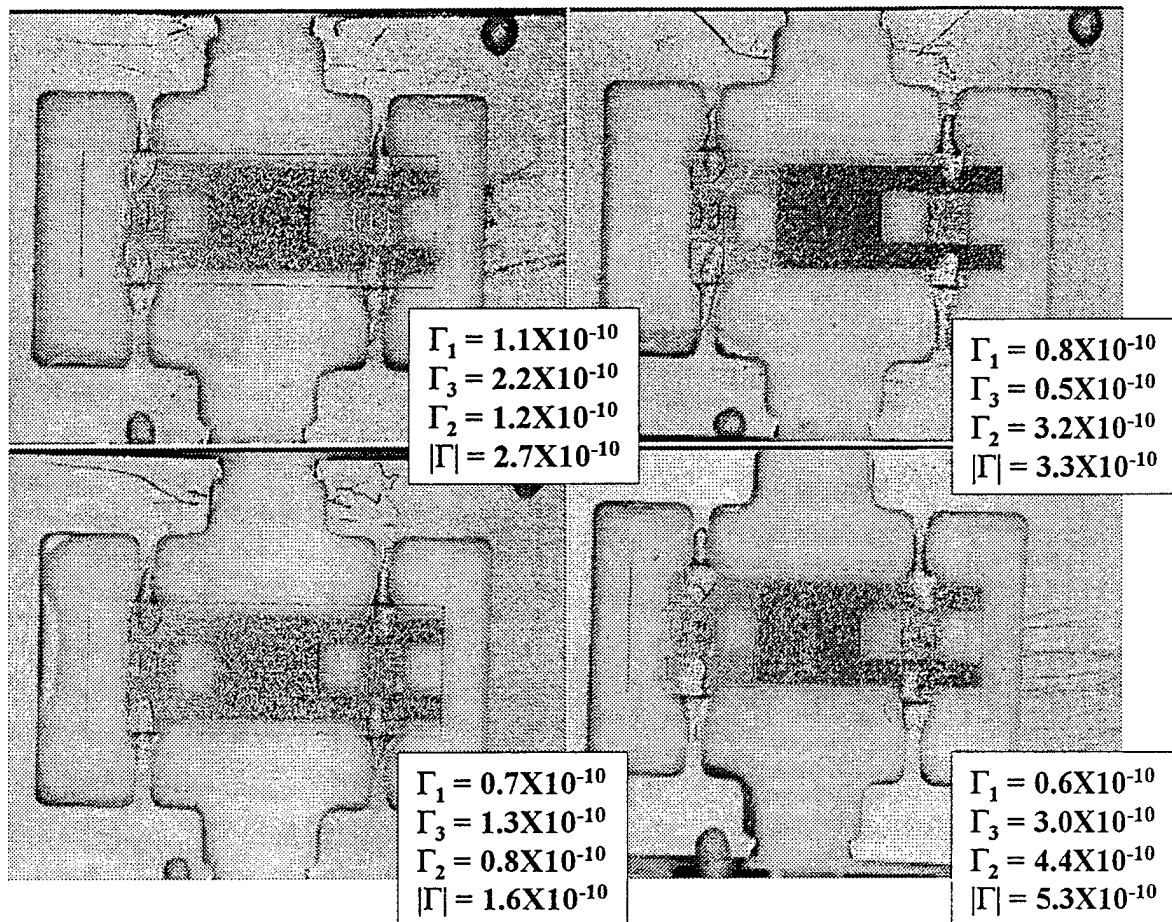


Figure 14.a.) Results for various lead frame mounted devices.

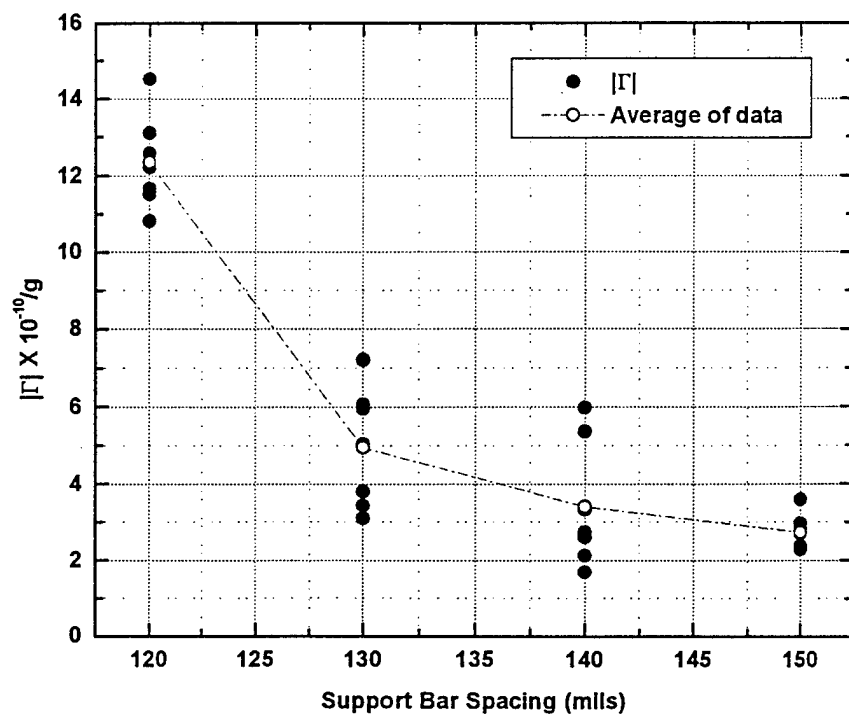


Figure 14.b.) Variation of  $\Gamma$  magnitude with support beam spacing, lead frame mount.

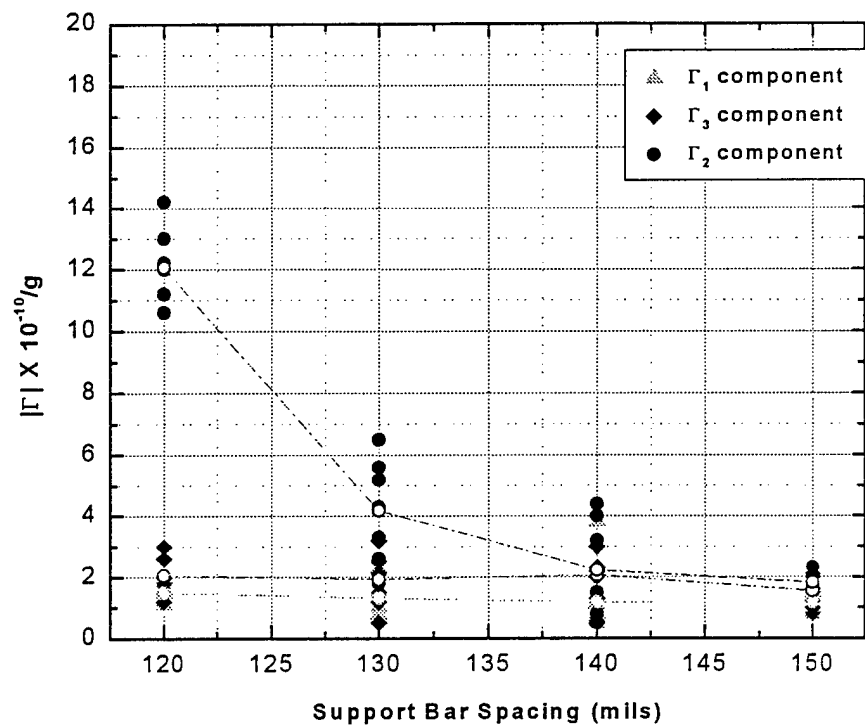


Figure 15.) Variation of  $\Gamma$  components with support beam spacing, lead frame mount.

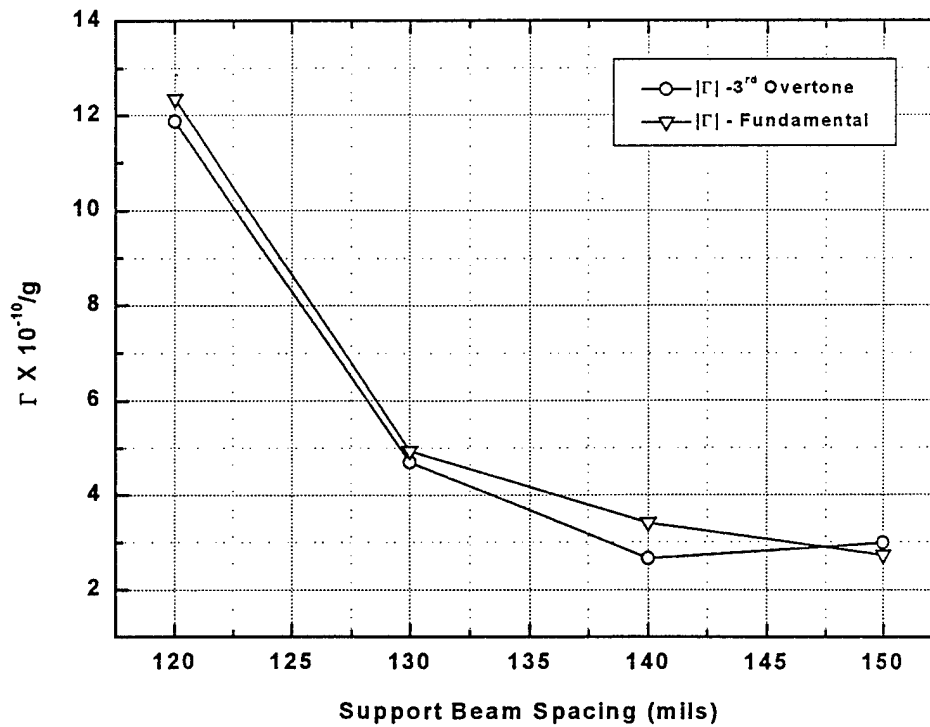


Figure 16.) Comparison of  $\Gamma$  magnitude for fundamental and 3rd O.T., lead frame mount.

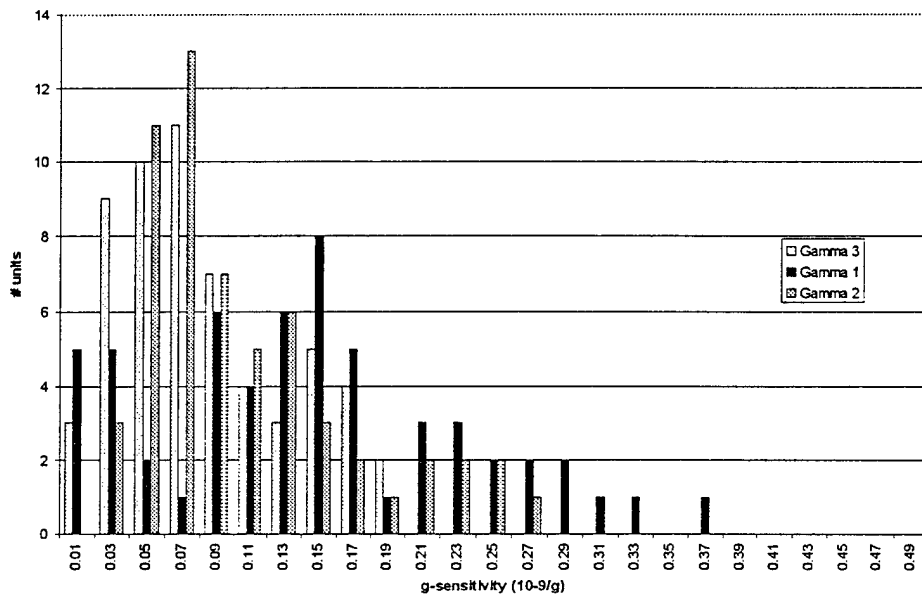


Fig 17a. Distribution of  $\Gamma$  in each of the three axes, lead frame design, 20 MHz fundamental, 0.140" beam spacing

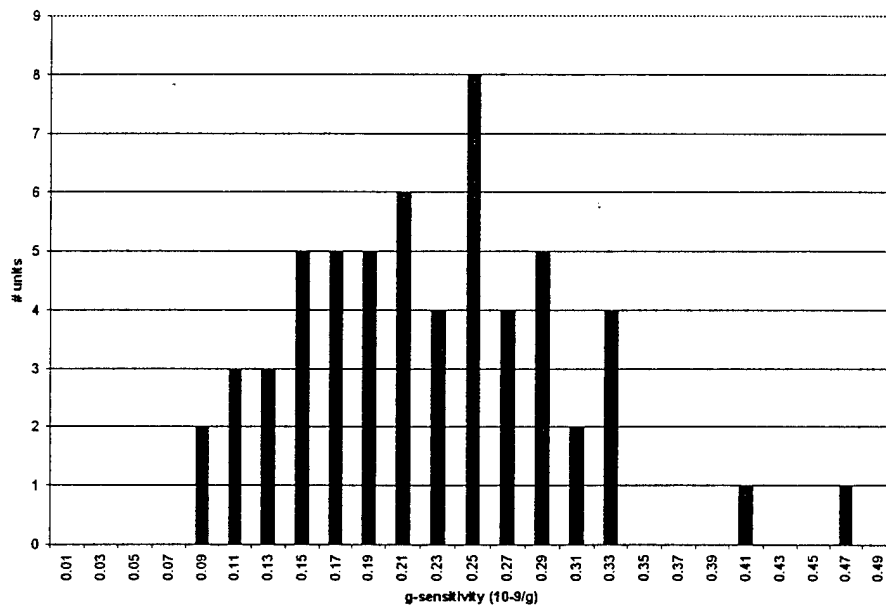


Fig 17b. Distribution of  $|\Gamma|$ , lead frame design, 20 MHz fundamental, 0.140" beam spacing



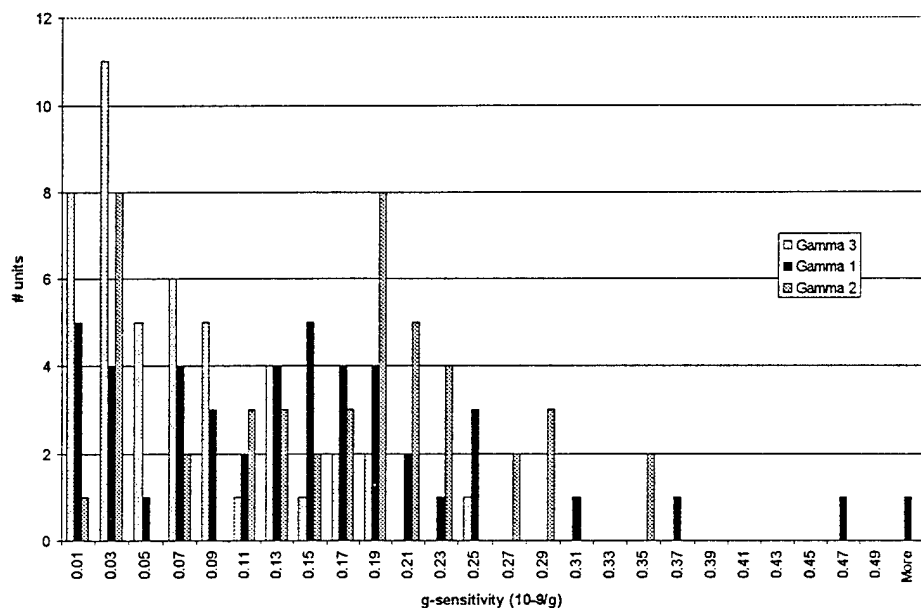


Fig 17c. Distribution of  $\Gamma$  in each of the three axes, lead frame design, 60 MHz 3rd overtone, 0.140" beam spacing

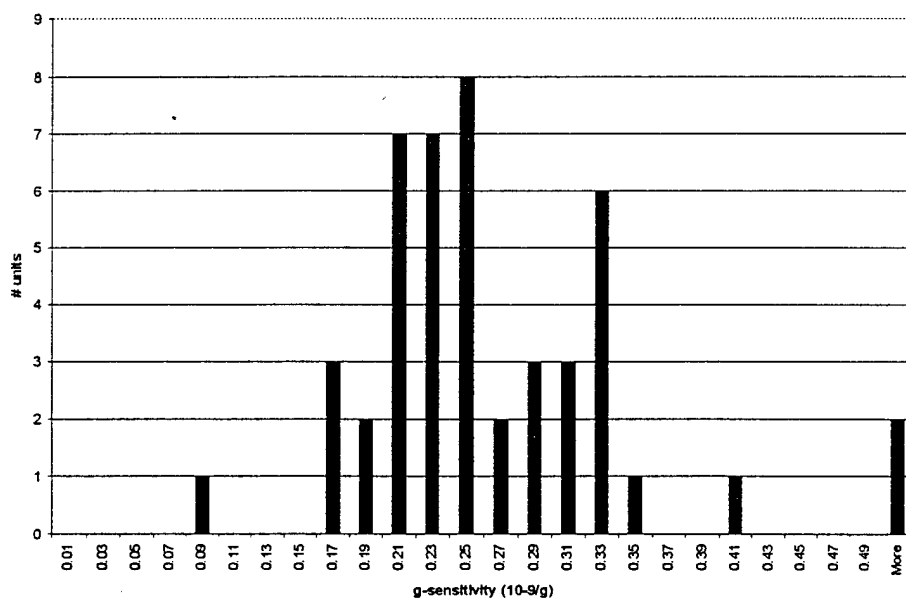


Fig 17d. Distribution of  $|\Gamma|$ , lead frame design, 60 MHz 3rd overtone, 0.140" beam spacing

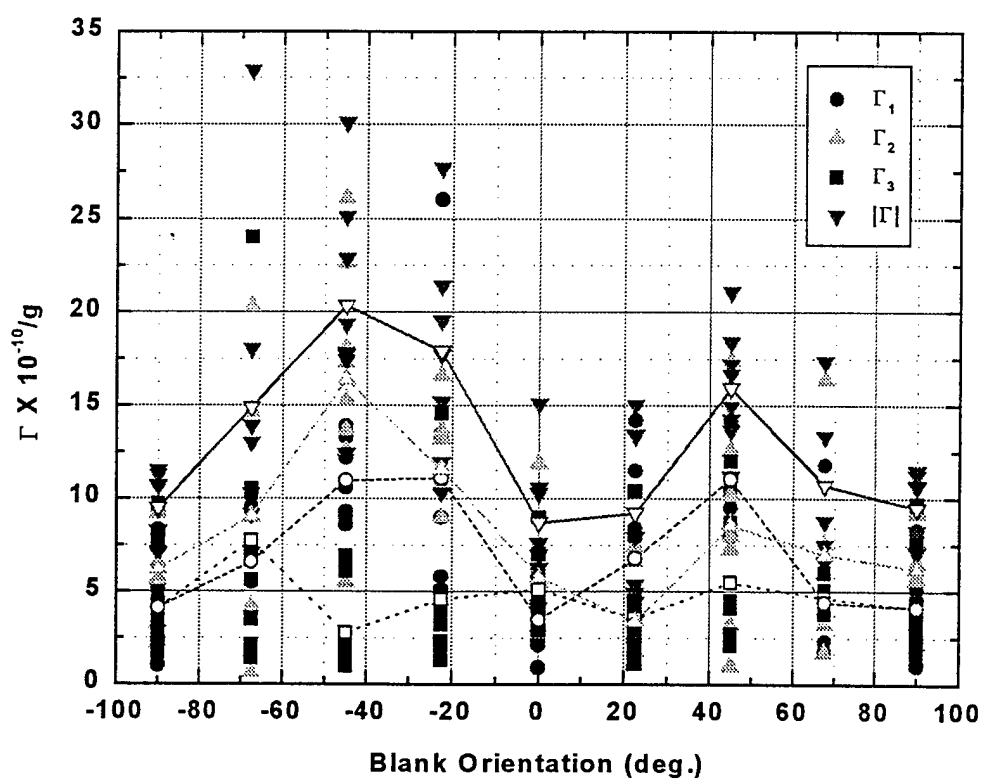
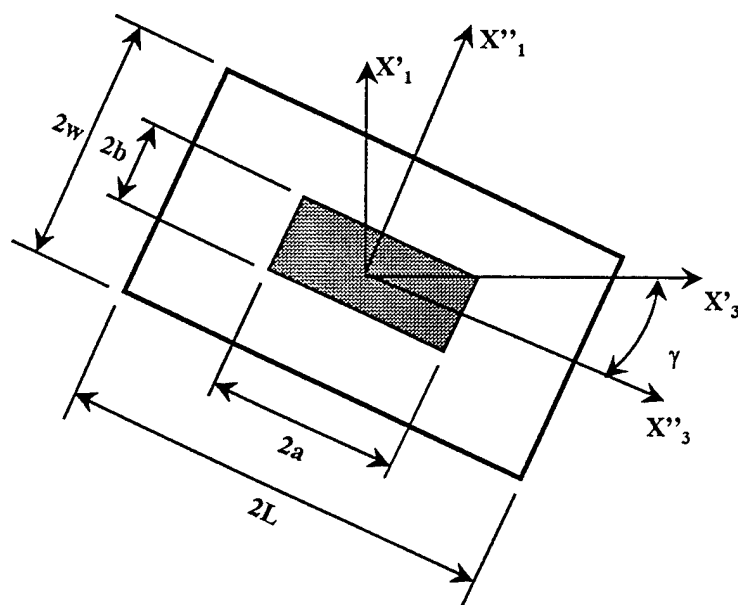


Figure 18.) Variation of  $\Gamma$  components with blank orientation, SC Cut, double end mount.

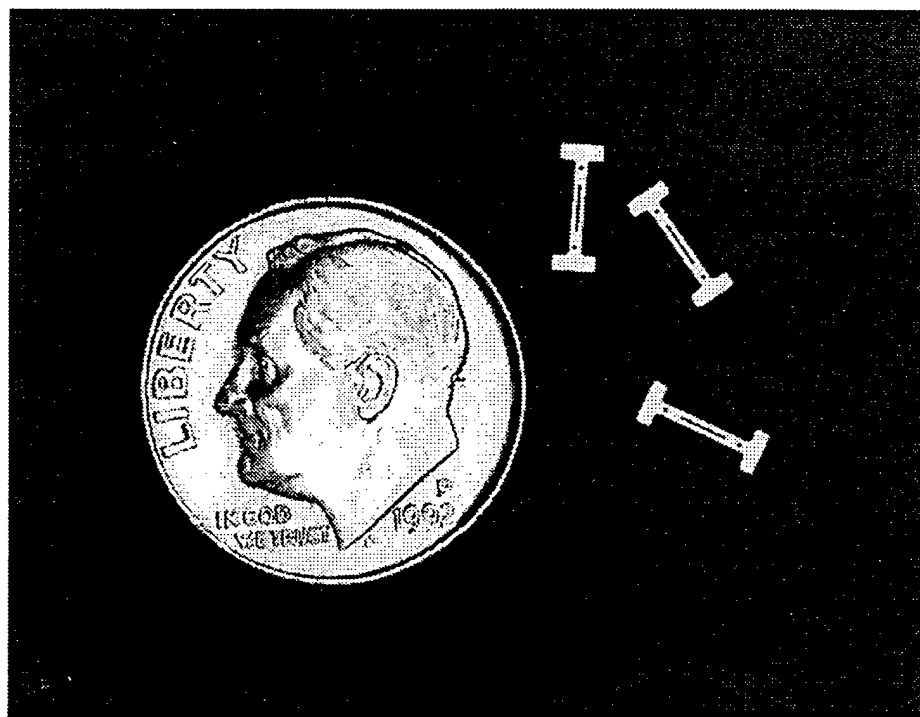
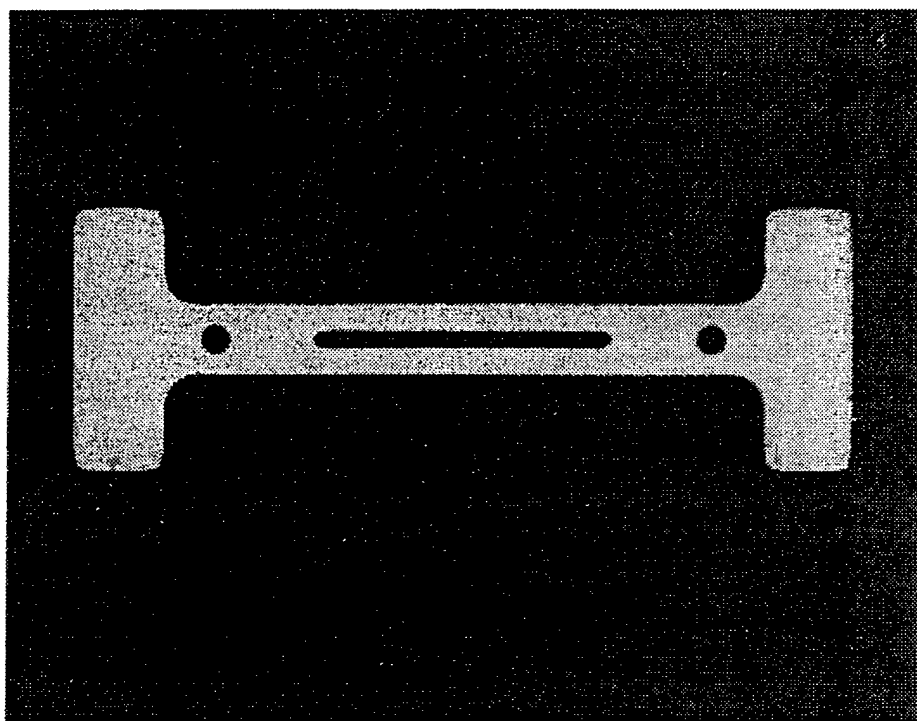


Figure 19.) Slotted clip for mounting rectangular crystals.

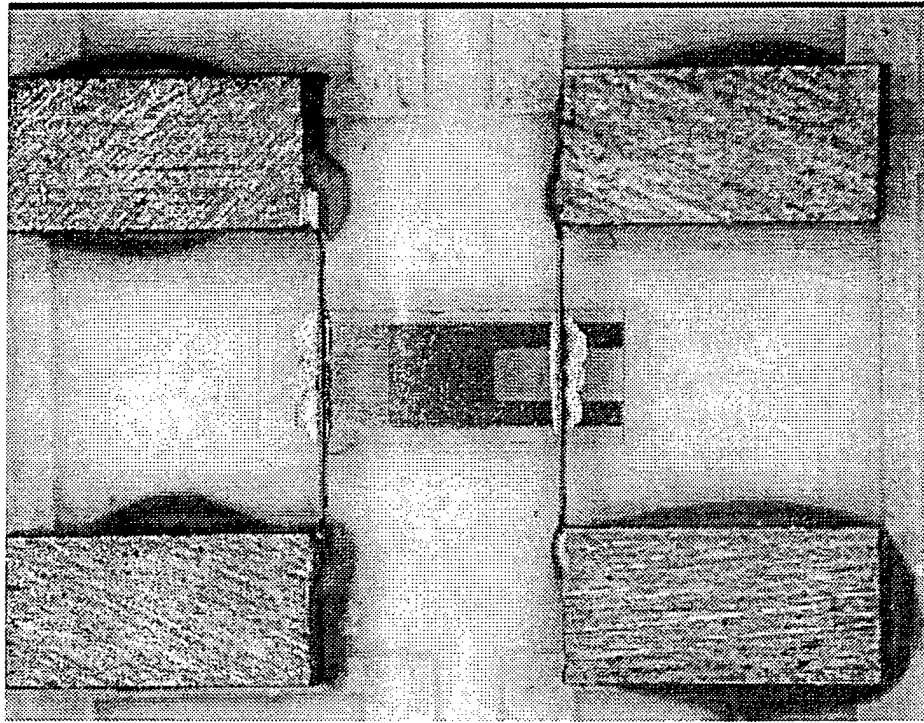


Figure 20.) Rectangular AT Cut Z'-elongated crystal mounted with slotted clips.

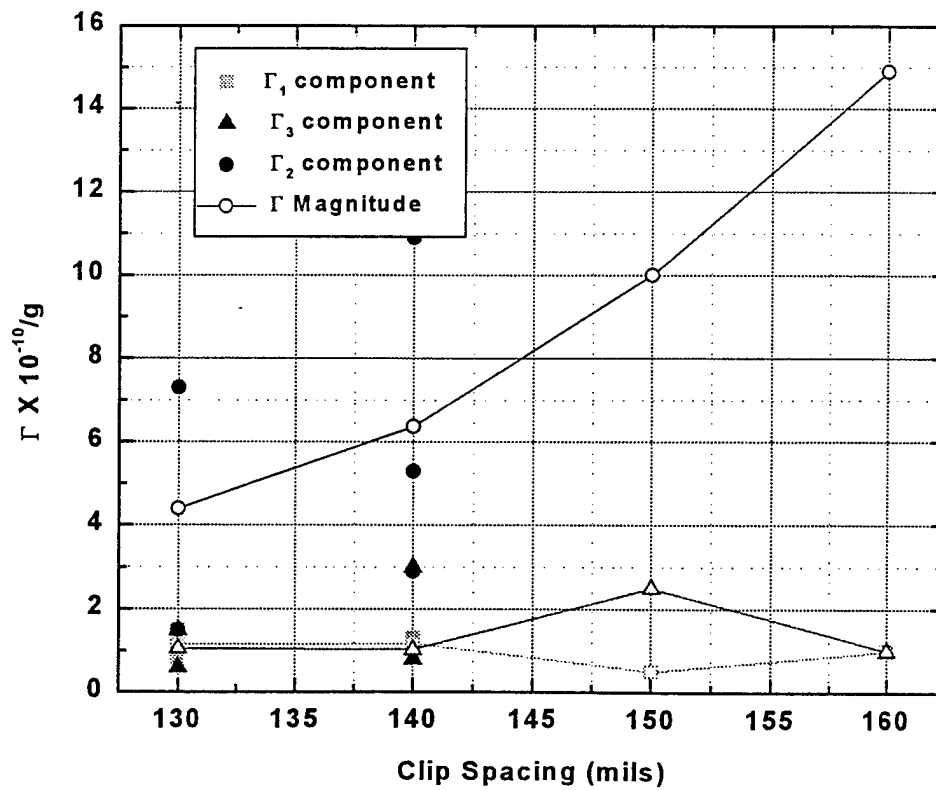


Figure 21.) Variation of  $\Gamma$  with support spacing for slotted clip mounted crystals.

**Part 3: Report on the Development of the Miniature Low Power SDIL & DDIL  
OCXOs for Low G-sensitivity applications.**

This part consists of slides and textual material that was delivered and discussed as part of the final contract review meeting.

---

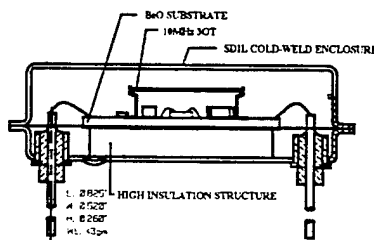
***ARMY CONTRACT#N66001-97-C-8635  
Low G-Sensitive Quartz Resonators, and  
Low-Power Clock Utilizing the Resonators***

SDIL & DDIL OCXO DEVELOPMENT



## Background & Concept

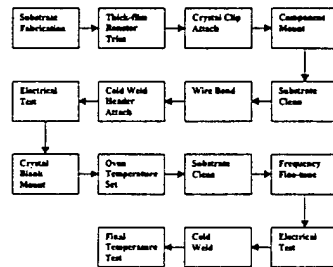
- OCXO's insulation can be improved by evacuating the package. If aging performance is adequate, then an open blank crystal can be utilized directly.
- Utilize proven cold weld techniques for hybrid package.



The overall intent of this development is to produce a new class of OCXO's with smaller size, lower power dissipation and better characteristics in vibration than existing technology can deliver. The overall concept was developed after a careful analysis of previous efforts to develop evacuated OCXO's. The advantage of evacuating the package is a dramatic improvement in thermal insulation. **If** outgassing and contamination issues can be resolved, then the resonator does not require a separate package and the entire module becomes dramatically simpler (and smaller). Achieving adequate cleanliness was a major concern from the outset of this project and was the reason why the aging testing was started as quickly as possible. Although a number of packaging options were considered, including ceramic, it was ultimately determined that the best chance for success was to utilize cold weld sealing. Cold welding is the standard choice for high precision resonators, but is essentially not used for hybrid microcircuits. The Single DIL package was previously tooled for a different application, but the DDIL package and sealing dies needed to be designed and procured.

## ***Material Selection & Processing***

- BeO used (only in substrate form) for the heat spreading substrate
- Conventional thick-film materials used on the substrate



The above flow chart shows a typical process flow for these devices. BeO was selected to minimize thermal gradients across the temperature controlled substrate, and conventional aluminum oxide was chosen for the lower level. Standard thick-film metallization, epoxies and inks were used. Electrical components, including inductors, were chosen from Vectron's standard hybrid component inventory. Although these components have been proven over many years in lower stability XO's and VCXO's, the outgassing characteristics needed to be proven in this application.



### ***DIL OCXO Platforms***

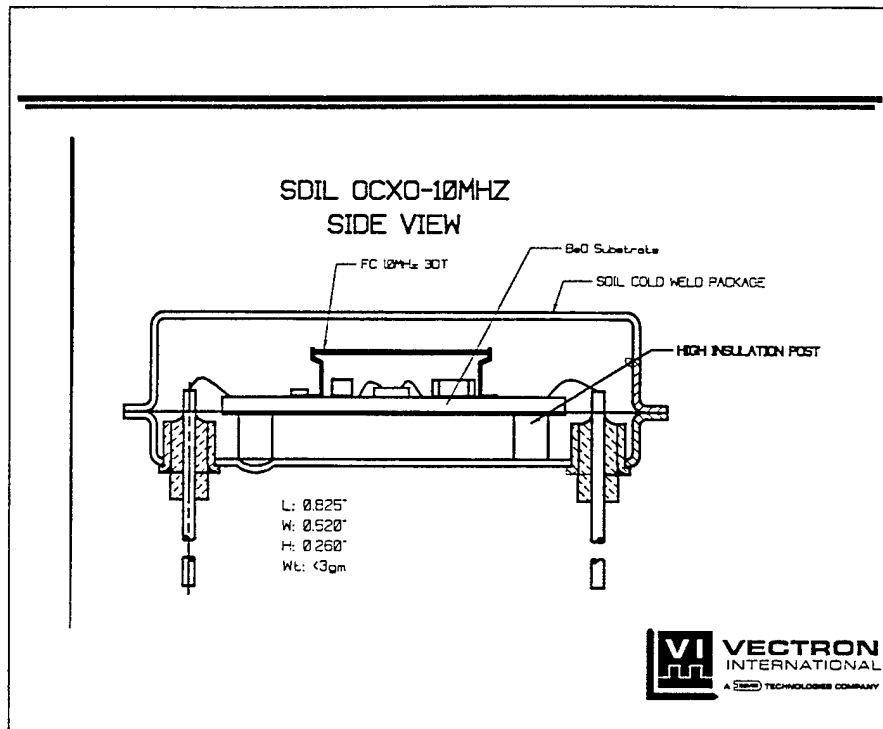
---

- SDIL OCXO - 10MHz
- SDIL OCXO - 100MHz
- DDIL OCXO - 10MHz
- DDIL OCXO - 100MHz

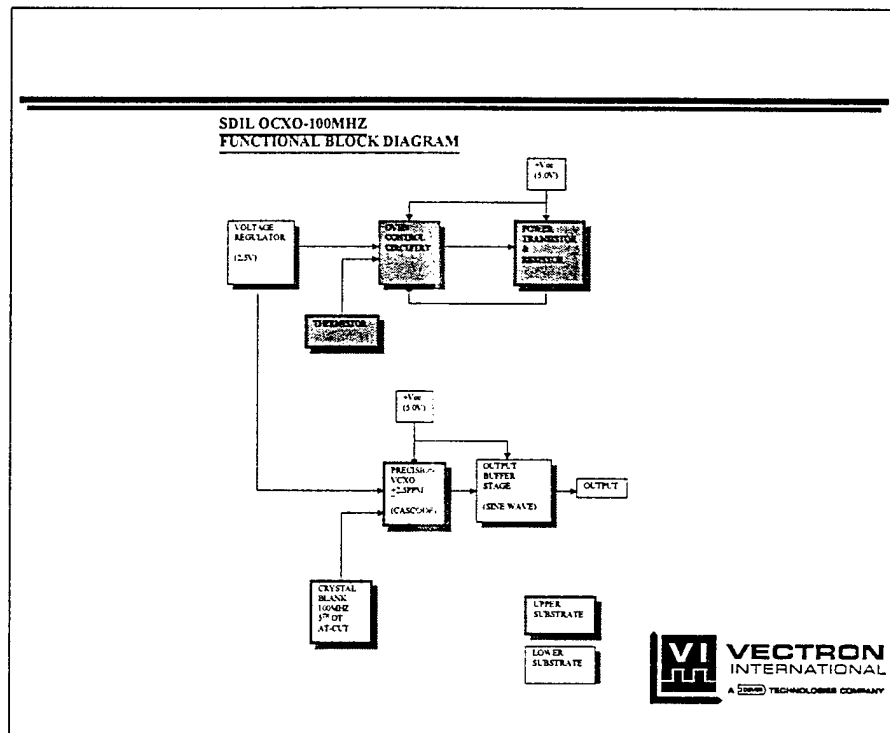


The original intent was to have both HF and VHF devices with two levels of performance, thus the choice of 10 & 100 MHz with two package sizes. HF devices exhibit superior aging, while VHF is an advantage when generating microwave signals. Since phase noise degrades by  $20\log N$  when the frequency is multiplied, lower multiplication ratio's result in lower phase noise degradation.

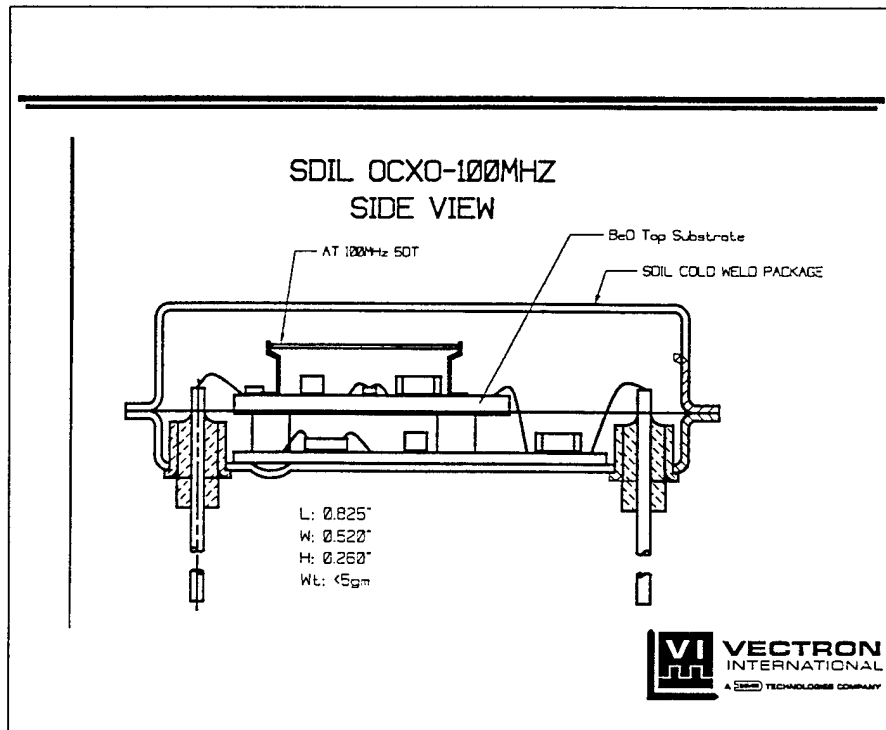




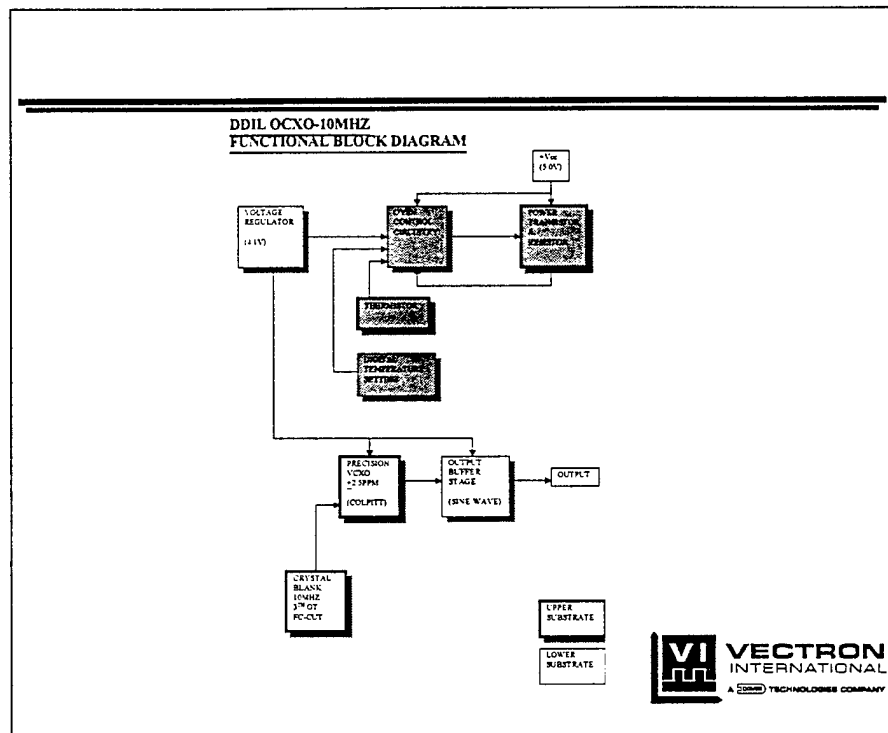
As can be seen in the drawing, the substrate is heated and heat flows to the resonator through the mounting clips. Three small posts are used to suspend the substrate off the package floor and thermally isolate the heated OCXO substrate from the metal housing. The metal package is sealed with the cold-welding technique under a high vacuum level environment. I/O interconnects are provided by wirebonding the thermally isolated substrate directly to the posts of the package. As depicted in the above slide, the overall dimension of the SDIL OCXO is 0.825"x0.520"x0.260". The net weight is slightly under 3gm.



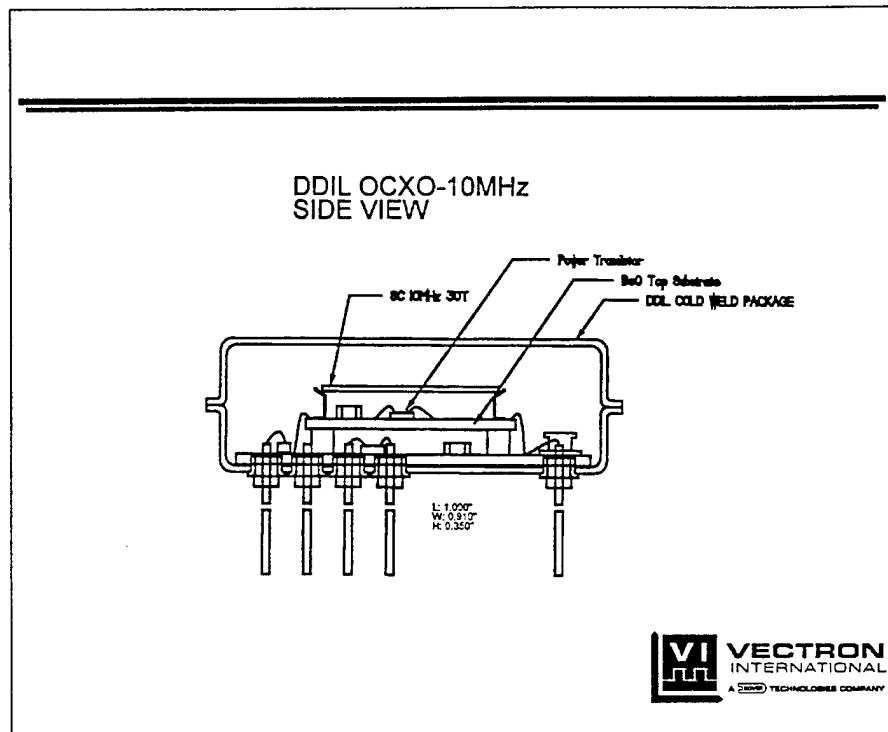
With the 100 MHz SDIL devices, it was desirable to sink the output amplifier heat to the package case. Thus, a two level approach was developed wherein the circuitry which is not temperature sensitive is located on the lower substrate. This is critical since heat rise due to uncontrolled power can cause the oven to prematurely shut down at higher temperatures. Given the very high thermal resistance of around 500°C/W, this becomes a more critical factor than in conventional OCXO's.



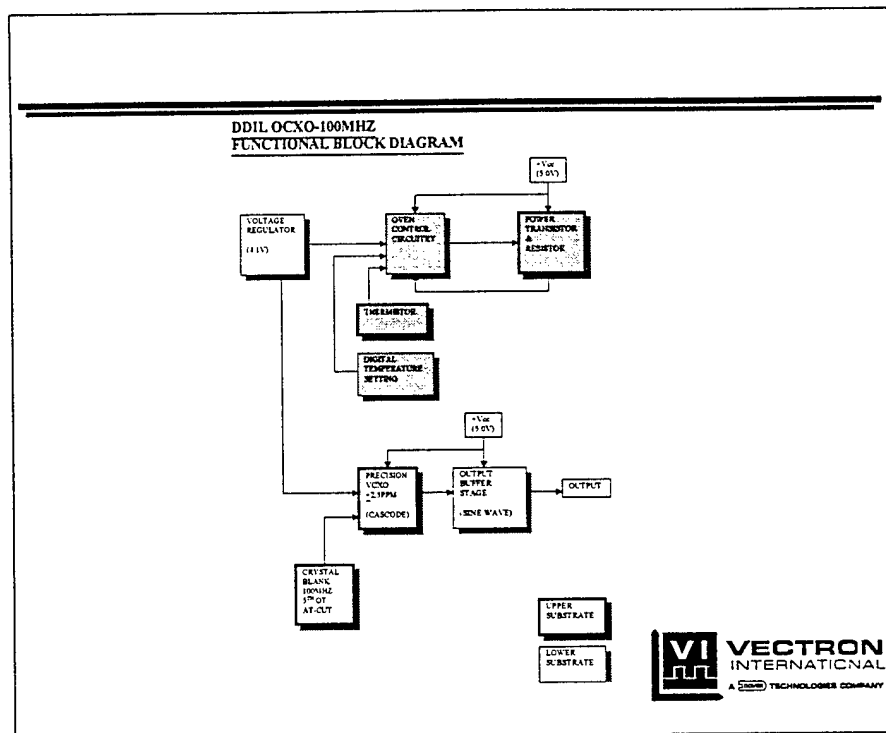
The 100MHz SDIL design uses the same package as the 10 MHz SDIL, but an additional substrate is added for the reasons described on the previous slide. The temperature-controlled portion of the OCXO is housed on the top substrate with the BeO material. The Bi-level interconnection is joined via wirebonding. Although the overall dimension is exactly the same as the 10MHz SDIL, the net weight is roughly 2 gm higher.



The oscillator for the 10 MHz DDIL is a Colpitts configuration with a bipolar transistor. As expected, the Allan deviation is much superior on this part as is the overall stability. In addition, the temperature is set with a programmable pot thereby allowing fine adjustments after sealing. In addition, the 10MHz DDIL also utilizes the 2-level substrate design approach.



This design also uses a two level structure to dissipate unregulated heat. The package has also been enlarged to accommodate a larger crystal and more sophisticated circuitry.



The electrical design of the 100 MHz DDIL is also a Colpitts, but with the necessary modifications for frequency.



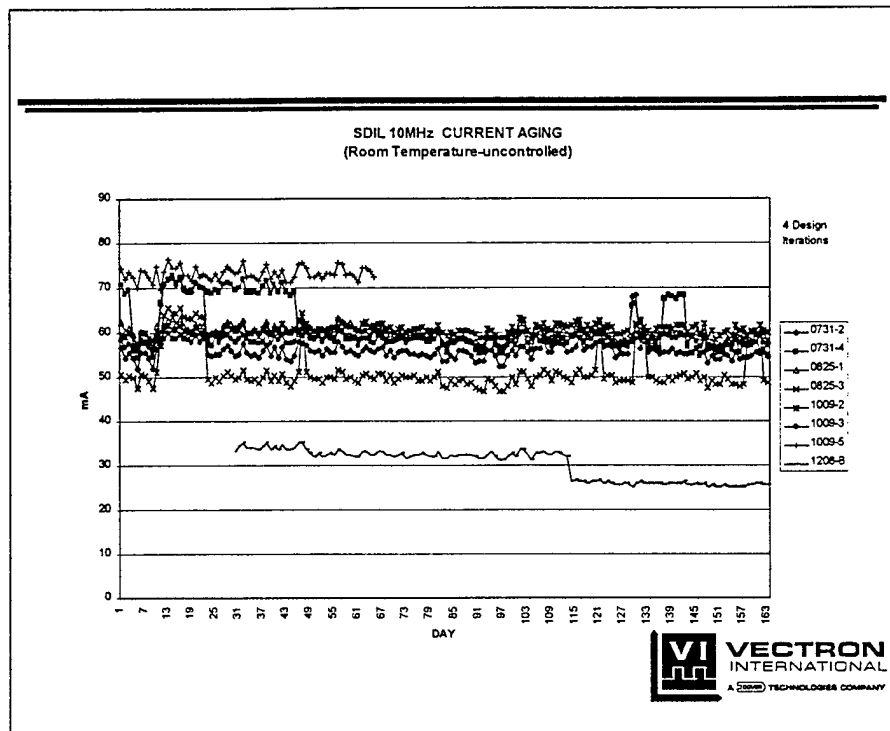
---

---

***SDIL & DDIL TEST DATA***



<b>PAGE(S)</b>	<b>TEST/DATA DESCRIPTION</b>
76	CURRENT AGING OVER TIME
77-85	TEMP STABILITY DATA/EVALUATION
86-90	CURRENT CONSUMPTION DATA/EVAL.
91-96	OEXO WARM UP DATA/EVALUATION
97-104	VIBRATION SENS. DATA/EVALUATION
105-109	PHASE NOISE DATA/EVALUATION



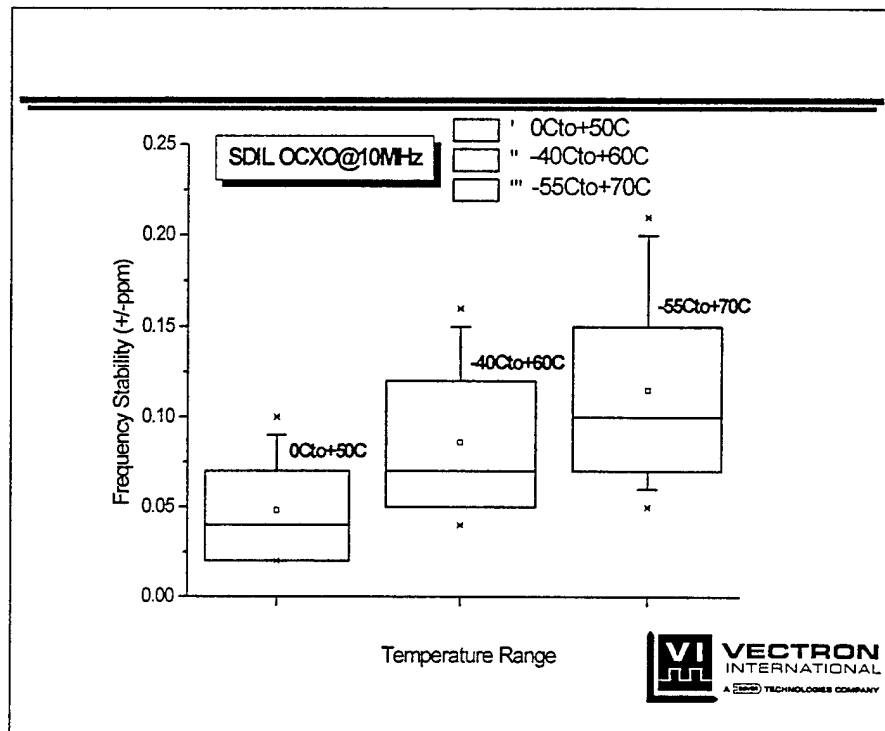
Measured heater current over an extended time period. Changes in current indicate an internal atmospheric change. The variation in average current drain is a result of different oven temperature set points. Constant power consumption over extended periods of time is indicative of low leak rates.

---

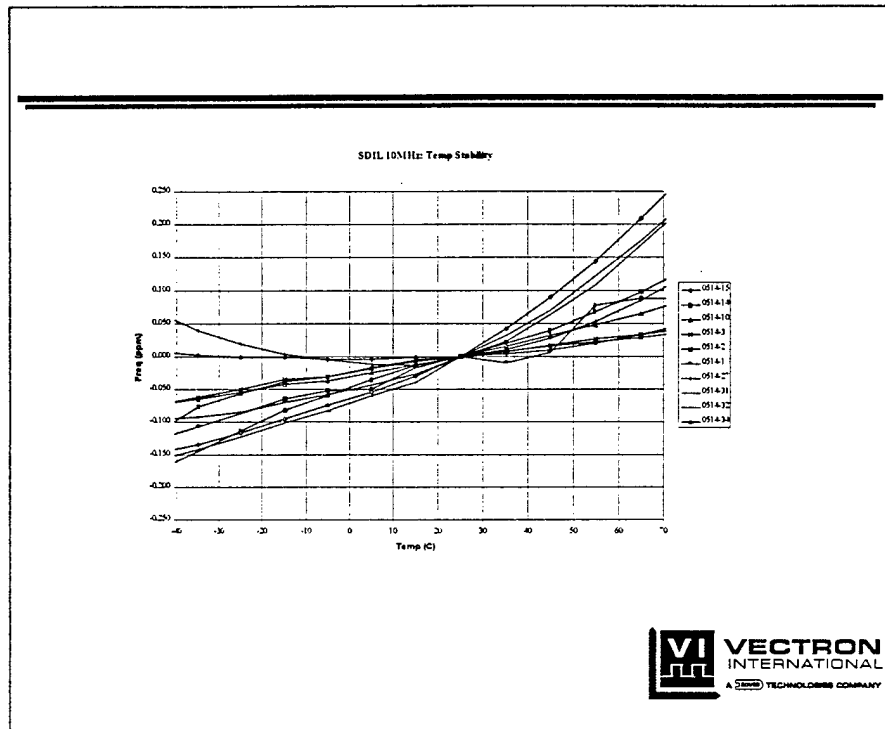
---

*Temperature Stability Data*



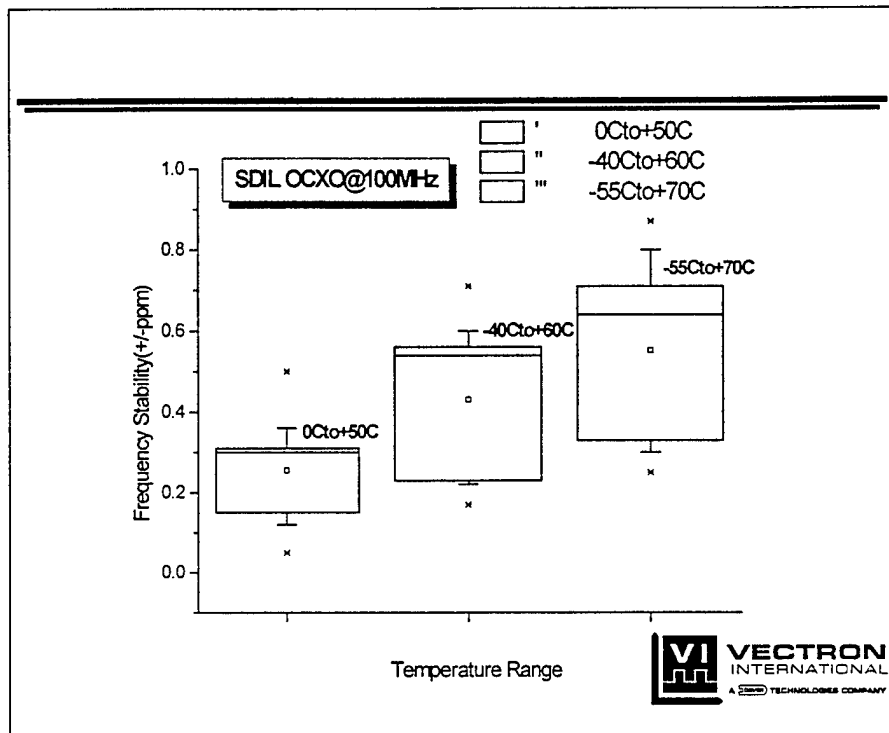


In this and the following charts, the best and worst units are shown as the lower and upper X's respectively, and the mean is the small square in the middle. The three lines on the larger box's represent 25, 50 and 75th percentile distribution of performance. Most of the variation on SDIL units is caused by the resolution of setting the substrate temperature to the crystal turnover point. Although we have identified some techniques to improve the accuracy of setting the temperature, time constraints did not allow us to implement them.

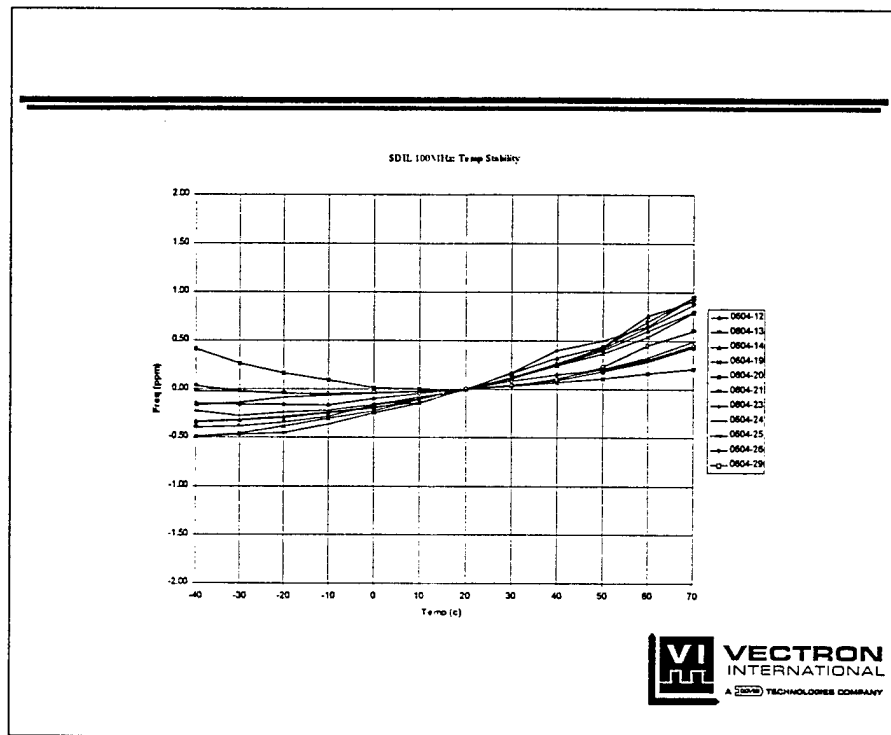


Frequency stability versus temperature of Single DIP units.

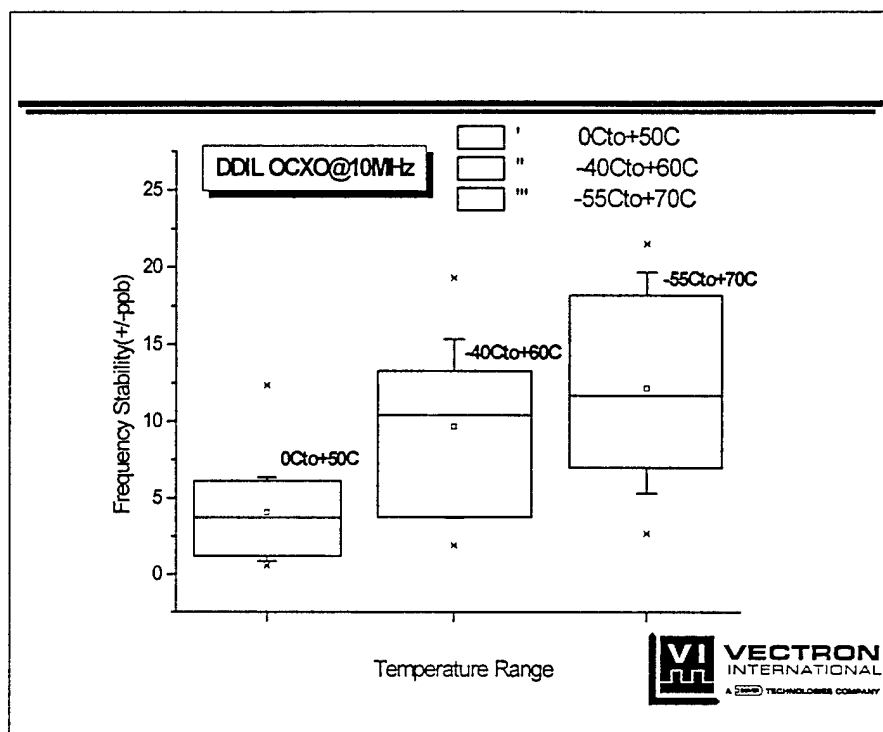
Nominal frequency of 10 MHz. Stability ranges from  $\pm 0.05$  to 0.25 ppm over the temperature range of -40 to +70 degC. The variation in performance is due mainly to the differences in turnover temperature of the crystals used. For this test, a standard oven temperature was used for all crystals, resulting in non-optimized temperature characteristics. Individual adjustment of oven temperature will result in superior performance.



As was stated previously the best and worst units are shown as the lower and upper X's respectively, and the mean is the small square in the middle. The three lines on the larger box's represent 25, 50 and 75th percentile distribution of performance. The temperature performance of the SDIL 100 MHz unit generally is not as good as that of the 10 MHz SDIL units. This is due in large part to a greater circuit sensitivity at 100 MHz to changing stray reactances and other circuit parameters

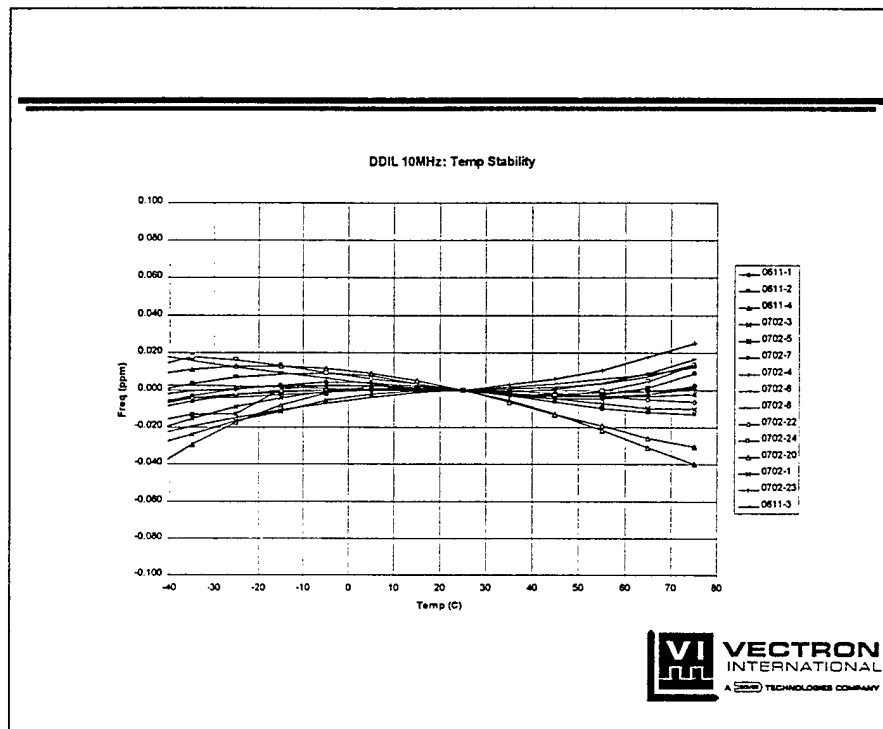


Frequency stability versus temperature of Single DIP units. Nominal frequency is 100 MHz. The crystals used in these units are 5th overtone AT cut. A single modification was made on each unit to adjust oven temperature to match the crystal parameters. While there is an apparent improvement, the slope of the frequency /temperature curve indicates that the oven temperature is still set low for most units. Further individual adjustment of temperature and servo gain would result in better temperature performance.

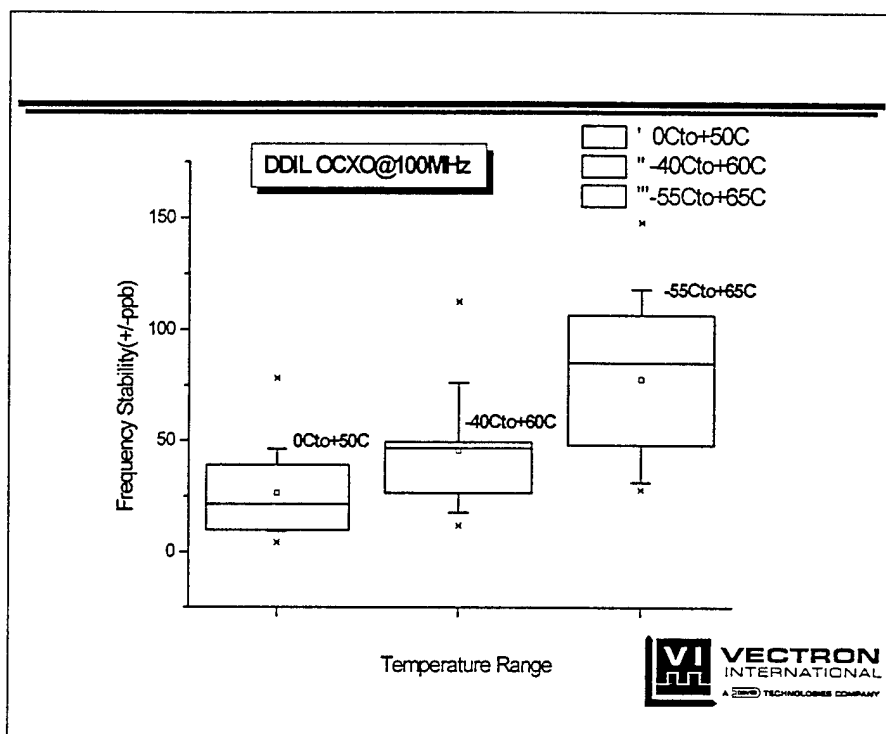


As can be seen from the data, these Double DIL units exhibit much better stability than Single DIL units. This is primarily attributed to having an ability to adjust the oven temperature with the digital potentiometer after sealing. Units are run over temperature several times at different oven temperature settings. Based on the frequency temperature data, an optimal oven temperature is selected.

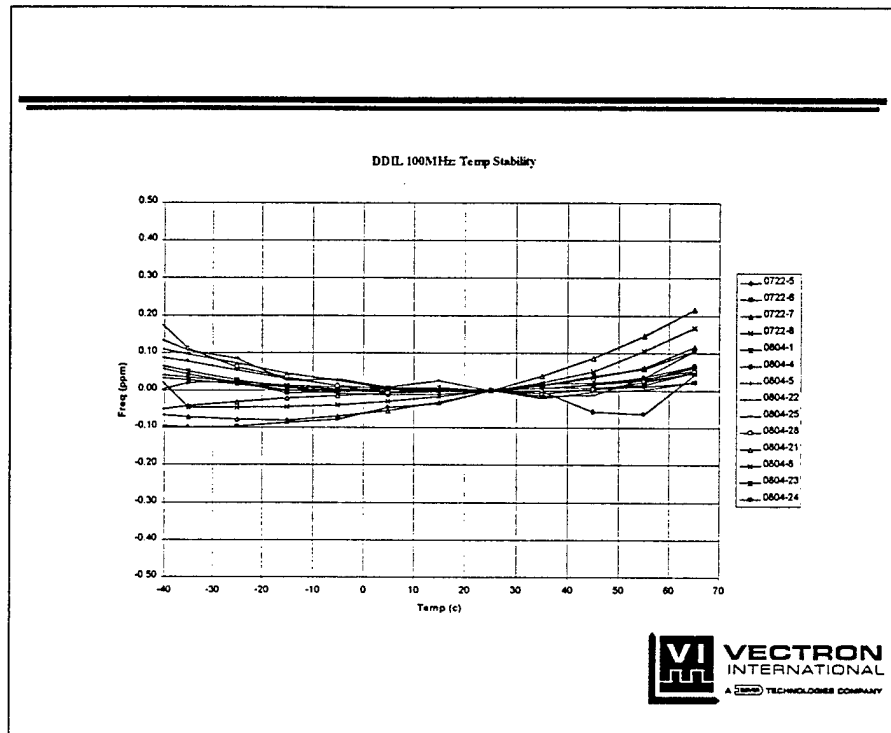




This data indicates that most of the frequency deviation is due to second and third order temperature effects. We believe that this is caused by circuit temperature variations and shifting thermal gradients. Both effects can be further improved with the use of SC crystals, but at the expense of tuning range and possibly acceleration sensitivity. We do plan on introducing SC cuts to improve thermal stability.



Data is shown to +65°C for the 100 MHz DDIL units. Crystals exhibited a lower than expected turnover point, so it was necessary to reduce the heated substrate temperature. Testing indicated that there was a shift in apparent turnover from static f-t measurements of as much as 8°C. We suspect that this is due to thermal stress effects with the AT cut. Improvements were obtained by putting a thermal shield over the crystal, but the temperature stability of the 10 MHz devices was still superior. It is felt that in most applications, the stability number achieved here are generally adequate since aging will tend to dominate at these frequencies. However, it will be necessary to improve the upper temperature limitation. We feel that this can be done through a combination of having a higher crystal turnover and improving the thermal shielding. Incorporating FC, IT or SC resonators may also improve the stability.



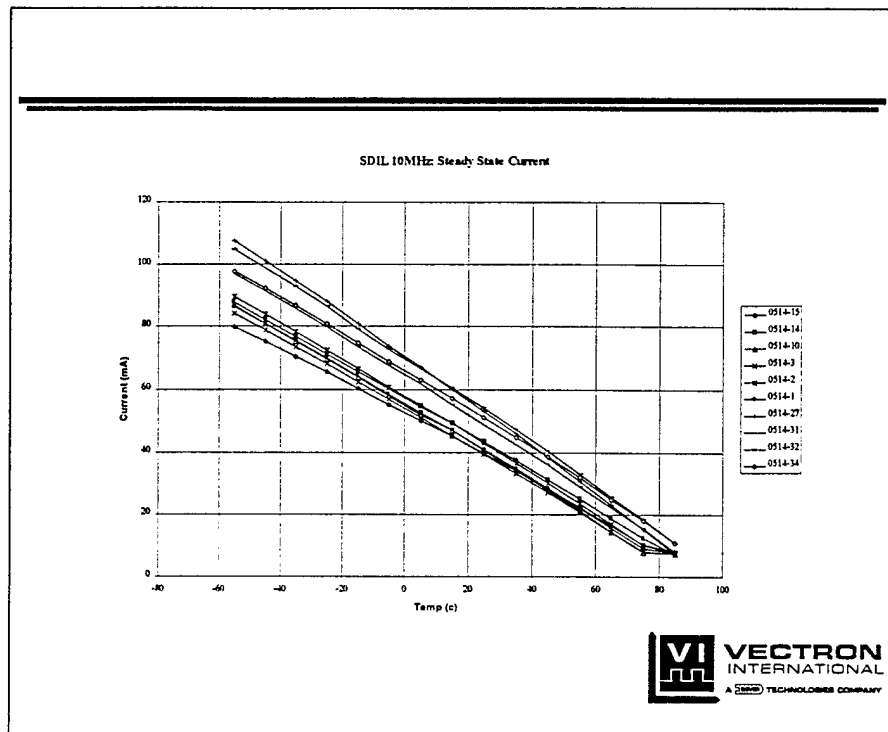
Again, it can be seen here that the linear effects are nearly absent, indicating good resolution on setting the substrate temperature. The ability to adjust each oscillator individually in the DDIL configuration yields much better temperature stability. It is also noted that temperature stability at higher frequency is degraded due to an increased sensitivity to parametric and stray circuit changes.

---

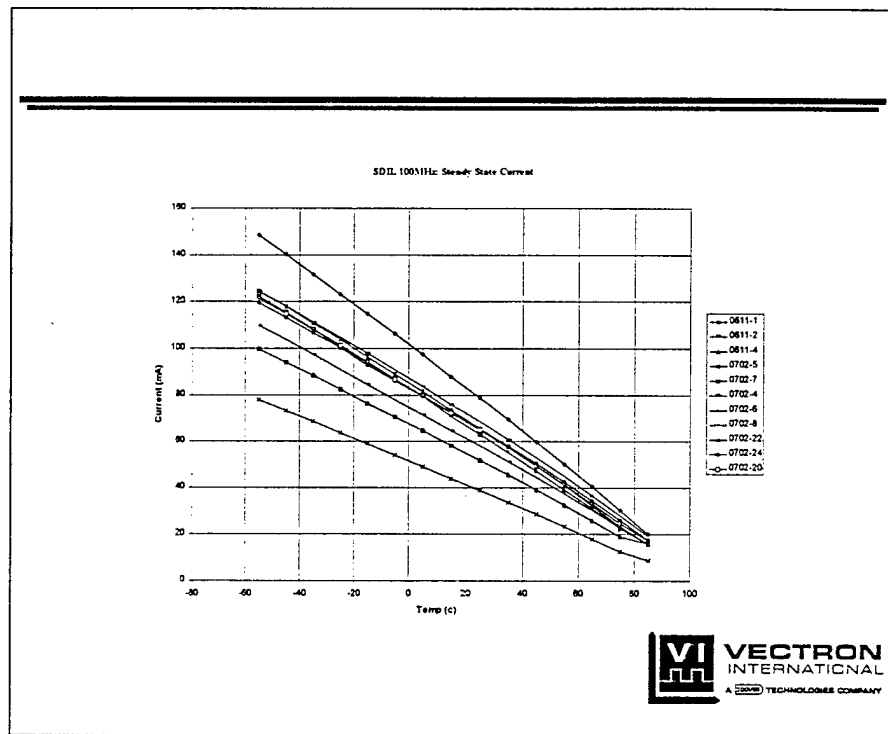
---

*Current Consumption Data*

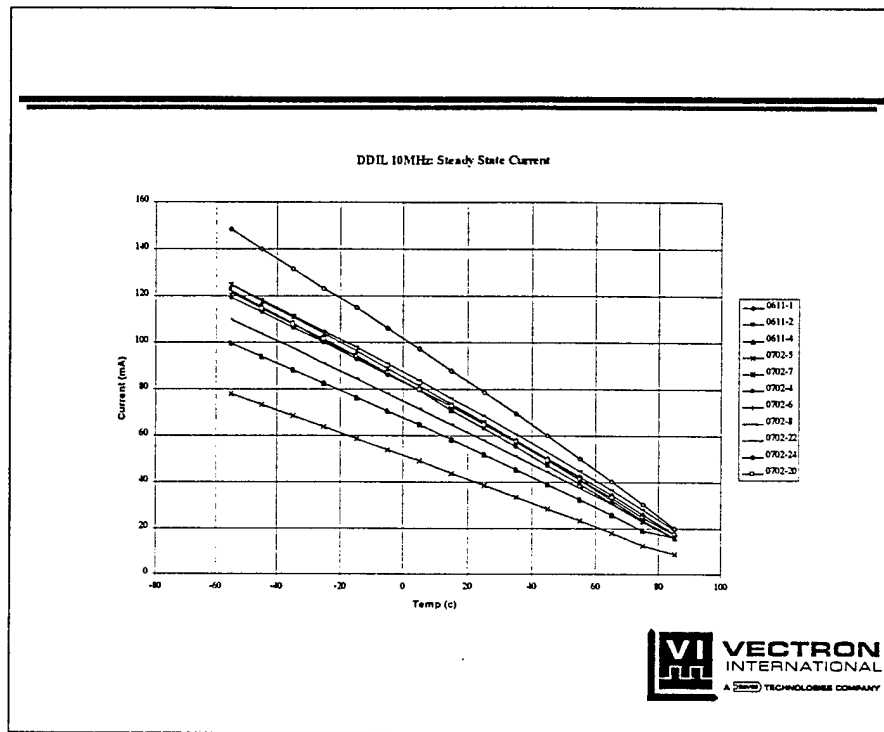




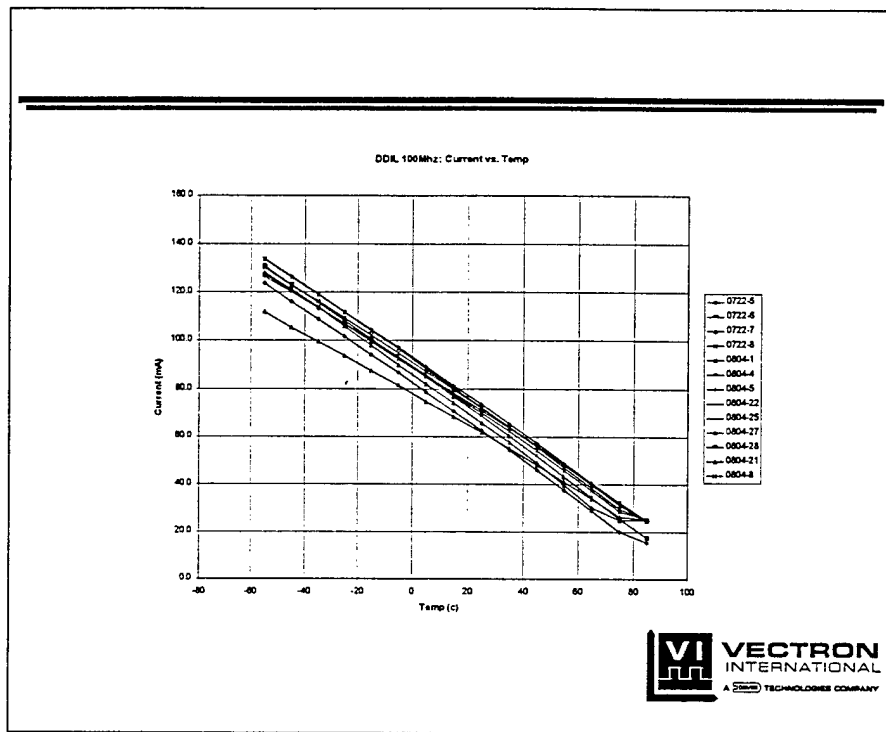
The “flattening” of current at high temperature on some units is caused by lower crystal turnover. Units with +95°C crystal turnover temperatures remained in linear operation to +85°C. We believe that the variation in thermal resistance (reflected in slope here) is caused by varying degrees of partial pressure in the can. Further work is needed to determine the root cause of the variations.



Steady state current versus ambient temperature 100 MHz. Single DIL package. Possible variations in internal atmosphere and set temperature contribute to the power variations from unit to unit. Higher average current in the SDIL package at 100 MHz compared to the SDIL 10 MHz unit is primarily due to the higher oven temperature in the 100 MHz SDIL units.



As expected, the average oven current drain for the DDIL units is greater than that of the SDIL units. As previously mentioned, the “flattening” slope at higher temperatures is due to the ambient temperature approaching the internal oscillator temperature, causing the oven to shut down.



Steady state current versus ambient temperature. 100 MHz DDIL package. The slope of current drain versus ambient temperature (thermal resistance) remains constant over almost all traces on this plot, indicating consistent low leak rates and outgasing inside the units. Again, the absolute power drain is greater for a DDIL package and a higher frequency design.

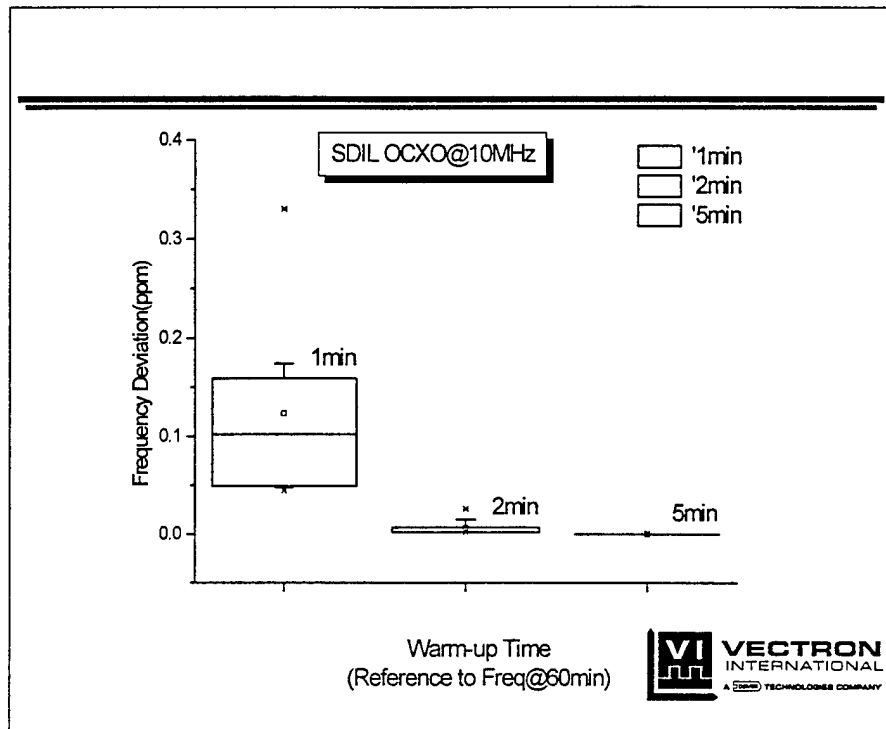


---

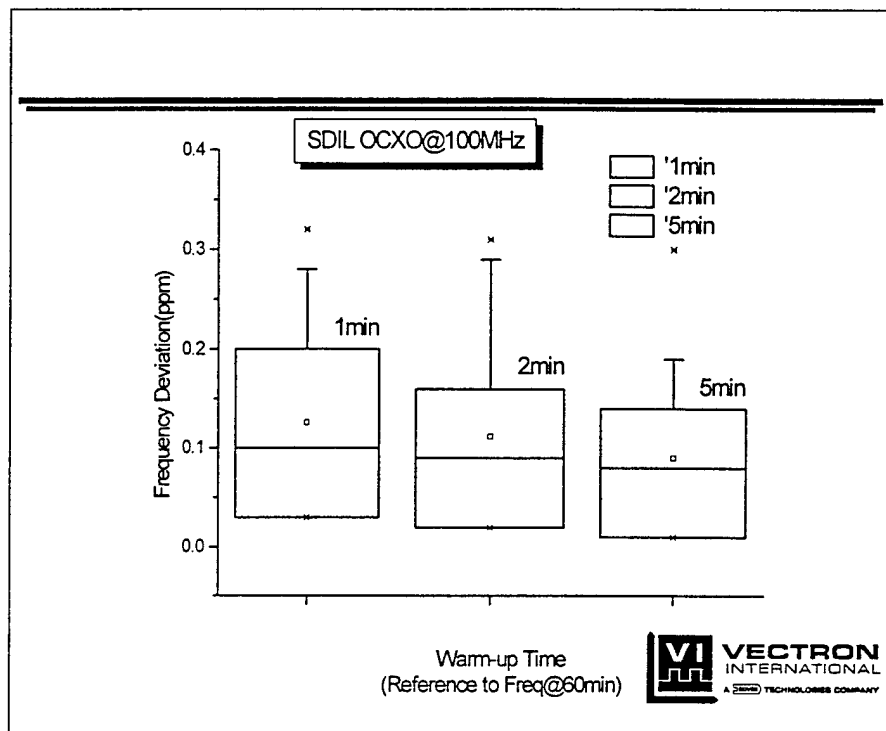
---

*OCXO Warm-up Data*



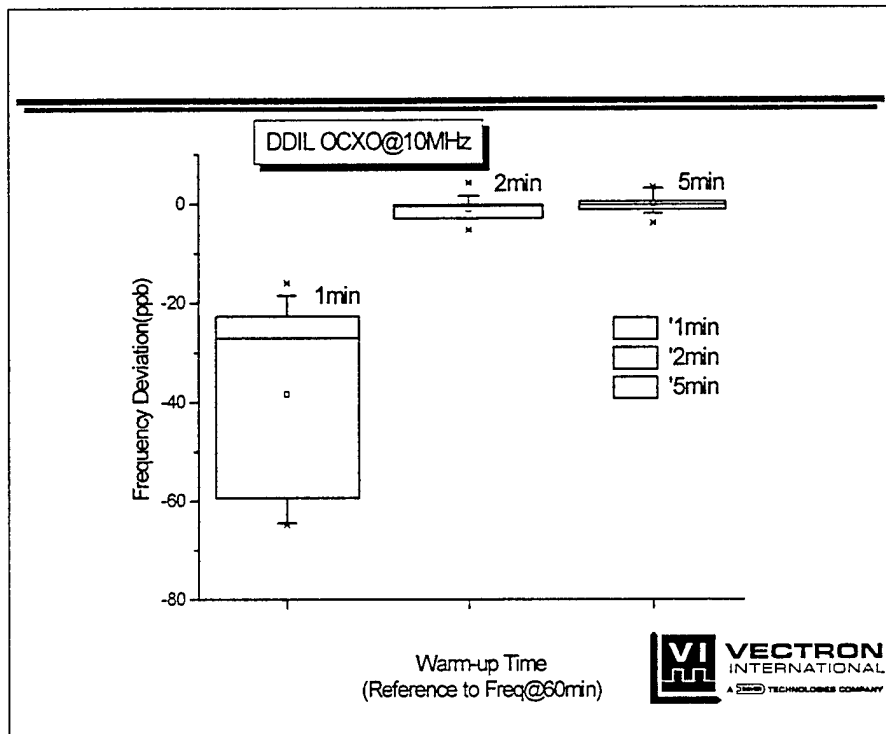


This data was taken at +25°C, and represents measurements taken on 10 pieces. Individual warm-up curves on selected units is shown on later slides at various temperatures.

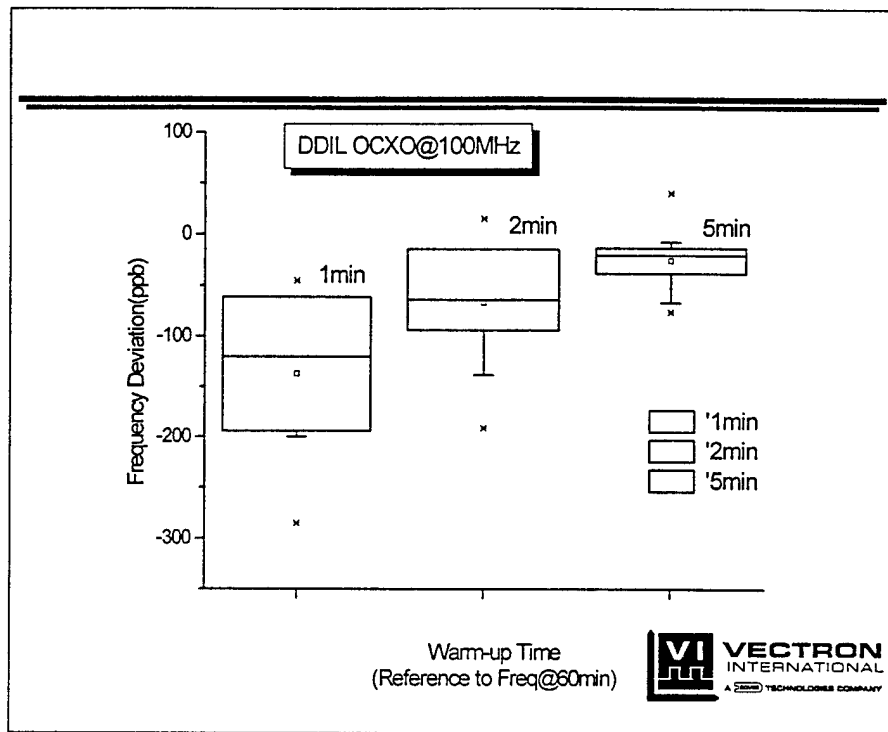


This data was also taken at +25°C, and represents measurements taken on representative pieces. Individual warm-up curves on selected units is shown on later slides at various temperatures.

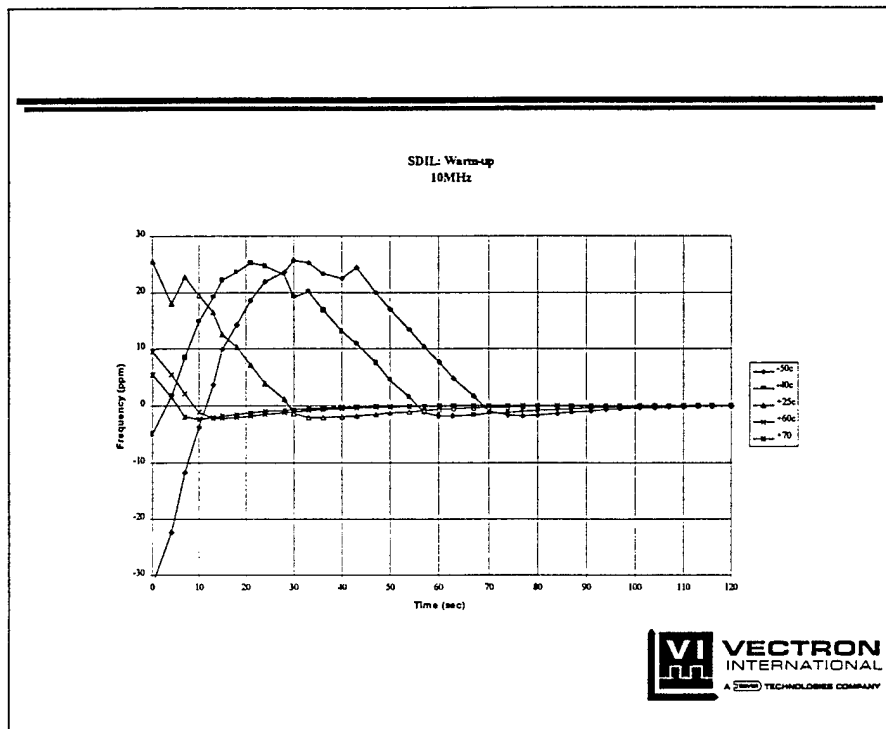
Consistent with the observations of stability, and power drain, the 100 MHz units have slightly worse performance than their 10 MHz counterparts. Again, this is primarily due to increased circuit sensitivity at higher frequencies.



This graph showing warm-up of a representative group of 10 MHz DDIL OCXO's highlights the difference in mass between the SDIL and DDIL packages. Despite the extra starting current used in the DDIL the SDIL performance is still significantly better. The DDIL package contains a more sophisticated oven controller and if faster warm-up were required, it would be possible to increase the oven startup current.



As might be expected, the frequency warm-up of the 100 MHz DDIL units is the slowest of the four types tested. In addition to reasons listed on earlier pages, the transient response of an AT cut crystal is significantly slower than the doubly rotated family of crystals, and exhibits significant overshoot when warming up.



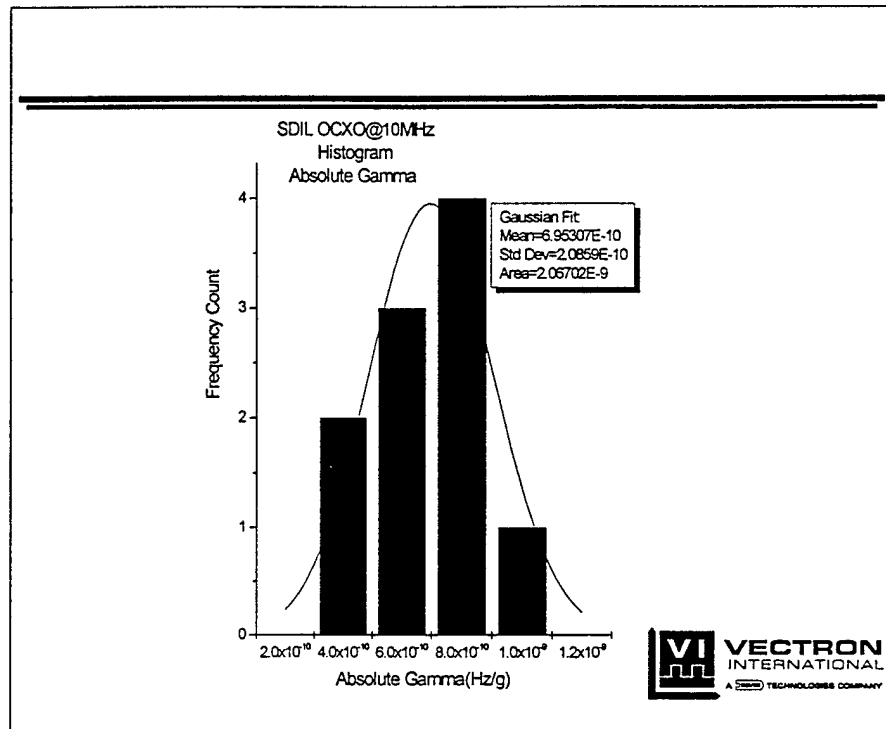
Note here that warm-up times can be reduced somewhat by increasing the initial heater current. This is set in the design by the value of one resistor, so changes can readily be accommodated.

---

---

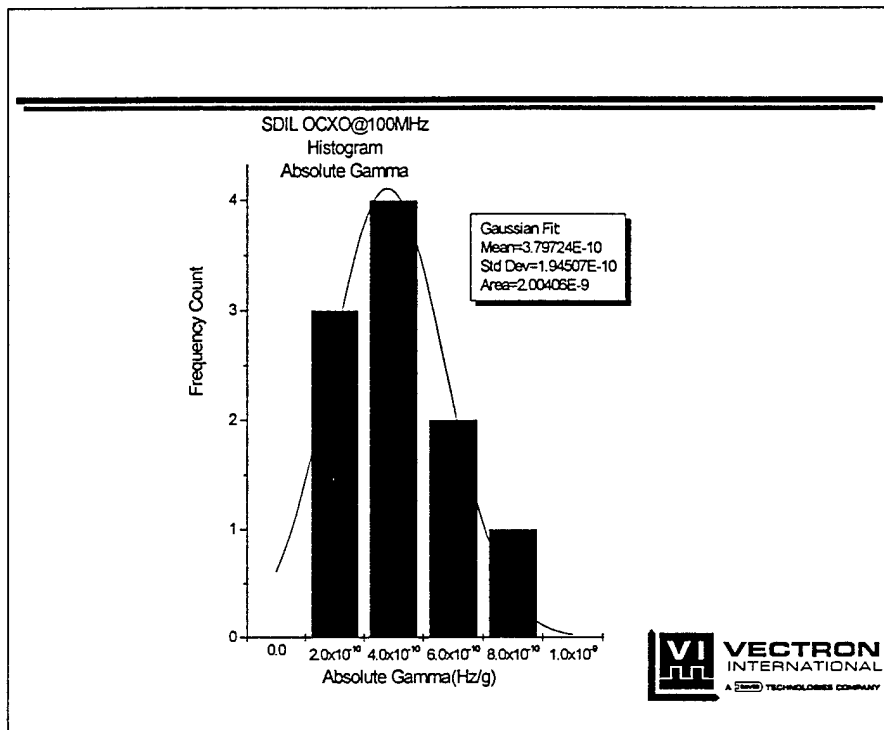
*Vibration Sensitivity Data*





Statistical fit of  $\Gamma$ (Gamma)  
Single DIL 10 MHz package



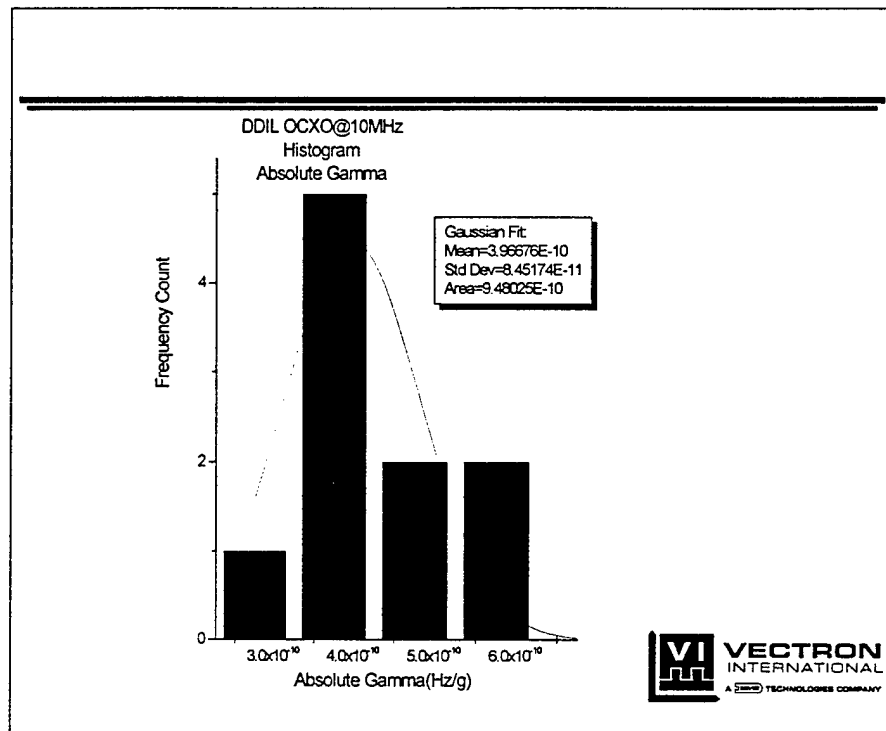


Statistical fit of  $\Gamma$ (Gamma)  
Single DIL 100 MHz package

DDIL OCXO@10MHz					
G Sensitivity	0611-2	0611-3	0702-1	0702-3	0702-4
X-Axis(/g)	5.32E-10	3.17E-10	4.94E-10	3.58E-10	3.88E-10
Y-Axis(/g)	2.36E-10	1.57E-10	1.26E-10	5.61E-11	2.46E-10
Z-Axis(/g)	1.04E-10	2.31E-10	7.26E-11	1.95E-10	3.46E-10
Gamma(/g)	5.92E-10	4.23E-10	5.15E-10	4.11E-10	5.75E-10
G Sensitivity	0702-8	0702-20	0702-22	0702-23	0702-24
X-Axis(/g)	3.48E-10	3.68E-10	3.75E-10	3.64E-10	2.48E-10
Y-Axis(/g)	1.95E-10	3.10E-10	1.15E-10	1.32E-10	6.07E-11
Z-Axis(/g)	1.06E-10	3.45E-11	4.07E-11	2.21E-11	1.94E-10
Gamma(/g)	4.12E-10	4.83E-10	3.94E-10	3.88E-10	3.21E-10



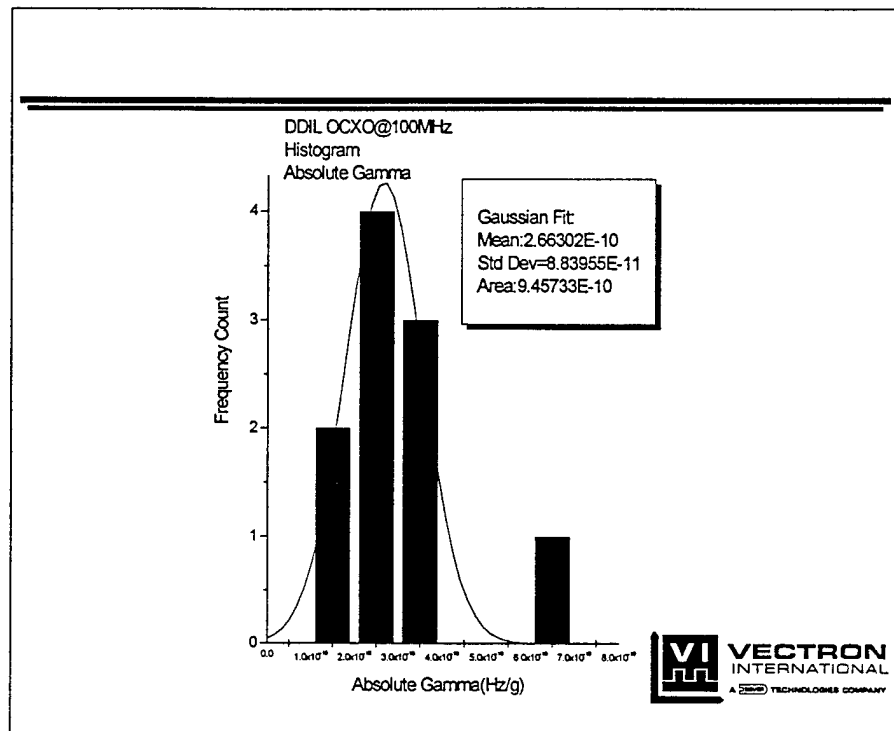
**VECTRON**  
INTERNATIONAL  
A TSCM TECHNOLOGIES COMPANY



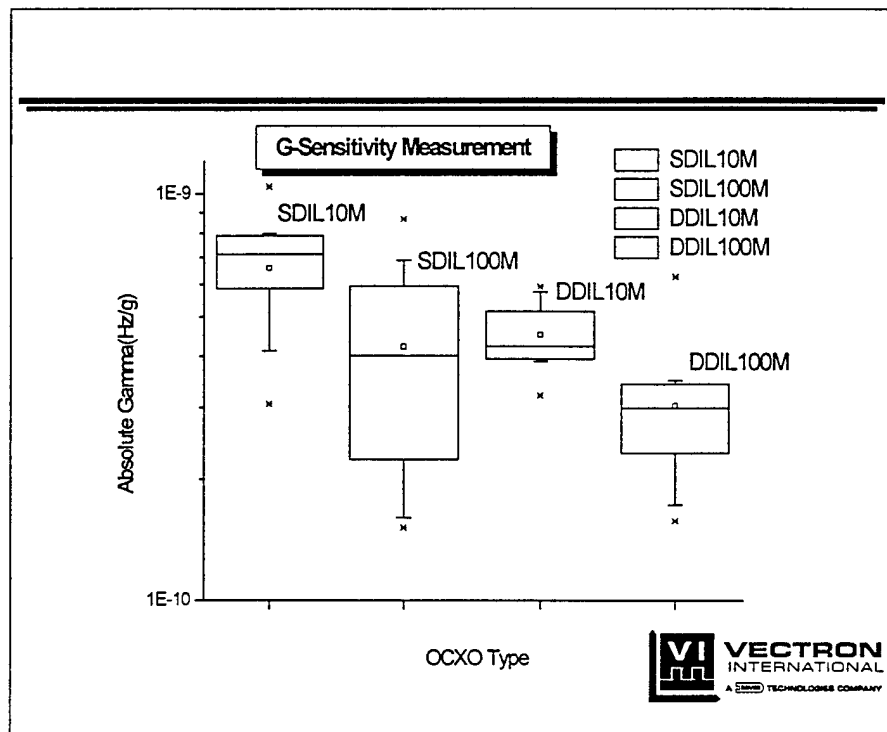
Statistical fit of  $\Gamma$ (Gamma)  
Double DIL 10 MHz package

DDIL OCXO@100MHz					
G Sensitivity	0722-7	0722-8	0804-4	0804-8	0804-21
X-Axis(/g)	1.01E-10	1.47E-10	3.19E-10	5.23E-10	1.91E-10
Y-Axis(/g)	4.98E-11	4.06E-11	8.39E-11	9.14E-11	2.29E-10
Z-Axis(/g)	1.32E-10	4.23E-11	9.05E-11	3.32E-10	2.42E-11
Gamma(/g)	1.73E-10	1.58E-10	3.42E-10	6.27E-10	2.99E-10
G Sensitivity	0804-22	0804-23	0804-24	0804-25	0804-28
X-Axis(/g)	1.55E-11	2.56E-10	2.42E-10	2.12E-10	2.23E-10
Y-Axis(/g)	1.95E-10	1.11E-11	1.11E-10	8.79E-11	2.65E-10
Z-Axis(/g)	1.31E-10	1.29E-10	1.87E-10	3.73E-11	3.46E-11
Gamma(/g)	2.35E-10	2.87E-10	3.25E-10	2.32E-10	3.49E-10





Statistical fit of  $\Gamma$ (Gamma)  
Double DIL 100 MHz package



This table and the associated data suggests that with these resonator designs, 100 MHz 5th overtone devices will exhibit superior characteristics. Since there will also be less phase noise degradation due to frequency multiplication, this also suggests that 100 MHz is a good choice when generating microwave signals with good spectral purity during vibration. If better overall stability is required (i.e temperature and aging), it would be quite straightforward to phase lock the 100 MHz oscillator to a 10 MHz reference oscillator.

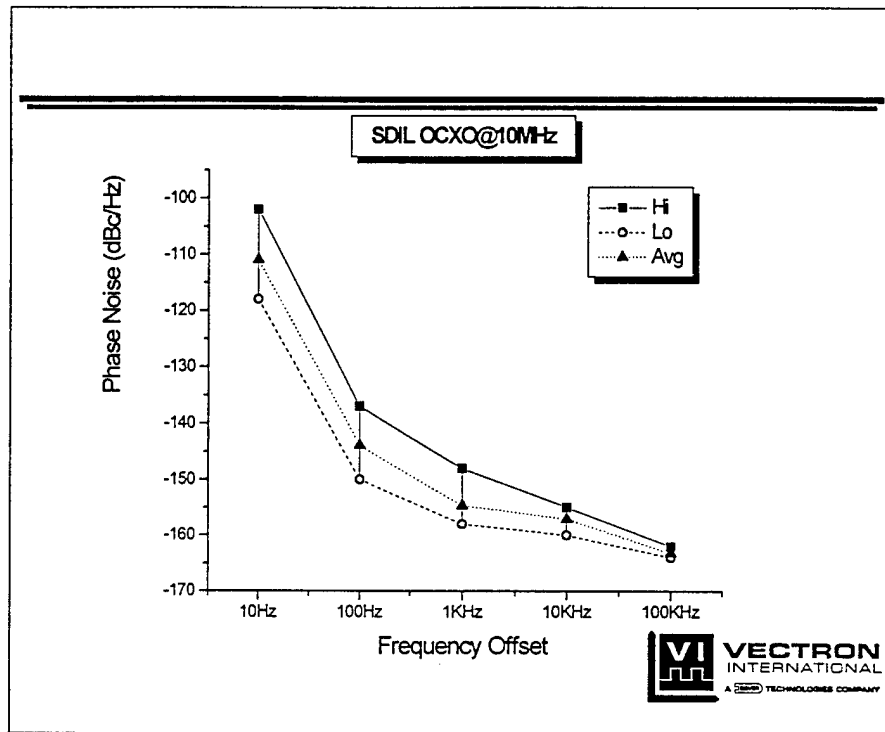
---

---

### *Phase Noise Data*

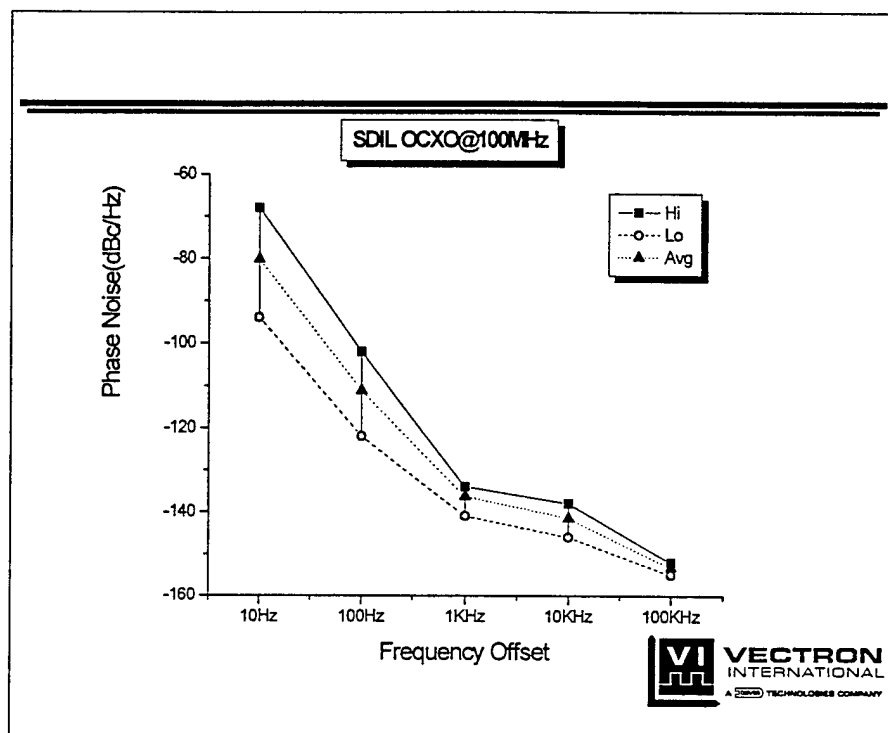


A few comments are in order regarding phase noise performance. All units were assembled in Vectron's hybrid oscillator facility in Norwalk, CT. This facility has been set up to manufacture hybrid XO's and VCXO's using standard chip and wire techniques. Blanks are procured from outside suppliers and shipped to Norwalk in plated form. While this is adequate for standard applications, it very likely degrades short-term stability and close-in phase noise for this application. Consequently, it is our belief that phase noise data (particularly variations at offsets of less than 100 Hz) may be somewhat degraded from what ultimately can be achieved. It is Vectron's intent to either find a better method of shipping plated blanks, or establish baseplating locally.

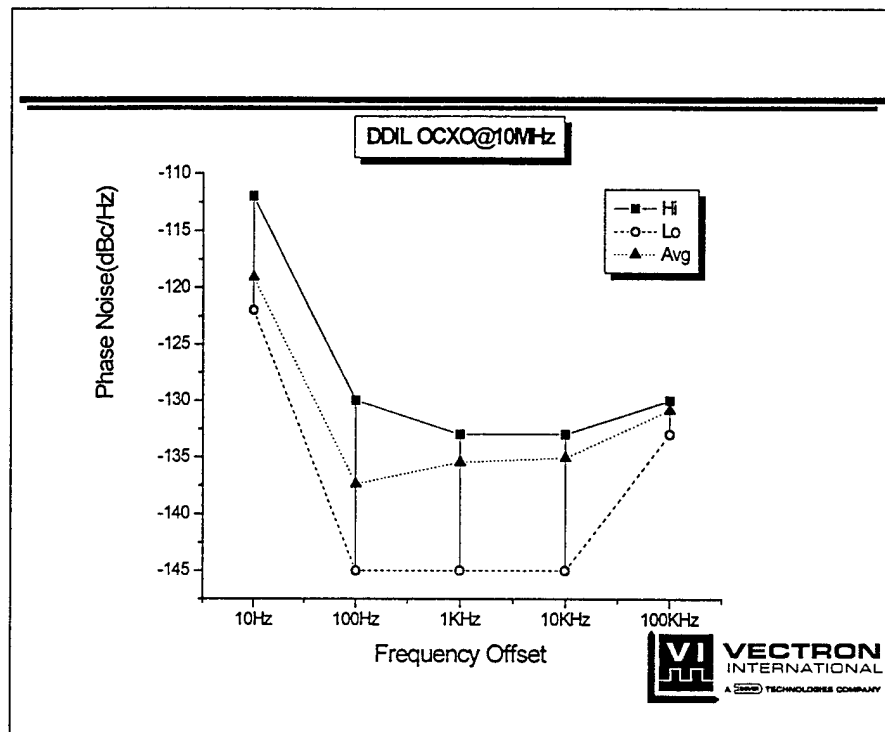


In addition to the shipping issues previously commented on, we believe that the variations in setting the substrate temperature are impacting performance somewhat. As techniques are developed to increase the accuracy of setting the temperature, we anticipate improvements at small offset frequencies.

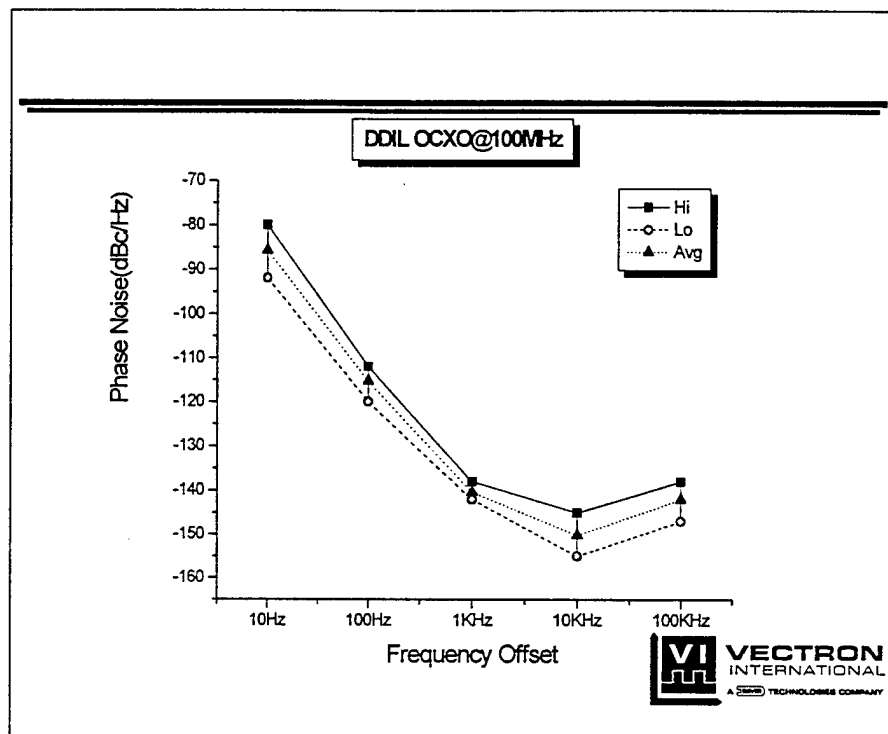




Measured Phase Noise  
100 MHz Single DIL Package



A voltage regulator has been positively identified as the source of noise at offsets of 100 Hz and larger. A new voltage regulator will be installed in future designs.

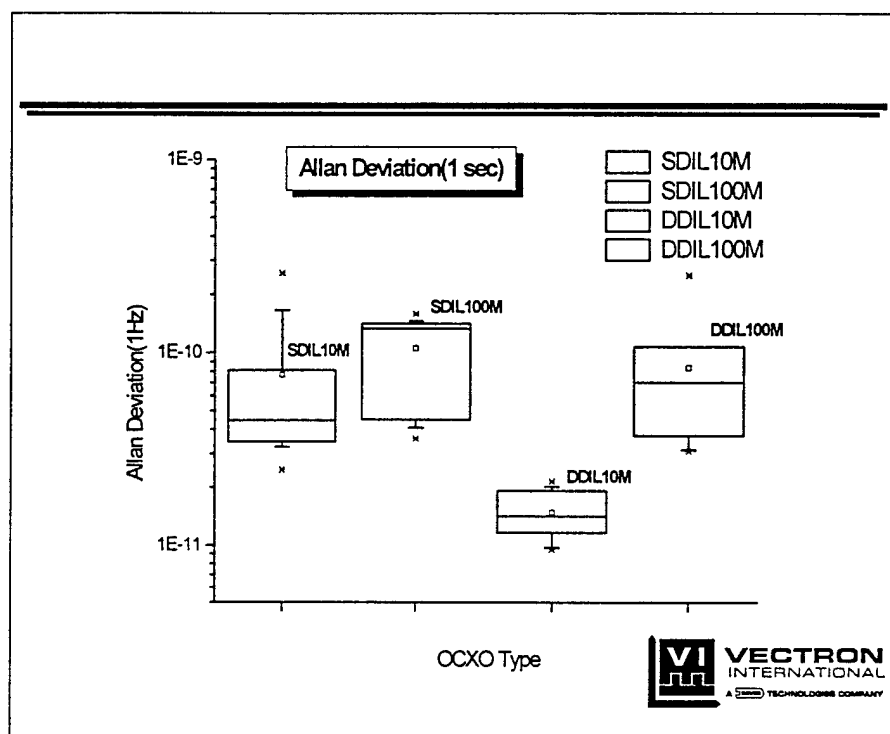


The regulator used in the 10 MHz DDIL is also used here, and will be changed to a lower noise part for future builds.

---

*Allan Deviation Data*





Again, it is our belief that better methods of processing the blanks will significantly improved Allan deviation. In addition, enhancements to the accuracy of setting substrate temperature on SDIL units may also improve performance, particularly at 10 MHz.

---

---

## *SUMMARY*



## R&D Target

Size	inch3	0.1	0.125	0.125	4	0.5
Warm-up Time	min	0.5	0.75	0.75	5	0.1
Power@25C	Watts	0.10	0.22	0.24	1.5	0.05
Allan Deviation@1s	x10-11	2	3.84	10.6	0.5	100
Vibration Sensitivity	x10-10/g	1	6.58	4.22	10	10

Parameter		CO-08 OCXO Target	DDIL OCXO @10MHz	DDIL OCXO @100MHz	OCXO Typical	TCXO Typical
Size	inch3	1.1	0.366	0.366	4	0.5
Warm-up Time	min	2	1	1	5	0.1
Power@25C	Watts	0.40	0.33	0.328	1.5	0.05
Allan Deviation@1s	x10-11 Hz	0.5	1.55	8.16	0.5	100
Vibration Sensitivity	x10-10/g	10	4.99	3.29	10	10



## Performance Summary